Revisiting linear stability of the asymptotic suction boundary layer and plane Couette flow

Zur Erlangung des akademischen Grades Doktor-Ingenieur (Dr.-Ing.)
Genehmigte Dissertation von Alparslan Yalcin aus Kitzingen
Tag der Einreichung: 25. April 2022, Tag der Prüfung: 21. Juni 2022

Erstreferent: Prof. Dr.-Ing. Martin Oberlack
Korreferent: Prof. Dr. rer. nat. Amsini Sadiki
Darmstadt, Technische Universität Darmstadt

TECHNISCHE
UNIVERSITÄT
DARMSTADT

Fachbereich Maschinenbau
Fachgebiet für
Strömungsdynamik

Revisiting linear stability of the asymptotic suction boundary layer and plane Couette flow

Genehmigte Dissertation von Alparslan Yalcin

Erstreferent: Prof. Dr.-Ing. Martin Oberlack
Korreferent: Prof. Dr. rer. nat. Amsini Sadiki

Tag der Einreichung: 25. April 2022
Tag der Prüfung: 21. Juni 2022

Darmstadt, Technische Universität Darmstadt

For Elif, my family and all my supporters

Erklärungen laut Promotionsordnung

§8 Abs. 1 lit. c PromO

Ich versichere hiermit, dass die elektronische Version meiner Dissertation mit der schriftlichen Version übereinstimmt.

§8 Abs. 1 lit. d PromO

Ich versichere hiermit, dass zu einem vorherigen Zeitpunkt noch keine Promotion versucht wurde. In diesem Fall sind nähere Angaben über Zeitpunkt, Hochschule, Dissertationsthema und Ergebnis dieses Versuchs mitzuteilen.

§9 Abs. 1 PromO

Ich versichere hiermit, dass die vorliegende Dissertation selbstständig und nur unter Verwendung der angegebenen Quellen verfasst wurde.

§9 Abs. 2 PromO

Die Arbeit hat bisher noch nicht zu Prüfungszwecken gedient.

Darmstadt, 25. April 2022

A. Yalcin

Abstract

One of the unsolved problems of fluid mechanics revolves around the prediction and description of large-scale turbulent structures, so-called turbulent superstructures, in various wall-bounded shear flows such as the asymptotic suction boundary layer (ASBL) or plane Couette flow (PCF). It is assumed that the origin of such superstructures is to be sought in the laminar-turbulent transition phenomenon.
In the present dissertation, linear stability theory (LST) is therefore revisited for aforementioned ASBL and PCF with the goal of disclosing phenomena describing and influencing the formation of large-scale structures. In the context of the ASBL, the present understanding of linear stability is extended by investigating the analytical solution of the underlying Orr–Sommerfeld equation (OSE). One of the key results in the present work is the establishment of a clear interrelation between Reynolds number and streamwise wavelength of perturbations through asymptotic analyses, which demonstrably is of universal nature and, thus, applicable to any wall-bounded shear flow. Furthermore, continuous modes are derived and examined for the ASBL, where in the spatial stability problem one solution branch gives novel unstable continuous modes.
A curiosity of PCF is that LST predicts linear stability exclusively, whereas experiments and numerical simulations provide evidence of laminar-turbulent transition leading to fully turbulent PCF. It is shown in this work that, in contrast to suction boundary layers, transpiration destabilizes PCF and above a minimal transpiration rate yields PCF linearly unstable. It is additionally demonstrated that in the infinite limit of the transpiration rate, PCF can be converted to the ASBL via specific parameter and coordinate transformations.
The final part of this thesis revolves around the discovery of novel unstable three-dimensional (3D) spatial modes. An extension of Squire's transformation to the spatial stability framework discloses the mathematical necessity of additionally introducing complex spanwise wave numbers and, thus, possible growth in the spanwise direction, which in previous research was neglected in view of Squire's theorem. Thereof, it is demonstrated that these novel modes with oblique growth may lead to subcritical transition in potentially linearly unstable two-dimensional (2D) flows. Linearly stable 2D flows in turn experience growth of the perturbation velocity field in spanwise direction, which is reminiscent of large-scale laminar-turbulent patterns known from numerical simulations of transitioning PCF. Therefore, 3D PCF superposed by such oblique modes is studied in conclusion through a direct numerical simulation (DNS) with a spectral element solver.

Zusammenfassung

Ein ungelöstes Problem der Strömungsmechanik dreht sich um die Vorhersage und Beschreibung von großskaligen turbulenten Strukturen, sogenannten turbulenten Superstrukturen, in verschiedenen wandgebundenen Scherströmungen wie der asymptotisch abgesaugten Grenzschichtströmung (engl. asymptotic suction boundary layer (ASBL)) oder der ebenen Couette-Strömung (engl. plane Couette flow (PCF)). Vermutet wird, dass der Ursprung solcher Superstrukturen im laminar-turbulenten Umschlagsphänomen zu suchen ist.
In der vorliegenden Dissertation wird infolgedessen die lineare Stabilitätstheorie (engl. linear stability theory (LST)) für die ASBL und PCF neu aufgegriffen mit dem Ziel, Phänomene ausfindig zu machen, welche die Entstehung großskaliger Strukturen bedingen und beeinflussen. Im Kontext der ASBL wird hierfür das gegenwärtige Verständnis der linearen Stabilität erweitert, indem die analytische Lösung der Orr-Sommerfeld Gleichung (engl. Orr–Sommerfeld equation (OSE)) eingehend untersucht wird. Ein zentrales Ergebnis der vorliegenden Arbeit ist die Herstellung eines klaren Zusammenhangs zwischen Reynolds-Zahl und Störwellenlänge in Strömungsrichtung durch asymptotischen Analysen, welcher überdies nachweislich universeller Natur ist und daher auf beliebige wandgebundene Scherströmungen übertragen werden kann. Ferner werden kontinuierliche Moden für die ASBL hergeleitet und untersucht. Ein wesentliches Ergebnis besteht in der Existenz eines Lösungszweiges im räumlichen Stabilitätsproblem, durch welches neuartige instabile kontinuierliche Moden auftreten.
Eine Besonderheit der PCF besteht darin, dass die LST ausschließlich lineare Stabilität vorhersagt, wohingegen Experimente und numerische Simulationen nachweisen, dass laminar-turbulenter Umschlag möglich ist. In der vorliegenden Arbeit wird gezeigt, dass, im Gegensatz zur ASBL, Transpiration einen destabilisierenden Effekt auf die PCF hat und schließlich zu linearer Instabilität für ausreichend große Transpirationsraten führt. Außerdem wird gezeigt, dass für unendlich große Transpirationsraten die ebene Couette-Strömung durch geeignete Koordinaten- und Parametertransformationen in die ASBL überführt werden kann.
Im finalen Teil dieser Thesis wird die Entdeckung neuartiger 3D Moden mit schrägem Wachstum thematisiert. Eine Erweiterung der Squire-Transformation für das räumliche Stabilitätsproblem legt die mathematische Notwendigkeit offen, zusätzlich komplexe Spannweitenwellenzahlen einzuführen und damit das Wachstum von Störungen in Spannweitenrichtung zu ermöglichen, was in einschlägiger Literatur in Anbetracht des Squire-Theorems vernachlässigt wurde. Ein zentrales Ergebnis besteht darin, dass diese neuartigen Moden mit schrägen Wachstumsmechanismen zu subkritischem Umschlag von potentiell linear instabilen 2D-Strömungen führen können. Für linear stabile 2D-Strömungen hingegen ergibt sich, dass das entstehende Störgeschwindigkeitsfeld in Spannweitenrichtung anwächst, was Ähnlichkeiten zu großskaligen laminar-turbulenten schrägen Strukturen in umschlagender PCF aufweist, die aus einschlägigen numerischen Simulationen bekannt sind. Aus diesem Grund wird die 3D PCF überlagert mit derartigen schrägen Moden abschließend in einer direkten numerischen Simulation (engl. direct numerical simulation (DNS)), durchgeführt mit einem Spektralelementlöser, untersucht.

Acknowledgements

First, I would like to cordially thank Prof. Dr.-Ing. habil. Martin Oberlack for his excellent supervision during the 4 years in which the research presented in this dissertation has been conducted. His scientific and personal guidance have invaluably promoted the results presented in this thesis. Furthermore, I would like to thank him and the Chair of Fluid Dynamics for the possibility of using the institute's infrastructure, attending conferences and meetings, and finally for the excellent scientific atmosphere in the institute which fruitfully contributed to my personal research. For this, I also express my thanks to the remaining permanent members of the institute Prof. Dr.-Ing. habil. Yongqi Wang, Dr.-Ing. Florian Kummer and Ruth Völker.
Additional gratitude is expressed towards Prof. Dr. rer. nat. habil. Amsini Sadiki, who agreed to be my second supervisor.
I would furthermore like to thank Prof. Dr. Sergio Hoyas for his scientific consultation during the numerical studies conducted in my research as well as for the two weeks I was able to spend at the Universitat Politecnica de Valencia, Spain.
I cannot be thankful enough to Tim Gebler, who has not only been a fantastic office mate throughout my entire PhD research, but also has become an invaluable friend to me. I also want to express my thanks to Jie Liu, who has also become an important friend as the third person in office no. 324. I further want to thank all the other great friends I have made at our institute, both graduated and still continuing their research. It has also been an honor and great experience to supervise four master theses and as many seminar works. Thank you to my supervisees for their effort and fruitful discussions. I thoroughly enjoyed all supervisions and personally grew by taking responsibility.
Special thanks are expressed towards the proof readers of this dissertation. It is great to have people in my group of friends who dedicate their valuable time to support me with their scientific expertise and sharp eyes.
Last, but certainly not least, I would love to thank my parents, my sisters and my beloved Elif for always providing support and countless consultations to me. Every endeavor is accompanied with hardship and moments of doubt. In these moments it is indispensable to have people around you who believe in and endure you. I hope I will be able to repay everything you have done for me. I would like to close my acknowledgements with words by my father:
Always do the right thing and eventually everything will fall into place.

I want to express my gratitude towards the German Research Foundation (DFG), who financially supported the present research via the grant OB96/45-1 and established the priority programme SPP1881 in which my research was embedded. Calculations for this research were conducted on the Lichtenberg high performance computer of the TU Darmstadt.

Author's contribution

All results presented in chapter 3 - 6 were elaborated under the supervision of Prof. Dr.-Ing. habil. Martin Oberlack.

Contributions to chapter 3: The results of the temporal stability analysis in chapter 3 are reproduced from Yalcin et al. (2021), with the permission of AIP Publishing. Jalal Mirzayev conducted the derivation of the symmetry-induced ansatz functions in his unpublished bachelor thesis under the supervision of Prof. Dr.-Ing. Martin Oberlack, which were subsequently thoroughly analyzed by me in section 3.2.4. Jonas Tautz contributed to the parameter analysis of the spatial continuous modes discussed in section 3.3.2 under my supervision during his unpublished master thesis and a subsequent endeavor as research assistant.

Contributions to chapter 4: The results in chapter 4 were worked out both by me and by Weihang Sun in an unpublished master thesis supervised by Prof. Dr.-Ing. Martin Oberlack and me. Weihang Sun conducted the stability analysis under my guidance by employing scripts and methods worked out and provided by me, whereas I derived the transformation to the asymptotic suction boundary layer in the infinite transpiration rate limit.

Contributions to chapter 5 & chapter 6 The results in chapter 5 are elaborated as follows: Prof. Dr.-Ing. Martin Oberlack introduced the idea of applying Lie symmetry theory on the set of parameters in the Orr-Sommerfeld equation, which resulted in an extension of Squire's transformation to the spatial framework. The emerging invariance conditions were partially solved for the spanwise wave number by Yasin Turkac in an unpublished master thesis as well as in a subsequent endeavor as a research assistant under Prof. Dr.-Ing. Martin Oberlack's and my supervision. These results were subsequently corrected and completed by me. I further applied the newly established theory exemplary on plane Couette flow and numerically verified the results in a direct numerical simulation with the open source spectral element code *nek5000* (Fischer et al., 2008) in chapter 6.

Contents

List of Figures xvii

List of Tables xxi

List of Abbreviations xxiii

1 Introduction 1
- 1.1 Large-scale structures in laminar and turbulent flows . . . 1
- 1.2 Revisiting linear stability analysis for wall-bounded canonical shear flows exemplified by plane Couette flow and the asymptotic suction boundary layer . . . 3
- 1.3 Outline . . . 4

2 Basic equations of linear stability theory 5
- 2.1 Continuum mechanics . . . 5
- 2.2 Conservation laws . . . 7
  - 2.2.1 Continuity equation . . . 7
  - 2.2.2 Momentum equation . . . 8
- 2.3 Navier-Stokes equations . . . 9
  - 2.3.1 Non-dimensional Navier-Stokes equations . . . 11
- 2.4 Equations of linear stability theory . . . 12
  - 2.4.1 Linearized Navier-Stokes equations . . . 12
  - 2.4.2 Orr-Sommerfeld and Squire equations . . . 13
  - 2.4.3 Temporal and spatial stability . . . 16
  - 2.4.4 Squire's transformation . . . 19

3 Revisiting linear stability of the asymptotic suction boundary 21
- 3.1 Linear stability equations for the asymptotic suction boundary layer . . . 23
- 3.2 Temporal stability analysis of the asymptotic suction boundary layer . . . 29
  - 3.2.1 Continuous temporal linear modes . . . 29
  - 3.2.2 Asymptotic analysis of the parameters in the temporal eigenvalue problem 31
  - 3.2.3 Temporal stability characteristics of the asymptotic suction boundary layer 36
  - 3.2.4 Symmetry-induced ansatz modes . . . 46
- 3.3 Spatial stability analysis of the asymptotic suction boundary layer . . . 50
  - 3.3.1 Computation of the spatial Tollmien-Schlichting modes of the asymptotic suction boundary . . . 51
  - 3.3.2 Continuous spatial linear modes . . . 52
- 3.4 Conclusive remarks . . . 58

4 Destabilization of plane Couette flow via wall-normal constant transpiration 61
4.1 Governing stability equations for plane Couette flow with transpiration 62
4.2 Transformation to the asymptotic suction boundary layer in the large Re_V limit 64
4.3 Stability characteristics of plane Couette flow with transpiration 67
4.3.1 Neutral stability surfaces, curves and critical parameters 67
4.4 Spectra and eigenfunctions 71
4.5 Summary and conclusions 73

5 Extension of Squire's transformation to spatial stability and novel unstable oblique modes 75
5.1 Revisiting Squire's transformation as an equivalence transformation 77
5.2 Extended Squire's transformation for spatially developing instabilities and oblique modes 79

6 Direct numerical simulations of oblique modes in plane Couette flow 83
6.1 Spatial stability problem of plane Couette flow and generation of 3D modes with oblique growth 83
6.2 Numerical method and boundary conditions 86
6.3 DNS Results 88
6.4 Summary 92

7 Conclusion 93

Bibliography 97

A Appendix 103
A.1 Asymptotic expansion for small streamwise wave numbers 103
A.2 Asymptotic expansion for distinguished limit Re_α 104
A.3 Asymptotic expansion for large streamwise wave numbers ($\alpha \to \infty$) 106
A.4 Asymptotic expansion for the Stokes-limit ($Re \to 0$) 107

B Solution to Orr-Sommerfeld equation for plane Couette flow 109

List of Figures

2.1 Molecules of diameter d in a domain with the characteristic length L, the pressure p and temperature T oscillate and have the instantaneous velocity $\boldsymbol{v}$. The likelihood of collisions is quantified by the mean free path $\lambda(p, T, d)$. . . . 6

2.2 Visualization of a typical set of solution curves in a temporal stability problem for a given Reynolds number. Only the Tollmien–Schlichting (TS) mode curve yields unstable modes in the vicinity of α_{cr}, which therefore is the curve of interest. The higher mode curves are not visualized. 18

3.1 Schematic depiction of the three-dimensional (3D) asymptotic suction boundary layer (adapted from Yalcin et al. (2021)) 23

3.2 Temporal continuous spectrum for the ASBL (line) and the Blasius boundary layer (BBL) (dashed line) with $\alpha = 1$ and $Re = 500$. For both spectra a maximum is located at $\omega_r = 1$ and $\omega_i = -\alpha^2/Re$. (adapted from Yalcin et al. (2021)) . . 31

3.3 (a) The Laurent-series coefficient ω_1 in (3.59) is plotted vs. $Re_\alpha = Re\,\alpha$ as defined in (3.57). The lower threshold below which $\omega_1(Re_\alpha)$ yields no solutions is $Re_{\alpha,min} \approx 0.84191$. (b) Employing ω_1 into (3.59) and Re_α with a fixed Re into (3.57) gives the actual physical parameters ω and α, which is concretely plotted for $Re = 1.0 \times 10^5$. (adapted from Yalcin et al. (2021)) 34

3.4 (a) Computations of solutions ω in the original eigenvalue problem (EVP) (3.54) for $Re = 1.0 \times 10^5$ in surrounding of the lower threshold $\alpha_{min} = 0.84191 \times 10^{-5}$, which is seemingly identical to the results obtained for the expanded EVP in figure 3.3b. (b) Visualization of the semi-logarithmic error of the eigenvalues computed from the expanded EVP (3.61) relative to the eigenvalues obtained from the full EVP (3.54). (adapted from Yalcin et al. (2021)) 35

3.5 Depiction of the two-dimensional (2D) temporal stability map presenting the temporal growth rate of the least stable TS modes as discussed in figure 2.2. The colored shades represent unstable modes whereas blank areas are areas of stability. The Reynolds number axis is given logarithmically. The point-dashed line gives the asymptote derived by Dempsey and Walton (2017) via the triple-deck theory for large Re. (adapted from Yalcin et al. (2021)) 37

3.6 Temporal spectra are displayed at fixed $Re_{cr} = 54378.62032$ and varying α: (a) $\alpha = 0.001$; (b) $\alpha = 0.01$; (c) $\alpha_{cr} = 0.15546$; (d) $\alpha = 1$. Here and in figure 6 the red parabola denote the temporal continuous spectra given by (3.52). (adapted from Yalcin et al. (2021)) 40

3.7 Temporal spectra are displayed at fixed $\alpha_{cr} = 0.15546$ and varying Re: (a) $Re = 500$; (b) $Re = 5000$; (c) $Re_{cr} = 54378.62032$; (d) $Re = 500000$. The spectra were obtained analogous to figure 3.6. Eigenfunctions of the eigenvalues $1 - 4$ in figure (c) are shown in figure 3.8. (adapted from Yalcin et al. (2021)) 41

3.8 Eigenfunctions of the wall-normal disturbance $v_r(y)$ vs. y are plotted for the critical parameters Re_{cr} and α_{cr} given in (3.64c). The corresponding ω are given in figure 3.7c where eigenfunctions for selected ω are shown: (a) $\omega_1 = 0.023296$, (b) $\omega_2 = 0.050041 - 0.021402i$, (c) $\omega_3 = 0.073523 - 0.036063i$, (d) $\omega_4 = 0.14120 - 0.043418i$. (adapted from Yalcin et al. (2021)) 42

3.9 TS eigenfunctions $\tilde{v}_r(y)$ parametrized by Re at fixed $\alpha = \alpha_{cr}$ (a) and α at fixed $Re = Re_{cr}$ (b). The critical parameters can be taken from (3.64c). For comparison we have displayed the laminar base solution in the form $1 - U(y)$. (adapted from Yalcin et al. (2021)) 43

3.10 (a) wave decay-rate length (WDRL) δ_σ as given in (3.71) as a function of α and Re. (b) Wave propagation angle Θ as given in (3.70) as a function of α and Re (in degrees) (adapted from Yalcin et al. (2021)) 45

3.11 Viscous part of the harmonic wall-normal perturbation velocity (3.66) rescaled to unity at $Re = 1.0 \times 10^4$ and $\alpha = 1.0 \times 10^{-4}$, accounting for $Re_\alpha = 1.0$. The black-dashed line represents the WDRL (3.71), which for the present wave gives $\delta_\sigma = 1.82360$. The propagation angle yields $\theta = 89.99064°$. 46

3.12 2D spatial stability map with spatial amplification rate α_i plotted semilogarithmically with $4.0 \times 10^4 \leq Re \leq 5.0 \times 10^5$. Blank areas describe linearly stable modes. The critical triplet is given in (3.64c). 51

3.13 The complex limit ω_{cl}, below which α_i yields complex values and thus no continuous modes exist, is plotted for $\alpha_{cr} = 1$ and various orders of Re. The asymptotics for large Re as given in (3.111) is visualized in dashed lines. . . . 53

3.14 The 2D amplification map ($\beta = 0$) for (a) the positive solution $\alpha_{i,+}$ and (b) the negative solution $\alpha_{i,-}$ is plotted vs ω and Re with $\alpha_r = 0.1$. The lines indicate isolevels of amplification. All positive solutions are amplified while the negative solutions are damped. A minimum in α_i is clearly visible at $\omega = \alpha_r = 0.1$. . . . 54

3.15 The spatial growth rate α_i plotted for (a) its positive solution and (b) its negative solution according to (3.105) for $\alpha_r = 1$ and $Re = 1000$. As can be seen, α_i adopts complex values for $\omega \lessapprox 0.866$, which is the value arising for the threshold in (3.110). Above this thresholds α_i is purely positive with a global minimum for $\alpha_{i,-}$ at $\omega = \alpha_r = 1$. 55

3.16 (a) Computation of the real part of the eigenfunction $\tilde{v}_r(y)$ as given in (3.117) for $Re = 100$ and $\alpha_r = \omega = 0.1$, which in figure 3.14b contributed to a maximum amplification rate α_i. Two window plots for the range $y \in [0, 1]$ and $y \in [99, 100]$ are displayed, respectively. (b) Single-sided power spectrum of the eigenfunction acquired from the fast Fourier transformation (FFT) of $\tilde{v}_r(y)$, where the amplitude $|P(f)|$ is plotted versus the wave numbers f. A local maximum corresponding to the wall-normal wave number k_y defined in (3.121) at $f \approx 20.8$ and a global maximum at $f \approx 104.2$ can be observed. 57

4.1 The non-dimensional velocity profile of PCF with wall-transpiration rates from $Re_V = 0$ (classical PCF) to $Re_V = 50$. (adapted from Sun et al. (2022)) 63

4.2 The dimensionless velocity profile of the ASBL with the displacement thickness δ_1 and wall-normal constant suction V_0. (adapted from Sun et al. (2022)) . . . 65

4.3 (a) Temporal stability surface for plane Couette flow with transpiration (PCFT) parametrized by α, Re_V and Re, where every point on the surface corresponds to a neutrally stable mode and points within correspond to unstable modes. (b) Temporal stability surface displayed with a maximum Reynolds number $Re_{max} = 2.0 \times 10^6$, where the surface is projected onto the α-Re-plane and the Re_V-Re-plane, respectively. The critical quadruplet may be referred to in (4.28d). (adapted from Sun et al. (2022)) 68
4.4 Projection of the temporal stability surface from figure 4.3b onto the Re-Re_V-plane in 2D. The critical parameters are given in (4.28d). The red-dashed line marks a threshold at $Re_V \approx 6.71$ below which all modes are stable regardless of Re and α. (adapted from Sun et al. (2022)) 69
4.5 Temporal stability map given at the critical transpiration Reynolds number $Re_{V,cr} = 9.79923$. Shaded areas indicate unstable modes with maximum growth rates of $\omega_{i,max} \approx 2.5 \times 10^{-3}$. The shape of the thumb curve is similar to the corresponding stability map for the ASBL displayed in figure 3.5 (adapted from Sun et al. (2022)) 70
4.6 Temporal (a) and spatial (b) spectrum of PCFT for the critical parameters α_{cr} or ω_{cr}, respectively, as well as $Re_{V,cr}$ and Re_{cr} as given in (4.28d). The neutrally stable TS mode is encircled in blue. In the temporal spectrum, the A-, P- and S-branches are discernible. (adapted from Sun et al. (2022)) 71
4.7 Two additional temporal spectra are depicted for (a) $Re_V = 15$ and (b) $Re_V = 20$. In contrast to figure 4.6a, the $S-$ branch is clearly visible and similarly distorted towards $\omega_r \approx 0.1$. (adapted from Sun et al. (2022)) 72
4.8 Streamwise (a) and wall-normal (b) eigenfunctions $\tilde{u}(y)$ and $\tilde{v}(y)$, respectively, rescaled by the maximum of the streamwise eigenfunction $\tilde{u}(y)_{max}$ for $Re_V = Re_{V,cr}$, $Re_V = 15$ and $Re_V = 20$. (adapted from Sun et al. (2022)) 72

5.1 Flow domain with upper wall velocity U_w, the laminar base profile and a perturbation $\tilde{\boldsymbol{u}}$. The wave and growth mechanics are described with the corresponding angles θ_p and θ_{cr} respectively as defined in (5.26) and (5.28) for oblique 3D modes as defined in equation (5.18) and induced by $\phi < 1$. 81

6.1 A part of the 2D spatial eigenvalue spectrum of PCF with $\omega_{2D} = 0.1$ and $Re_{2D} = 1000$ is displayed for modes with $\alpha_{2D,i} < 5$. All modes employed into (6.1) yield a residuum smaller than $r = 10^{-10}$. The TS mode is encircled in blue. 84
6.2 Amplitudes of eigenfunctions $\tilde{u}(y)$ (a), $\tilde{v}(y)$ (b) and $\tilde{w}(y)$ (c) arising for a transformation of the 2D parameter set in table 6.1, separated into real and imaginary parts. 85
6.3 Perturbation velocity components $u(x, y = 0.5, z = 5)$ (a), $v(x, y = 0.5, z = 5)$ (b) and $w(x, y = 0.5, z = 5)$ (c) displayed in streamwise direction at $y = 0.5$ and $z = 5$ after $t = 200 \approx 9T$, where $T = 2\pi/\omega$, i.e. one period. The index 'a' gives the analytical results, the index 'DNS' gives the results simulated with the nek5000 spectral element method (SEM) code. 89
6.4 Streamwise velocity component $u'(x = 15, y = 0.5, z)$ in Cartesian (a) and semi-logarithmic coordinates (b) displayed in spanwise direction at $y = 0.5$ and $x = 15$ after $t = 200 \approx 9T$, where $T = 2\pi/\omega$, i.e. one period. The index 'a' gives the analytical results, the index 'DNS' gives the results simulated with the nek5000 SEM code. 90

6.5 Wall-normal velocity component $v(x = 15, y = 0.5, z)$ in (a) linear and (b) semi-logarithmic scaling displayed in spanwise direction at $y = 0.5$ and $x = 15$ after $t = 200 \approx 9T$, where $T = 2\pi/\omega$, i.e. one period. The index 'a' gives the analytical results, the index 'DNS' gives the result simulated with the nek5000 SEM code. 90
6.6 Spanwise velocity component $w'(x = 15, y = 0.5, z)$ in (a) linear and (b) semi-logarithmic scaling displayed in spanwise direction at $y = 0.5$ and $x = 15$ after $t = 200 \approx 9T$, where $T = 2\pi/\omega$, i.e. one period. The index 'a' gives the analytical results, the index 'DNS' gives the result simulated with the nek5000 SEM code. 91
6.7 2D contour plot of the wall-normal perturbation velocity component $v(x, y = 0.5, z)$ at half channel height $y = 0.5$ after $t = 200 \approx 9T$, where $T = 2\pi/\omega$, i.e. one period, with the propagation angle θ_p and critical angle θ_{cr} as defined in (5.26) and (5.28). 91

List of Tables

6.1 Transformation of 2D to 3D parameters with Reynolds number ratio $\phi = 0.35$ as transformation parameter according to (5.20) and (5.25). 84
6.2 3D wave characteristics for transformed 3D mode given in table 6.1 84

List of Abbreviations

1D one-dimensional

2D two-dimensional

3D three-dimensional

ASBL asymptotic suction boundary layer

BBL Blasius boundary layer

BC boundary condition

BDF2/EXT2 second order backward differentiation formula and extrapolation

BL boundary layer

CFL Courant–-Friedrichs–-Lewy

DFG German Research Foundation

DNS direct numerical simulation

EVP eigenvalue problem

FEM finite element method

FFT fast Fourier transformation

FST free-stream turbulence

GLL Gauss–Lobatto–Legendre

LNSE linearized Navier–Stokes equations

LSA linear stability analysis

LST linear stability theory

mOSE modified Orr–Sommerfeld equation

mSE modified Squire equation

NMA normal mode ansatz

NSE Navier–Stokes equations

ODE ordinary differential equation

OS Orr–Sommerfeld

OSE Orr–Sommerfeld equation

PCF plane Couette flow

PCFT plane Couette flow with transpiration

PDE partial differential equation

RBC Rayleigh–Bénard convection

SE Squire equation

SEM spectral element method

TBL turbulent boundary layer

TS Tollmien–Schlichting

WDRL wave decay-rate length

1 Introduction

Mankind's interaction with the environment has always constituted a desire to first comprehend, then describe quantitatively and finally control the entirety of all existing physical phenomena. The goals of such control may be manifold and are generally dictated by the spirit of the respective era. As the situation presents itself in the present times, the pressing challenge of the prevailing century is the anthropogenic climate change and its disastrous effects on the environment, humans and nature in its entirety. It is certainly not exaggerated to declare that limiting global warmth preferably to 1.5° C or 2° C at most compared to the pre-industrial era is crucial to maintain a habitable planet Earth and prevent extreme climates (UN, 2015).
A trivial way out of the dilemma of an ever-increasing demand for energy and the necessity of reducing the emission of CO_2 clearly would be the emergence of novel inexhaustible methods of green energy production, such as nuclear fusion, in order to satisfy the global energy demand and halt climate change. In the foreseeable future, however, humanity must rely on more conventional methods of tackling climate change, that is, increasing the usage of conventional green energy production, limiting the usage of fossil fuels by law, for instance by capping CO_2-emissions by specific thresholds, and improving the efficiency of traditional technologies. In almost all aspects of energy production, fluid mechanics plays a significant role in achieving higher degrees of efficiency. In this aspect, the understanding of turbulence as one of the main reasons of energy loss due to increased friction is indispensable. For this, one must be able to correctly predict turbulence and describe the structures emerging in a turbulent flow. The present dissertation attempts to contribute to these specific points with the following chapters.

1.1 Large-scale structures in laminar and turbulent flows

The scientific research of the present dissertation is embedded in the priority programme SPP1881: *Turbulent Superstructures*, funded by the German Research Foundation (DFG). The goal of this research program is to thoroughly describe, understand and control large-scale turbulent structures, so called turbulent superstructures. This term was first coined by Hutchins and Marusic (2007) in a seminal paper, in which the authors both experimentally and numerically verified the existence of clustered structures aligned in streamwise direction in the near-wall region. These results are quite remarkable, as turbulent flows are generally thought of as chaotic and rather arbitrary. Certain statistical turbulent flow features, such as the mean velocity $\overline{U}$, classically represent the very few ordered and regular features of an otherwise chaotic phenomenon. However, the mechanisms leading to the formation of such large-scale structures are not yet understood thoroughly to date.
Despite the novel terminology, the presence of large-scale motions in turbulent boundary layer (TBL) was described decades ago by Kovasznay et al. (1970), made possible by the emergence

of conditional sampling and conditional averaging methods in experimental fluid mechanics. In the elaborations a clear interrelation between the motion of the interface separating the turbulent and non-turbulent regimes in intermittent turbulence and the clustering of large-scale motions in the turbulent patches could be deduced. It is quite fascinating how the forming and movement of exclusively turbulent features, specifically persisting large-scale turbulent motions, are influenced by intermittency, which in itself outlines the presence or non-presence of turbulence in a spatiotemporal regime. Observations of this sort are invaluable for the quantitative and structural understanding of turbulence, which otherwise is confined by the infamous closure problem. Similar observations of turbulent superstructures were also made by Nakagawa and Nezu (1981), who in an open-channel flow could extract bursting large-scale motions in experiments via new sampling analysis methods.
In all of these results resides the question: from where do these large-scale persisting turbulent superstructures originate? In this context, it is convenient to consider turbulent Rayleigh–Bénard convection (RBC), which represents the convective flow forming between two plates, the lower heated and the upper cooled. While laminar RBC features ordered convection cells both in two-dimensional (2D) and three-dimensional (3D), these ordered structures break up in turbulent RBC and seemingly distort into chaotic patterns. It was shown, however, that the instantaneous chaos in turbulent RBC possesses large-scale dynamics classifiable as turbulent superstructures (Getling, 1998; Bodenschatz et al., 2000; Ahlers et al., 2009). Remarkably, in a recent work by Pandey et al. (2018) weakly turbulent RBC fields were found to yield cell-like structures reminiscent of the convection patterns occurring at much smaller Rayleigh numbers and thus in linear or weakly non-linear regimes. The laminar convection patterns, in turn, are results of linear instabilities in the non-convective state, i.e. when viscous forces dominate buoyancy and heat is transferred via conduction rather than convection. Thus, these results strongly hint at a link between large-scale motions in turbulent flows and linear instabilities in the laminar base state.
Throughout this thesis, the asymptotic suction boundary layer (ASBL) is discussed extensively, for which fluctuations with large-scale streamwise wavelengths were found to be the most energetic in pre-multiplied energy spectra by Khapko et al. (2016). Time-averaged turbulent superstructures in the form of large and wide streamwise rolls were further discovered by Kraheberger et al. (2018) for plane Couette flow (PCF), which is the other canonical flow examined in this dissertation. For sufficiently large Reynolds numbers, counter-rotating rolls covering the entire spanwise direction of the computational boxes are uncovered via time-averaging of the turbulent velocity field. Curiously, the rolls persist even for increasingly large transpiration rates and seem to be of universal nature rather than spontaneous occurrences. The diameter of these counter-rotating rolls are as large as the characteristic length scale, i.e. the distance between both walls, similar to the aforementioned large-scale motions in TBL. Furthermore, these rolls effectively outlive all transient phenomena in the flow, proving to be long-lived enough to classify as turbulent superstructures. There is a strong suspicion that their origin also lies in the laminar regime, wherein linear modes seem to persist transition to turbulence and thereof evolve into large-scale turbulent structures.

To sum up the hitherto available insights, two important pieces of information may be extracted from these results:
(i) While instantaneous small-scaled transient turbulent fluctuations serve little to no role in global transportation phenomena, large-scale persisting turbulent superstructures are essential for global mass and heat transfer in a flow, as was demonstrated for RBC by Bodenschatz et al.

(2000) and Pandey et al. (2018). This implies that the understanding of the forming as well as the temporal development of these structures are vital in order to reasonably predict the mass and heat transfer not only of canonical flows but also of technical fluid applications or atmospheric motions.
(ii) The results of Pandey et al. (2018) and Kraheberger et al. (2018) strongly hint that the origin of turbulent superstructures are to be discovered in the laminar base states of respective flow problems. Classical linear stability analysis (LSA) can be used to analyze flows superposed by small perturbations in order to predict the growth of respective perturbation modes. As will be demonstrated throughout the present dissertation, LSA utilized on canonical shear flows addressed in the present thesis, namely PCF and the ASBL, as well as multiple other flow problems gives rise to numerous novel insights on the emergence and growth mechanics of infinitesimal perturbations. The respective results may be extended by employing weakly non-linear methods, which for aforementioned RBC was utilized by Schlüter et al. (1965) in order to predict the dynamics of finite amplitude perturbations. As the title of this thesis indicates, attention hereafter shall be focused to the ASBL and PCF.

1.2 Revisiting linear stability analysis for wall-bounded canonical shear flows examplified by plane Couette flow and the asymptotic suction boundary layer

One of the key results of the research established in the present thesis emerged from the analytical study of the linear stability problem of the ASBL. It could be shown via asymptotic methods that very long streamwise perturbations are limited in their length by the corresponding Reynolds number of the problem. Even more remarkable is a distinct functional interrelation of this length-threshold and the Reynolds number of the problem. These results coincide with the aforementioned work by Khapko et al. (2016) as well as very recent experimental observations made for the turbulent ASBL by Ferro et al. (2021), who both uncovered energy maxima in pre-multiplied power density spectra at large streamwise wavelengths, i.e. corresponding to turbulent superstructures, for Reynolds numbers of same order in the near-wall region. Evidently, this was worked out analytically in Yalcin et al. (2021) as elaborated. In this work the present author also derived continuous spectra for the temporal stability problem of the 2D ASBL, which proved to be stable regardless of the flow parameters. However, a shift of framework to the spatial stability problem disclosed spatial continuous spectra which for very specific parameters do in fact become unstable. To the best knowledge of the author unstable continuous spectra were not detected for other classically examined canonical shear flows. Additionally, the existence of novel ansatz functions for the linearized Navier-Stokes equations were analyzed based on derivations by Mirzayev (2016) in an unpublished bachelor thesis. These analyses in turn are based on group theoretical examinations by Nold et al. (2015), where optimal systems of symmetries of the inviscid linearized Navier-Stokes equations yielded aforementioned novel ansatz functions for plane shear flows in general. The application of the presented techniques gave rise to double-exponential and alternative exponential ansatz functions for the ASBL.
The effect of transpiration was studied further in both a temporal and spatial LSA for plane Couette flow with transpiration (PCFT) in a supervised unpublished master thesis by Sun (2020). While conventional PCF is known to be linearly stable for all Reynolds numbers, as was

proven by Romanov (1973), the same setup with constant wall-transpiration turns unstable at a specific transpiration Reynolds number. It could be shown that transpiration, in contrast to stabilization of boundary layer (BL) via suction, leads to destabilization of PCF. Floryan (2003) showed previously how harmonic transpiration at the lower-wall of PCF induce instabilities. These results were complemented in the present research by considering the case of global and constant wall-transpiration, which evidently also induces instabilities at large enough transpiration rates. Remarkably, PCFT is demonstrated to be mathematically equivalent to the ASBL for the infinite limit of the transpiration Reynolds number. This yields the stability analysis of PCFT with large transpiration Reynolds numbers superfluous, which is then covered by the ASBL.
The last major topic of this thesis is the discussion of novel oblique modes for wall-bounded shear flows. The respective results are discussed in chapter 5. Via extension of the classical Squire's transformation for the temporal stability problem to the spatial framework, novel modes with oblique growth mechanics are derived. Where conventional linear modes are globally stable for PCF, the inclusion of spanwise growth rates induce a perturbation field which quite possibly experiences growth for certain angles in the wall-parallel plane. The framework was also applied to the ASBL, which upon assumption of spanwise growth rates yield linear modes with subcritical Reynolds numbers. The stabilizing effect of suction for BL may, based on the present results, be subjected to a misconception. A distinction is therefore necessary, as suction clearly does stabilize BLs flows when assuming purely streamwise growth rates, as was also proven experimentally by Fransson and Alfredsson (2003). Oblique modes, however, seem to bypass the self-evident stabilization of suction. Bypass transition was observed for the ASBL at Reynolds numbers as low as $Re = 333$ in large-eddy simulations by Schlatter and Örlü (2011). It is well within the realms of possibility that bypass transition is triggered by the presence of oblique modes such as the ones discussed in this thesis.
Finally, the results in chapter 5 are backed by direct numerical simulation (DNS) conducted with the open-source code *nek5000* by Fischer et al. (2008) in chapter 6, which employs a high-order spectral element method (SEM) scheme implemented by nodal Lagrange polynomial basis functions interpolated on Gauss–Lobatto–Legendre (GLL) points. The simulations verify the validity of the derived oblique modes for PCF and prove that oblique patterns similar to known laminar-turbulent stripe patterns emerge (Barkley and Tuckerman, 1999; Barkley and Tuckerman, 2005; Tuckerman and Barkley, 2011).

1.3 Outline

The following chapters of the present doctoral thesis are inaugurated by chapter 2, in which theoretical backgrounds all succeeding chapters have in common, i.e. a derivation of the Navier-Stokes equation, its linearization and non-dimensionalization as well as the derivation of equations of linear stability and corresponding equations and transformations are presented. Chapter 3 revisits temporal and spatial linear stability analysis for the ASBL and introduces novel unstable spatial continuous modes. The destabilizing effect of transpiration on PCF is studied in chapter 4, where additionally for large transpiration rates a unique transformation to the ASBL is presented. An extension of the framework of linear stability in terms of modes with oblique growth is introduced in chapter 5. These modes are verified in direct numerical simulations presented in chapter 6. A conclusion and outlook based on the present results is lastly presented in chapter 7. Several chapters are backed by the appendix.

2 Basic equations of linear stability theory

Stability theory represents the mathematical framework that is employed to predict the temporal or spatial evolution of perturbations introduced into or emerging in a system. The idea itself is not restricted to fluid dynamics, but may be applied to different fields of physics, such as thermodynamics or structural mechanics. Correspondingly, a thermodynamic system may become unstable due to a perturbation in temperature while a mechanical structure may feature instabilities due to harmonic or quasi-harmonic displacements. As the focus in the following chapter is going to be on plane shear flows, the governing equations will be restricted to the introduction of hydrodynamic stability theory. For this, the basic conservation laws, for momentum and mass in particular, are discussed in the framework of continuum mechanics and extended to the famous Navier–Stokes equations (NSE) by the inclusion of material laws. Thereof, the linearized Navier–Stokes equations (LNSE) are derived by a perturbation ansatz, which then are transformed to two partial differential equation (PDE) for the wall-normal perturbation velocity and vorticity, respectively.
Classical stability theory then is commenced in form of the Orr–Sommerfeld equation (OSE) and Squire equation (SE), which are obtained from the LNSE by employing the normal mode ansatz (NMA), which mathematically represents a Fourier-Laplace transformation. The OSE and SE framework is supplemented by the Squire's transformation, which represent symmetry transformations between the respective two-dimensional (2D) and three-dimensional (3D) spectral parameters arising due to the Fourier-Laplace transformation. This theoretical framework will form the basis for the analyses conducted and discussed in the subsequent chapters on the linear stability analysis (LSA) of the asymptotic suction boundary layer (ASBL) and plane Couette flow (PCF) with and without wall-transpiration, respectively.

2.1 Continuum mechanics

A gas or liquid is ideally described in field theory by assuming all field quantities to be defined at every point of the domain via local spatial and statistical averaging at a molecular level. Naturally, however, not every infinitesimally small point in a domain is occupied by gas molecules and thus defining fluid velocity, for instance, as an averaged field quantity may be erroneous. In such cases, it would be more sensible to describe the statistical behavior of such thermodynamic systems, for instance by the Boltzmann equation (Boltzmann, 1872). The corresponding equations and ensuing statistical descriptions of fluid behavior on a molecular level, however, are unnecessarily complex for most flows and fluid applications. It is more convenient, if applicable without grave errors in all field points, to regard the flow domain as a continuum, in which above mentioned field quantities are spatially averaged in a continuous field, allowing for the calculation of local gradients of such fields.

The justification of such approach is given if the mean free path λ, denoting the mean length of particle collisions, is sufficiently small in relation to a problem specific length scale L, i.e.

$$Kn := \frac{\lambda}{L} \ll 1, \tag{2.1}$$

where Kn denotes the Knudsen number. Figure 2.1 conceptually depicts the mean free path λ and a problem specific length scale, here a circular flow domain of diameter L, which could be the inside of a balloon. The molecules in the domain both oscillate and have the instantaneous velocity $\boldsymbol{v}$. The thermodynamics state of the medium inside the domain is described by the pressure p of the gas as well as the temperature T, which correlates to the intensity of oscillations and the molecular velocity. As such, the mean free path is dependent on these molecular phenomena as well as the size of the molecules, expressed by the mean molecule diameter d. For ideal gases the mean free path thus is given by

$$\lambda = \frac{k_B T}{2^{\frac{1}{2}} \pi d^2 p}, \tag{2.2}$$

where k_B additionally denotes the Boltzmann constant, one of the fundamental constants of statistical mechanics. Karniadakis et al. (2006) specifies the range in which the continuum

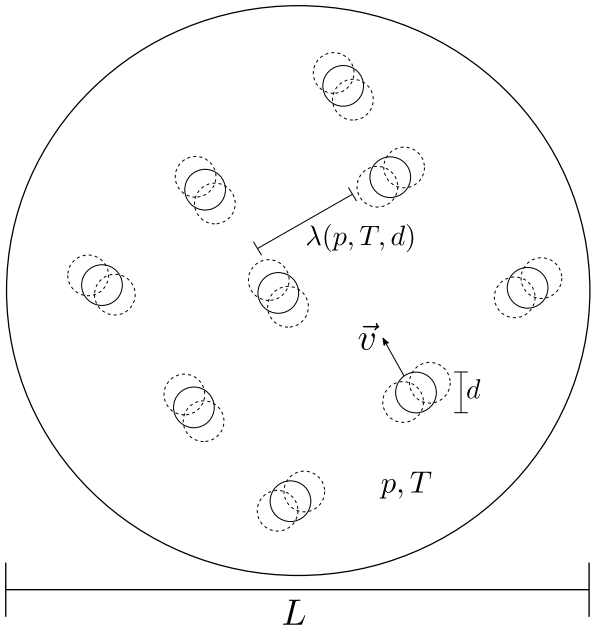

Figure 2.1: Molecules of diameter d in a domain with the characteristic length L, the pressure p and temperature T oscillate and have the instantaneous velocity $\boldsymbol{v}$. The likelihood of collisions is quantified by the mean free path $\lambda(p, T, d)$.

hypothesis applies as

$$Kn \leq 0.01, \tag{2.3}$$

whereas the later described NSE already apply for

$$Kn \leq 0.1. \tag{2.4}$$

The Knudsen number range in between, i.e. $0.01 < Kn < 0.1$, is called the slip flow region, for which the classical no-slip boundary condition (BC) must be replaced by a slip BC. In

order to explain the use of the continuum hypothesis hereafter, a short calculation discussed in Pope and Pope (2000) is depicted. For air under atmospheric conditions, the mean free path between the molecules is approximately $\lambda = 6 \times 10^{-8}$ m. Typical length scales in common fluid applications are rarely smaller than $L = 10^{-4}$ m $= 0.1$ mm. Employing these lengths into (2.1) gives $Kn = 0.0006 \ll 1$ and thus justifies the assumption of continuum mechanics. The following flow problems are assumed to generally combine characteristic lengths scales and mean free paths such that the Knudsen numbers are not entering the slip flow region, which would demand refined BC. Instead, no-slip BC are employed for wall-bounded shear flows.

2.2 Conservation laws

The assumption of continuum mechanics due to the prevalence of sufficiently low Knudsen numbers as defined in (2.1) gives rise to one of the central and most powerful concepts of field theory, i.e. conservation laws. They state that certain quantities in a closed domain may not appear from nowhere or disappear into the void and are therefore conserved. An increase or decrease of the corresponding quantity is only possible via production or annihilation of the same inside the domain or via flux over the boundaries. It shall be noted that, in addition to the now discussed conservation laws of mass and momentum, there exist conservation laws for energy, angular momentum or vorticity, among numerous others for incompressible fluids (see e.g. Caviglia and Morro (1989)). The notation and following presentation of basic equations in continuum mechanics are based on derivations given in Spurk and Aksel (2010). A thorough in-depth derivation of the now following principles shall be referred to there.

2.2.1 Continuity equation

Certainly, conservation of mass represents the most comprehensible and plausible conservation law. Upon considering a time-dependent material surface, the mass without production or destruction (e.g. via matter-antimatter annihilation) and flux over the boundaries is a conserved quantity, which translates to

$$\frac{\mathrm{D}}{\mathrm{D}t} \iiint\limits_{V(t)} \rho \, \mathrm{d}V = 0, \tag{2.5}$$

where

$$\frac{\mathrm{D}}{\mathrm{D}t} := \frac{\partial}{\partial t} + u_i \frac{\partial}{\partial x_i}, \tag{2.6}$$

denotes the material derivative. Notice that the Einstein index notation is introduced here, where $i \in [1, 2, 3]$ describes the three principal directions in a Cartesian coordinate system. Moreover, the Einstein summation convention

$$a_i a_i = a_1^2 + a_2^2 + a_3^3, \tag{2.7}$$

is employed throughout the present thesis.
At any given instance t, the time-dependent volume $V(t)$ in (2.5) is equal to a constant volume V, which enables drawing the total derivative under the integral, yielding

$$\iiint\limits_{V} \left(\frac{\partial \rho}{\partial t} + \frac{\partial}{\partial x_i} \left(\rho u_i \right) \right) \mathrm{d}V = 0, \tag{2.8}$$

where u_i denotes the convective velocity. Reintroducing (2.6) and applying the chain rule of differentiation to (2.8) yields

$$\iiint_V \left(\frac{\mathrm{D}\rho}{\mathrm{D}t} + \rho \left(\frac{\partial u_i}{\partial x_i} \right) \right) \mathrm{d}V = 0. \tag{2.9}$$

Now, (2.8) as well as (2.9) must hold for any integral bound and thus must be zero regardless of the volume chosen. This is always the case for vanishing integrands

$$\frac{\partial \rho}{\partial t} + \frac{\partial}{\partial x_i} (\rho u_i) = 0, \tag{2.10a}$$

$$\frac{\mathrm{D}\rho}{\mathrm{D}t} + \rho \left(\frac{\partial u_i}{\partial x_i} \right) = 0. \tag{2.10b}$$

Both equations are equivalent, but (2.10b) is more useful in order to discuss incompressibility. A fluid is usually considered incompressible for low enough Mach numbers $M \ll 1$, where M is defined as

$$M := \frac{u}{c}, \tag{2.11}$$

with u describing the local velocity and c denoting the speed of sound (Acheson, 1990). In turn, an incompressible fluid by definition is one of constant density ρ. Employing a constant ρ into (2.10b) gives

$$\frac{\partial u_i}{\partial x_i} = 0, \tag{2.12}$$

or

$$\nabla \cdot \boldsymbol{u} = 0, \tag{2.13}$$

where

$$\boldsymbol{u} = (u_1, u_2, u_3)^T, \tag{2.14a}$$

$$\nabla = \left(\frac{\partial}{\partial x_1}, \frac{\partial}{\partial x_2}, \frac{\partial}{\partial x_1} \right)^T, \tag{2.14b}$$

which states that the divergence of the velocity field is zero. In other words, an incompressible fluid corresponds to a divergence-free velocity field. The corresponding continuity equation is given by (2.12). The entirety of results in this thesis is based on the assumption of incompressibility of the examined flows. For this reason, divergence-free velocity fields are going to be presupposed in the upcoming sections and chapters.

2.2.2 Momentum equation

The central equations of fluid mechanics, the NSE, embody both the conservation of mass as well as the momentum equation. The momentum I_i of a particle of mass m is defined as

$$I_i := m u_i, \tag{2.15}$$

where u_i denotes the velocity of the particle in the direction x_i. In continuum mechanics, rather than considering the momentum of a particle, the concept is extended to a fluid body of volume $V(t)$, where the momentum is then given by

$$I_i = \iiint_{V(t)} \rho u_i \mathrm{d}V, \tag{2.16}$$

with $u_i = u_i(x_1, x_2, x_3, t)$ now instead representing the local velocity of a specific field point. Conservation of momentum now states that in absence of forces on the volume the momentum of the material volume $V(t)$ is conserved, i.e.

$$\iiint_V \frac{\mathrm{D}u_i}{\mathrm{D}t} \rho \, \mathrm{d}V = 0. \tag{2.17}$$

A change of momentum, according to Newton's second axiom, occurs via surface forces t_i on the boundary S or volume forces k_i across the entire volume V, giving the momentum equation

$$\iiint_V \frac{\mathrm{D}u_i}{\mathrm{D}t} \rho \, \mathrm{d}V = \iint_S t_i \rho \, \mathrm{d}S + \iiint_V k_i \rho \, \mathrm{d}V. \tag{2.18}$$

The surface force vector t_i may be expressed as a linear map of the surface normal vector n_i through the Cauchy stress tensor τ_{ij}, expressing itself as

$$t_i = \tau_{ji} n_j. \tag{2.19}$$

Utilizing Gauss's theorem makes it possible to transform the surface integral in (2.18) after employing (2.19) into a volume integral, yielding

$$\iiint_V \left(\rho \frac{\mathrm{D}u_i}{\mathrm{D}t} - \rho k_i - \frac{\partial \tau_{ji}}{\partial x_j} \right) \mathrm{d}V = 0. \tag{2.20}$$

Analogous to arguments used to derive the differential form of the conservation of mass, the integral in (2.20) yields zero regardless of the integration boundaries if its integrand disappears, i.e.

$$\rho \frac{\mathrm{D}u_i}{\mathrm{D}t} = \rho k_i + \frac{\partial \tau_{ji}}{\partial x_j}. \tag{2.21}$$

This momentum equation is famously called Cauchy's momentum equation and together with (2.12) forms the basis for deriving the NSE. It shall be noted, before introducing material laws, that (2.21) may be extended to an accelerated frame of reference. As such accelerated systems are of no interest for the upcoming results, the interested reader is referred to respective literature (see e.g. Spurk and Aksel (2010)).

2.3 Navier-Stokes equations

The following derivation is based on Batchelor and Batchelor (2000) and Spurk and Aksel (2010) and is by no means as elaborate. For a more in-depth derivation, the reader is referred to these books in good conscience. The first step towards the Navier-Stokes equations of motion

is to regard the stress tensor τ_{ij} as the sum of an isotropic part $-p\delta_{ij}$ and the deviatoric stress tensor d_{ij}. It would be of great convenience to express d_{ij} in terms of quantities formed by the fluid velocity u_i. According to Batchelor and Batchelor (2000), for isotropic Newtonian fluids the deviatoric stress may readily be expressed by

$$d_{ij} = 2\mu e_{ij} + \mu'' e_{kk}\delta_{ij}, \tag{2.22}$$

where μ and μ'' are scalars, δ_{ij} describes the Kronecker delta and e_{ij} denotes the rate-of-strain tensor given by

$$e_{ij} = \frac{1}{2}\left(\frac{\partial u_i}{\partial x_j} + \frac{\partial u_j}{\partial x_i}\right). \tag{2.23}$$

Employing

$$\tau_{ij} = -p\delta_{ij} + d_{ij} = -p\delta_{ij} + 2\mu e_{ij} + \mu'' e_{kk}\delta_{ij}, \tag{2.24}$$

into (2.21) gives

$$\rho\frac{\mathrm{D}u_i}{\mathrm{D}t} = \rho k_i + \frac{\partial}{\partial x_i}\left(-p + \mu''\frac{\partial u_k}{\partial x_k}\right) + \frac{\partial}{\partial x_j}\left(\mu\left[\frac{\partial u_i}{\partial x_j} + \frac{\partial u_j}{\partial x_i}\right]\right). \tag{2.25}$$

As the problems analyzed in this work neglect temperature, and thus spatial or temporal, dependence of μ and μ'', the r.h.s. of (2.25) can be rewritten so that

$$\rho\frac{\mathrm{D}u_i}{\mathrm{D}t} = \rho k_i - \frac{\partial p}{\partial x_i} + (\mu + \mu'')\frac{\partial u_k}{\partial x_k} + \mu\frac{\partial^2 u_i}{\partial x_j \partial x_k}. \tag{2.26}$$

Assuming incompressibility as per (2.12) now yields the divergence terms zero, which finally gives the incompressible Navier-Stokes equations of motion

$$\frac{\mathrm{D}u_i}{\mathrm{D}t} = k_i - \frac{\partial p^*}{\partial x_i} + \nu\frac{\partial^2 u_i}{\partial x_j \partial x_k}, \tag{2.27}$$

where $p^* = p/\rho$ is the pressure re-scaled by the constant density and $\nu = \mu/\rho$ denotes the kinematic viscosity of the considered fluid. The incompressible NSE are complemented by the continuity equation (2.12) to form a set of four PDE, of which the three NSE of motion are non-linear.

In many flow problems it is furthermore justified to neglect the body forces if gravitational forces are small compared to inertial forces and shear stress. This gives the form of the NSE which is used throughout this thesis, i.e.

$$\frac{\partial u_i}{\partial t} + u_j\frac{\partial u_i}{\partial x_j} = -\frac{\partial p}{\partial x_i} + \nu\frac{\partial^2 u_i}{\partial x_j^2}, \tag{2.28a}$$

$$\frac{\partial u_i}{\partial x_i} = 0, \tag{2.28b}$$

where the star notation for p will be omitted hereafter for the sake of readability.

For problems with rotational symmetry, such as Hagen-Poiseuille flow, i.e. the flow driven through a circular pipe due to a pressure gradient, it is convenient and possible to rewrite these equations in polar coordinates. There are all sorts of specific flow problems, for which a change of coordinate system may prove to be useful. For spirally developing flows, for instance, a helical coordinate system proves to be handy to derive new conservation laws, as was shown by Kelbin et al. (2013). As no such flow is analyzed in the present dissertation, the listing of other representations of the NSE shall be referred to in respective literature, e.g. Batchelor and Batchelor (2000).

2.3.1 Non-dimensional Navier-Stokes equations

A powerful concept in fluid dynamics in particular and in physics generally is similitude. Every system must be independent of the unit system. Whether a physical quantity is expressed in imperial or metric units must not have any influence on the actual physics of the respective system. In conclusion, a system is unequivocally described if all dependents and independents are dimensionless. The ultimate goal in similitude is to extract the essential dimensionless numbers describing the behavior of the underlying physics of the respective system. In engineering applications, this relates to the question, which quantities need to be adjusted so that two independently conducted model experiments may become comparable despite differences in size, velocity or viscosity of the fluid.
The first notion of dimensional analysis in fluid mechanics was published by Reynolds (1883), after whom the famous Reynolds number is named. To understand the concept, consider the NSE (2.28). The first goal is to non-dimensionalize the variables for space, time, velocity and pressure. In a typical flow problem, convenient quantities for non-dimensionalization are the characteristic length scale L_c, such as the diameter of a pipe, as well as the characteristic velocity scale U_c, e.g. the free-stream velocity U_∞ for a boundary layer flow. The corresponding non-dimensional quantities then are

$$x_i^+ = \frac{x_i}{L_c}, \quad u_i^+ = \frac{u_i}{U_c}, \quad t^+ = t\frac{U_c}{L_c}, \quad p^+ = \frac{p}{U_c^2}, \tag{2.29}$$

where the plus sign in the superscript indicates that the corresponding quantity is dimensionless. Substituting (2.29) into the NSE (2.28) yields

$$\frac{\partial u_i^+}{\partial t^+} + u_j^+ \frac{\partial u_i^+}{\partial x_j^+} = -\frac{\partial p^+}{\partial x_i^+} + \frac{1}{Re}\frac{\partial^2 u_i^+}{\partial {x_j^+}^2}, \tag{2.30a}$$

$$\frac{\partial u_i^+}{\partial x_i^+} = 0, \tag{2.30b}$$

where

$$Re = \frac{U_c L_c}{\nu}, \tag{2.31}$$

represents the Reynolds number, which symbolizes the relation of inertial forces to friction forces. This is the aforementioned dimensionless number, which represents similarity between systems and experiments. If a model with the characteristic length scale L_c is experimented on in a wind tunnel with the characteristic velocity scale U_c is compared to a similarly shaped object of half the size in a wind tunnel with twice the characteristic velocity U_c, then both Reynolds numbers are identical and the experiments are representative of one another. Comparability of analyses, experiments and numerical studies is highly important in the field of science, and establishes a framework, in which the actual physics are in the foreground rather than the unit system. Further literature on the topic of dimensional analysis in fluid applications may be referred to in Simon et al. (2017) and Chemloul (2020).
Henceforth, the non-dimensional form of the NSE (2.30) is employed throughout this thesis. Furthermore, for the sake of brevity the plus superscripts are omitted hereafter. With the non-dimensional equations, the equations of linear stability theory (LST) are finally introduced hereafter.

2.4 Equations of linear stability theory

The theory of linear stability is, by definition, a framework employing the simplifications achieved by the linearization of differential equations. For this, the fluid is assumed to be superposed by perturbations of lower order of magnitude, which allows for a separation of the NSE in (2.28) into leading order and lower orders, which may be solved hierarchically. The success of perturbation methods in fluid mechanics is manifold, with LST forming a mere subset of many successful analyses, which may be referred to in full detail in Van Dyke (1975). Applying perturbation theory to the NSE gives rise to a set of four linear PDE, which is easier to acquire solutions from than the non-linear NSE (2.28). Via cross-differentiation it is then possible to obtain a single PDE of fourth order for the wall-normal velocity. Finally, the employment of the NMA yields an ordinary differential equation (ODE) of four order, which in a few special cases provide analytical solutions. Two such cases are the ASBL and PCF with or without transpiration, which are analyzed throughout this dissertation.

2.4.1 Linearized Navier-Stokes equations

Linear stability theory commences where a laminar base state $\{U_i(x,y,z,t), P(x,y,z,t)\}$ of the NSE (2.28) is superposed by perturbation terms $\{u_i'(x,y,z,t), p'(x,y,z,t)\}$ of lower order $O(\epsilon)$, i.e.

$$u_i(x,y,z,t) = U_i(x,y,z,t) + \epsilon u_i'(x,y,z,t) + O(\epsilon^2), \tag{2.32a}$$
$$p(x,y,z,t) = P(x,y,z,t) + \epsilon p'(x,y,z,t) + O(\epsilon^2). \tag{2.32b}$$

Employing (2.32) into the NSE in (2.28) yields

$$\frac{\partial}{\partial t}\left(U_i + \epsilon u_i'\right) + \left(U_i + \epsilon u_i'\right)\frac{\partial}{\partial x_j}\left(U_i + \epsilon u_i'\right) = \frac{\partial}{\partial x_i}\left(P + \epsilon p'\right) + \nu\frac{\partial^2}{\partial x_j^2}\left(U_i + \epsilon u_i'\right), \tag{2.33a}$$
$$\frac{\partial}{\partial x_i}\left(U_i + \epsilon u_i'\right) = 0. \tag{2.33b}$$

As is evident, there are terms scaling with various orders of ϵ. It is now possible to categorize the terms in (2.33) depending on their scaling factor ϵ^n with $n = \{0, 1\}$. This gives

$$O(\epsilon^0): \quad \frac{\partial U_i}{\partial t} + U_j\frac{\partial U_i}{\partial x_j} = \frac{\partial P}{\partial x_i} + \nu\frac{\partial^2 U_i}{\partial x_j^2}, \quad \frac{\partial U_i}{\partial x_i} = 0, \tag{2.34a}$$

$$O(\epsilon^1): \quad \frac{\partial u_i'}{\partial t} + U_j\frac{\partial u_i'}{\partial x_j} + u_j'\frac{\partial U_i}{\partial x_j} = \frac{\partial p'}{\partial x_i} + \nu\frac{\partial^2 u_i'}{\partial x_j^2}, \quad \frac{\partial u_i'}{\partial x_i} = 0. \tag{2.34b}$$

The base state $\{U_i, P\}$ solves the 0th order equation identically. Thereupon, the first order equation is comprised of a set of four linear PDE in the sought perturbation quantities u_i' and p'. Evidently, (2.34b) must be solved after (2.34a) due to $\{U_i, P\}$ appearing therein. Equations

(2.34b) form the LNSE, which represent the starting point of LST. One usually is now interested in exact solutions for the perturbation quantities $\{u_i', p'\}$. As the equations at hand are a set of four PDE with the four unknowns $\{u_1', u_2', u_3', p'\}$, further simplifications are required to yield these equations analytically accessible.

2.4.2 Orr-Sommerfeld and Squire equations

In order to obtain the famous OSE and SE of LST, it is necessary to assume the base flows to be wall-normal parallel shear flows only dependent on the wall-normal coordinate y, i.e.

$$U_i = (U(y), 0, 0)^T . \tag{2.35}$$

Employing (2.35) into (2.34b) yields

$$\frac{\partial u}{\partial t} + U\frac{\partial u}{\partial x} + v\frac{\mathrm{d}U}{\mathrm{d}y} = -\frac{\partial p}{\partial x} + \frac{1}{Re}\Delta u, \tag{2.36a}$$

$$\frac{\partial v}{\partial t} + U\frac{\partial v}{\partial x} = -\frac{\partial p}{\partial y} + \frac{1}{Re}\Delta v, \tag{2.36b}$$

$$\frac{\partial w}{\partial t} + U\frac{\partial w}{\partial x} = -\frac{\partial p}{\partial z} + \frac{1}{Re}\Delta w, \tag{2.36c}$$

$$\frac{\partial u}{\partial x} + \frac{\partial v}{\partial y} + \frac{\partial w}{\partial z} = 0, \tag{2.36d}$$

where from now on $(u, v, w, p)^T = (u_1', u_2', u_3', p')^T$ as well as $(x, y, z, t)^T = (x_1, x_2, x_3, t)^T$ is adopted as the notation for the sought quantities in LST and

$$\Delta = \frac{\partial^2}{\partial x^2} + \frac{\partial^2}{\partial y^2} + \frac{\partial^2}{\partial z^2}, \tag{2.37}$$

represents the Laplacian differential operator. Taking the divergence of equations (2.36a) - (2.36c) yields

$$2\frac{\mathrm{d}U}{\mathrm{d}y}\frac{\partial v}{\partial x} = -\Delta p, \tag{2.38}$$

where, implicitly, the continuity equation for the perturbation velocities (2.36d) was used to eliminate the divergence terms. With (2.38) the pressure in (2.36b) can now be eliminated as per

$$\Delta(2.36\text{b}) - \frac{\partial}{\partial y}(2.38), \tag{2.39}$$

which finally yields

$$\left[\left(\frac{\partial}{\partial t} + U\frac{\partial}{\partial x}\right)\Delta - \frac{\mathrm{d}^2U}{\mathrm{d}y^2}\frac{\partial}{\partial x} - \frac{1}{Re}\Delta^2\right] v = 0, \tag{2.40}$$

with the biharmonic operator

$$\Delta^2 = \frac{\partial^4}{\partial x^4} + \frac{\partial^4}{\partial y^4} + \frac{\partial^4}{\partial z^4} + 2\frac{\partial^4}{\partial x^2\partial y^2} + 2\frac{\partial^4}{\partial x^2\partial z^2} + 2\frac{\partial^4}{\partial y^2\partial z^2}. \tag{2.41}$$

As a consequence, the set of four linear PDE (2.36a) - (2.36d) is reduced to a single fourth order PDE for the wall-normal velocity v. Due to (2.40) still being multivariate and in general

terms unsolvable, further simplifications are necessary if analytical solutions are to be obtained. One classical approach to find solutions for PDE in general is to employ ansatz functions, which assume the concrete structure of the sought solution. One famous problem, in which an ansatz function is successfully applied to deliver the desired eigenvalues and -functions, is the Bethe ansatz, a many-body wave function named after Bethe (1931), applied on the one-dimensional (1D)-Heisenberg model to describe the behavior of ferromagnetism. Similar success was achieved for the examination of instabilities in fluid mechanics as the famous NMA was first employed by Orr (1907) and Sommerfeld (1908) to simplify (2.40). The ansatz function mathematically represents a Fourier-Laplace transformation of the variables in space and time. Concretely, it is given by

$$v(x, y, z, t) = \tilde{v}(y)\, e^{i(\alpha x + \beta z - \omega t)}, \tag{2.42}$$

where α and β denote the wave numbers in stream- and spanwise direction, respectively, ω gives the wave frequency and $\tilde{v}(y)$ is the amplitude function. In the most general case, all wave parameters as well as $\tilde{v}(y)$ are complex. It shall be noted that by employing Lie symmetry analysis on the LNSE (2.36), other ansatz functions may be obtained, as was elaborated by Nold and Oberlack (2013) and Nold et al. (2015). The analysis of such symmetry-induced ansatz functions in the context of the ASBL is presented in chapter 3.
The mathematical representation of the NMA implies that a perturbation is harmonic in stream- and spanwise direction as well as in time, grows or decays in these directions and experiences a varying amplitude based on the wall-normal distance y. The insertion of (2.42) into (2.40) consequently yields

$$L_{OS}(\tilde{v}(y)) \equiv \left[iRe(\alpha U(y) - \omega)(\mathrm{D}^2 - k^2) - iRe\alpha U''(y) - (\mathrm{D}^2 - k^2)^2 \right] \tilde{v}(y) = 0, \tag{2.43}$$

where L_{OS} denotes the Orr–Sommerfeld (OS) differential operator, $\mathrm{D}^n = \mathrm{d}^n/\mathrm{d}y^n$ abbreviates the differentiation with respect to y and

$$k = \sqrt{\alpha^2 + \beta^2}, \tag{2.44}$$

gives the magnitude of the wave vector $\boldsymbol{k}$. Whether equation (2.43) is solvable depends on the base solution $U_0(y)$. In fact, for various famous flow problems, such as plane Poiseuille flow, which describes the parabolic flow between two plates driven by a constant pressure gradient, i.e. $U_0(y) = 1 - y^2$ in non-dimensional variables, the OSE (2.43) is unsolvable analytically. In those cases, numerical methods, such as proposed by Orszag (1971), Schmid et al. (2002), and Canuto et al. (2012) are employed, which depending on their effectiveness, may yield solutions with grave errors. For plane Poiseuille flow, Thomas (1953) proposed replacing the OSE by a difference system of same order, for which a critical Reynolds number of $Re_{cr} = 5780$ was computed. Orszag (1971) improved on this result via Chebyshev collocation methods, which will be employed in chapters 3 and 4, to yield $Re_{cr} = 5772.22$. It will be proven in chapter 3, however, that the computation of eigenvalues based on the analytical solution of the (2.43) leads to considerably refined critical Reynolds numbers.
Now, given that a solution for (2.43) was obtained, the challenge prevails how to quantitatively describe the remaining perturbation velocity components u and w. In the case of 2D flows in the x-y plane, the answer is straightforward. The continuity equation (2.12) then reduces to

$$\frac{\partial u}{\partial x} + \frac{\partial v}{\partial y} = 0. \tag{2.45}$$

Assuming the NMA was also employed for the streamwise velocity component, reading

$$u(x,y,t) = \tilde{u}(y)\, e^{i(\alpha x - \omega t)}, \tag{2.46}$$

equation (2.45) then yields

$$i\alpha\tilde{u}(y) + \tilde{v}'(y) = 0, \tag{2.47}$$

where $v'(y)$ denotes the derivative of $\tilde{v}(y)$ with respect to y. Solving (2.47) for $\tilde{u}(y)$ gives

$$\tilde{u}(y) = \frac{i}{\alpha}\tilde{v}(y), \tag{2.48}$$

where the first derivative $\tilde{v}'(y)$ is acquired from the solution of the OSE (2.43). In the more general case, the 3D case with $\beta \neq 0$, a third equation is necessary to obtain the remaining perturbation velocity component w. It would be ideal to simply utilize the LNSE in spanwise direction given in (2.36c). Unfortunately, the pressure perturbation p is unknown and ideally kept out of the system of unknowns, as was accomplished in the derivation of the OSE. Hence, an additional equation is required which both must include the spanwise perturbation velocity w as well as exclude the pressure perturbation p. This may be achieved via cross-differentiation of the stream- and spanwise components of the LNSE, i.e.

$$\frac{\partial}{\partial z}(2.36a) - \frac{\partial}{\partial x}(2.36c). \tag{2.49}$$

In the ensuing equation the difference of the cross-differentiated velocity components in fact form the wall-normal vorticity, i.e.

$$\eta = \frac{\partial u}{\partial z} - \frac{\partial w}{\partial x}. \tag{2.50}$$

As a result, the emerging second order PDE is given by

$$\left[\frac{\partial}{\partial t} + U_0\frac{\partial}{\partial x} - \frac{1}{Re}\Delta\right]\eta = -U_0'\frac{\partial v}{\partial z}. \tag{2.51}$$

Employing the NMA for the wall-normal perturbation vorticity η with identical wave parameters, concretely

$$\eta(x,y,z,t) = \tilde{\eta}(y)\, e^{i(\alpha x + \beta z - \omega t)}, \tag{2.52}$$

and substituting (2.52) into (2.51) gives rise to the Squire equation

$$L_{SE}(\tilde{\eta}(y)) \equiv \left[iRe(\alpha U_0(y) - \omega) - (\mathrm{D}^2 - k^2)\right]\tilde{\eta}(y) = -iRe\beta U_0'(y)\tilde{v}(y), \tag{2.53}$$

with L_{SE} denoting the Squire differential operator, where the solution of the OSE $\tilde{v}(y)$ represents an inhomogeneity in the newly obtained second order ODE for η. As such, a clear hierarchy is established in which solving the OSE first is mandatory. Lastly, the utilization of the NMA is extended to all velocity components, thus

$$\{u,v,w\}(x,y,z,t) = \{\tilde{u},\tilde{v},\tilde{w}\}(y)\, e^{i(\alpha x + \beta z - \omega t)}. \tag{2.54}$$

In summary, the OSE (2.43), the SE (2.53), the continuity equation for the perturbation velocities (2.36d) as well as the definition of the wall-normal vorticity (2.50) form a set of four equations capable of providing well-defined solutions for the four unknowns u, v, w and η.

2.4.3 Temporal and spatial stability

Before introducing the Squire's transformation, the concept of temporal and spatial stability is introduced. So far, the spatial and temporal wave parameters α, β and ω were generalized to be complex. As is going to be demonstrated, the notion of more than one complex wave parameter yields the classical eigenvalue problem (EVP) for the OSE underdetermined. Generally, the OSE (2.43) is solved by a linear solution space of the form

$$\tilde{v}(y) = C_1\tilde{v}_1(y) + C_2\tilde{v}_2(y) + C_3\tilde{v}_3(y) + C_4\tilde{v}_4(y), \tag{2.55}$$

where C_1 to C_4 are integration constants and $\tilde{v}_1$ to $\tilde{v}_4$ are linearly independent solutions of (2.43). The corresponding BC depend on the domain, which is classically wall-bounded, semi-infinite or infinite, as well as the condition at the boundaries, e.g. homogeneous or inhomogeneous Dirichlet-BC or Neumann-BC. For most stability problems, the flows are either wall-bounded or exist in a semi-infinite domain, both for which homogeneous Dirichlet- and Neumann-BC are given. Assume the flow problem is restricted by two rigid walls, located at $y = 0$ and $y = 1$. Furthermore, no-slip and rigid wall BC are assumed. The corresponding BC then are

$$\tilde{v}(y = 0) = 0, \tag{2.56a}$$
$$\tilde{v}(y = 1) = 0, \tag{2.56b}$$
$$\mathrm{D}\tilde{v}(y = 0) = 0, \tag{2.56c}$$
$$\mathrm{D}\tilde{v}(y = 1) = 0. \tag{2.56d}$$

Substituting all four BC in (2.56) into (2.55) then yields

$$C_1A_{11} + C_2A_{12} + C_3A_{13} + C_4A_{14} = 0, \tag{2.57a}$$
$$C_1A_{21} + C_2A_{22} + C_3A_{23} + C_4A_{24} = 0, \tag{2.57b}$$
$$C_1A_{31} + C_2A_{32} + C_3A_{33} + C_4A_{34} = 0, \tag{2.57c}$$
$$C_1A_{41} + C_2A_{42} + C_3A_{43} + C_4A_{44} = 0, \tag{2.57d}$$

where $A_{11} = \tilde{v}_1(0)$ and analogously for all A_{ij}. This establishes a linear system of equations for C_1 to C_4 of the form

$$A_{ij}C_j = [0, 0, 0, 0]^T. \tag{2.58}$$

In fact, more specifically A_{ij} are now functions of the spectral wave parameters and the Reynolds number, i.e.

$$A_{ij}(\alpha, \beta, \omega, Re)\, C_j = [0, 0, 0, 0]^T. \tag{2.59}$$

Equation (2.59) only yields a non-trivial solution if the determinant of A_{ij} is equal to zero, i.e.

$$\mathcal{D}(\alpha, \beta, \omega, Re) := \det(\boldsymbol{A}(\alpha, \beta, \omega, Re)) = 0. \tag{2.60}$$

Notice that the determinant in (2.60) in general is calculated for a 4x4 matrix as given in (2.57). The conditional equation (2.60) is commonly called dispersion relation as well as algebraic EVP. Despite $\mathcal{D}(\alpha, \beta, \omega, Re)$ potentially being a rather long expression, it nevertheless is an algebraic equation in the complex space and can therefore be rewritten as

$$\mathcal{D}(\alpha, \beta, \omega, Re) = \mathcal{D}_r(\alpha, \beta, \omega, Re) + i\,\mathcal{D}_i(\alpha, \beta, \omega, Re) = 0, \tag{2.61}$$

where $\mathcal{D}_r(\alpha, \beta, \omega, Re)$ and $\mathcal{D}_i(\alpha, \beta, \omega, Re)$ denote the real and imaginary part of the dispersion relation. Hence, the stability problem was reduced to two single conditions

$$\mathcal{D}_r(\alpha, \beta, \omega, Re) = 0, \tag{2.62a}$$

$$\mathcal{D}_i(\alpha, \beta, \omega, Re) = 0. \tag{2.62b}$$

This system now consists of generally six unknowns and consists of two equations. The six unknowns are α_r, α_i, β_r, β_i, ω_r and ω_i. If $\alpha \in \mathbb{C}$ is regarded as the solution of (2.62), it is required to appoint rather arbitrary values to the five presumable parameters β_r, β_i, ω_r, ω_i and Re in order to be able to solve for the two unknowns α_r and α_i. The result would be a five-dimensional parameter space, which would be impossible to analyze rationally and presumably the results would be impossible to illustrate in a meaningful manner. It therefore proved to be more convenient and practical to reduce the stability problem such that only one parameter is complex and the other two are real. In those cases, only one parameter (2D flow) or two parameters (3D flow) would need to be predetermined.
In this context, the temporal stability framework is established when assuming

$$\{\alpha, \beta\} \in \mathbb{R}, \qquad \omega \in \mathbb{C}, \tag{2.63}$$

which employed into the NMA (2.42) gives

$$v(x, y, z, t) = \tilde{v}(y)\, e^{i(\alpha x + \beta z - \omega_r t)}\, e^{\omega_i t}. \tag{2.64}$$

Evidently, the real valued wave parameters α, β and ω_r quantitatively describe the harmonics in space and time while ω_i is representative for the growth or decay of the perturbation in time, depending on which sign and value it takes. The real exponential function also explains, why in the NMA (2.42) a minus sign was adopted in front of ω, as then a positive valued ω_i induces growth, which aligns with what one would intuitively expect.
As the essential stability mechanisms are expressed by ω, it is plausible to regard it as the sought solution of (2.62) and thus assign it to be the eigenvalue of interest. As such, the spatial wave numbers α and β as well as the Reynolds number Re merely represent parameters in the stability problem. Equation (2.60) can adequately be rewritten as

$$\mathcal{D}(\omega)_{\alpha,\beta,Re} = 0. \tag{2.65}$$

The principal approach to solving (2.65) is straightforward. For the parameters α, β and Re values of interest are assumed, which in turn are substituted into (2.65). Lastly, the dispersion relation is solved for its complex roots ω, which is generally done numerically with suitable non-linear complex root-finders. In the context of LSA, one is generally interested in the least stable or most unstable eigenvalue, which is called the Tollmien–Schlichting (TS) mode (Tollmien, 1930; Schlichting, 1933). One decisive advantage of utilizing the analytical dispersion relation (2.65) over numerical methods applied on the OSE is the possibility of employing homotopy methods, as is elaborated e.g. in Liao (2003) for nonlinear PDE. In order to understand the concept, consider figure 2.2. The initial challenge is to find the TS mode for α_0 at a fixed Reynolds number. This can be done rigorously by brute-force computation of all complex roots by altering the initial guesses, via employment of other numerical methods such as Chebyshev collocation schemes or extracting values from literature. Either way, once the TS mode $\{\alpha_0, \omega_0\}$ is discovered, it may be extrapolated linearly to obtain the subsequent initial guess ω_1^* for the corresponding $\alpha_k = \alpha_1$. The smaller the interval $\Delta\alpha = \alpha_k - \alpha_{k-1}$ is, the higher the chance

that the complex root solver converges the guess towards the sought TS mode ω_k. The order of extrapolation can be increased with increasing α_k, as then an increasing number of already computed TS modes can be used to extrapolate the subsequent initial guess. The goal always is to compute the entire TS mode curve without the solution curve jumping to the secondary or tertiary curve, for example, which are also visualized in figure 2.2. Once the range $\alpha_0 - \alpha_n$ of interest is finished, the Reynolds number Re, and in 3D computations the spanwise wave number β, may be extrapolated analogously. It is, however, quite tedious to perform these computations additionally in 3D, i.e. for $\beta \neq 0$. Fortunately, the 3D temporal stability problem can be bypassed by the Squire's transformation, which is discussed in the following section.

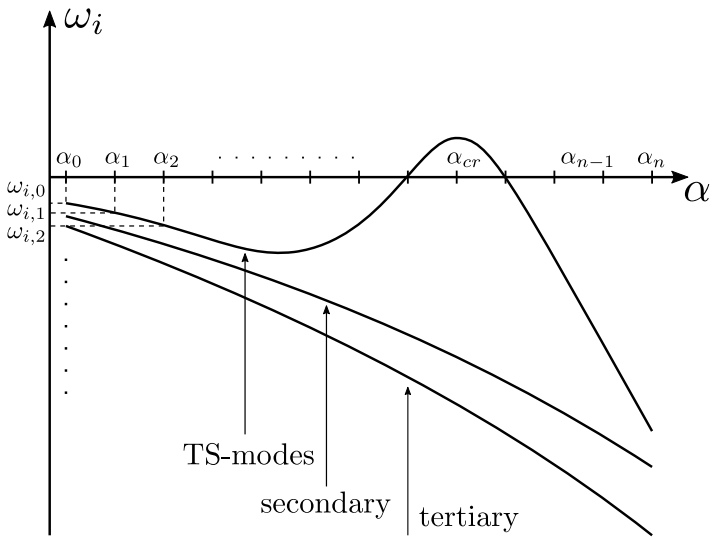

Figure 2.2: Visualization of a typical set of solution curves in a temporal stability problem for a given Reynolds number. Only the TS mode curve yields unstable modes in the vicinity of α_{cr}, which therefore is the curve of interest. The higher mode curves are not visualized.

Analogously, the spatial stability problem is examined when assuming

$$\{\beta, \omega\} \in \mathbb{R}, \qquad \alpha \in \mathbb{C}, \tag{2.66}$$

which again substituted into (2.42) yields

$$v(x, y, z, t) = \tilde{v}(y)\, e^{i(\alpha_r x + \beta z - \omega t)}\, e^{-\alpha_i x}. \tag{2.67}$$

While admittedly the sign in front of α contradicts the previous justifications, it is held consistent with common literature (see e.g. Schmid et al. (2002)). Thus, in opposition to the temporal framework, a positive α_i now leads to decay in positive streamwise direction whereas a negative α_i induces growth. Consequently, the dispersion relation (2.60) in analogy to the temporal framework is rewritten as

$$\mathcal{D}(\alpha)_{\beta,\omega,Re} = 0. \tag{2.68}$$

The general procedure of computing solutions for the eigenvalue α is identical to the aforementioned described steps for the temporal framework and therefore requires no further explanation. With this, the two relevant frameworks have been established for LST.

2.4.4 Squire's transformation

As was elaborated before, considering the spanwise direction in a stability problem adds an additional dimension to the parameter space and therefore greatly increases computational costs. In the case of temporal stability, for example, three parameter arrays $\{\alpha, \beta, Re\}$ need to be iterated through in order to capture the global stability characteristics. It was Squire (1933) who realized that in fact the 3D problem in the temporal case is dispensable and is accessible through the 2D problem via a remarkable set of transformations, henceforth called by their name in literature, i.e. Squire's transformation. The transformation becomes most apparent upon comparing the 2D and 3D OSE

$$\left[iRe_{2D}(\alpha_{2D}U_0(y) - \omega_{2D})(\mathrm{D}^2 - \alpha_{2D}^2) - iRe\alpha_{2D}U_0''(y) - (\mathrm{D}^2 - \alpha_{2D}^2)^2\right]\tilde{v}(y) = 0, \tag{2.69a}$$

$$\left[iRe_{3D}(\alpha_{3D}U_0(y) - \omega_{3D})(\mathrm{D}^2 - k^2) - iRe_{3D}\alpha_{3D}U_0''(y) - (\mathrm{D}^2 - k^2)^2\right]\tilde{v}(y) = 0, \tag{2.69b}$$

where the subscripts determine in which dimension the parameter is defined. Notice that $k = \alpha$ as $\beta = 0$. Comparing all parameter factors in (2.69) reveals that indeed (2.69a) and (2.69b) are equal if the invariance conditions

$$\alpha_{2D}^2 = \alpha_{3D}^2 + \beta^2, \tag{2.70a}$$

$$Re_{2D}\alpha_{2D} = Re_{3D}\alpha_{3D}, \tag{2.70b}$$

$$Re_{2D}\omega_{2D} = Re_{3D}\omega_{3D}, \tag{2.70c}$$

are satisfied. Equations (2.70a) – (2.70c) solved for the 3D parameters give

$$\alpha_{3D} = \sqrt{\alpha_{2D}^2 - \beta^2}, \tag{2.71a}$$

$$\omega_{3D,r} = \omega_{2D,r}\frac{\sqrt{\alpha_{2D}^2 - \beta^2}}{\alpha_{2D}}, \tag{2.71b}$$

$$\omega_{3D,i} = \omega_{2D,i}\frac{\sqrt{\alpha_{2D}^2 - \beta^2}}{\alpha_{2D}}, \tag{2.71c}$$

$$Re_{3D} = Re_{2D}\frac{\alpha_{2D}}{\sqrt{\alpha_{2D}^2 - \beta^2}}, \tag{2.71d}$$

where the temporal eigenvalue ω is readily split into real and imaginary part. Hence, one may take the set of 2D wave parameters and the 2D Reynolds number, transform them according to (2.71) by deciding on a non-zero β and obtains the corresponding set of 3D parameters which readily satisfy the dispersion relation (2.65) that would arise for the 3D case. Of particular interest is (2.71d). Due to the denominator on the r.h.s. always being lower or as large as unity, Squire's theorem may be deduced, which states that regardless of the temporal wave parameters

$$Re_{2D} \leq Re_{3D}. \tag{2.72}$$

More importantly, this result states that in case a critical Reynolds numbers exists in 2D, it is always lower than the corresponding 3D critical Reynolds number, i.e.

$$Re_{2D,cr} \leq Re_{3D,cr}. \tag{2.73}$$

This generally serves as justification to omit the analysis of the 3D stability problem in search for the most critical Reynolds number, at which onset of transition is predicted in the temporal

framework. Now, things are different in the spatial case. It can be shown that the Squire transformations cannot be derived for the spatial stability problem. The corresponding proof will be delivered in chapter 5. Moreover, on the basis of symmetry theory an extension of the Squire's transformation will be presented therein, in order to match the demands of the spatial stability framework.
At this point, it shall not remain unmentioned that due to shortcomings of LST regarding the correct prediction of laminar-turbulent transition in wall-bounded shear flows (Schmid, 2007), it was discovered that transient growth mechanisms induced by the non-orthogonality of the eigenvector basis play an important role in the transition process, which is extensively discussed by Reddy et al. (1993). In certain cases, the superposition of $n > 1$ eigenvectors may in turn lead to a transient growth of the maximum amplification energy $G(t)$ even if every single eigenvector decays in the framework of modal stability theory. Non-linear extensions to nonmodal stability theory are discussed extensively by Kerswell (2018), where the interested reader is referred to.
With this, the theoretical groundwork is laid for the subsequent chapters. In chapter 3, the LSA of the ASBL is presented, mostly based on the methods presented in this chapter. The superiority of analytical solutions over numerical solutions of the OSE (2.43) is demonstrated by means of asymptotic expansions of the underlying EVP. Moreover, the existence of continuous modes in both the temporal and spatial framework are discussed for the ASBL. Chapter 4 revolves around PCF and its behavior in the presence of transpiration. A thorough temporal and spatial stability analysis is presented, showing how transpiration in fact destabilizes the flow when large enough. The extension of Squire's transformation is applied on classical PCF in chapter 5, where novel modes with oblique growth are derived and numerically verified. In summary, the previously presented classical methods of LST are revisited and extended significantly. It will be shown that linear modal stability theory has not been exhausted yet and offers new theoretical grounds, which may and should be applied to other flows in order to enhance the understanding of linear stability in general.

3 Revisiting linear stability of the asymptotic suction boundary

Essential parts of the following chapter are heavily based on the peer-reviewed publication Yalcin et al. (2021), in particular the results presented in section 3.2.

It was Prandtl (1904) who first discussed the stabilizing effect of suction on flows around bodies. He reported a reduced pressure drag on a body, which was equipped with suction slits. The consequential question is how any kind of throughflow, whether it is suction or injection, alters the stability of a plane wall-bounded shear flow. The delay of laminar-turbulent transition on airfoils has been known ever since early experiments and design studies by Richards and Burge (1943), who reported that by virtue of well-engineered suction slits a laminar flow is maintained on an airfoil all the way to the trailing edge while separation is suppressed simultaneously. Based on this, a thorough understanding of the linear stability of boundary layer (BL) suction should be aimed for. In the context of turbulent superstructures, it is also of particular interest in what sense the linear stability of suction boundary layers is connected to large-scale persisting structures in turbulent suction boundary layer flows.
Linear stability theory in fluid mechanics has celebrated many successes ever since it was formally established by Orr (1907) and Sommerfeld (1908). One flow of particular interest until today has been the BL flow establishing itself over a flat plate. The understanding of laminar to turbulent transition in a BL is of highest interest for technical applications, as in principal any surface exposed to a inflow witnesses the emergence of a BL on its surface. A turbulent boundary layer (TBL) has larger streamwise velocity gradients at the wall than laminar BL. The wall shear stress is defined by

$$\tau_w \equiv \tau(y=0) = \mu \frac{\partial U(x,y)}{\partial y}\bigg|_{y=0}, \tag{3.1}$$

due to which TBL entail larger wall shear stress and, thus, energy loss due to friction. One of the mathematical challenges of analyzing BL in the framework of linear stability theory (LST) is BL growth, where, due to no-slip at the surface, the BL becomes thicker and the velocity field inside the BL is altered with increasing distance from the leading edge. If additionally a negative pressure gradient is present, i.e. $\mathrm{d}p/\mathrm{d}x < 0$, the flow may even experience separation from the surface, which especially in technical applications is highly unfavorable due to the kinetic energy loss via dissipation as well as the ensuing transient instabilities a flight vehicle, for instance, experiences.

Boundary layer theory and the Blasius boundary layer

One principal challenge of LST for boundary layers lies in the aforementioned growth of the boundary layer thickness $\delta(x)$ as well as the change of the two-dimensional (2D) velocity profile $\{U(x,y), V(x,y)\}$ in streamwise and wall-normal direction. In the case of uniform inflow U_∞, Blasius (1907) found self-similarity solutions for the velocity profile as well as the displacement thickness $\delta_1(x)$. The displacement thickness describes the distance from the wall, at which a uniform velocity profile U_∞ entails the same mass flow as the original BL flow, i.e. it quantifies the velocity defect due to the presence of the BL. It is therefore defined by

$$\delta_1(x) = \int_0^\infty \left(1 - \frac{U(x,y)}{U_\infty}\right) \mathrm{d}y. \tag{3.2}$$

Blasius now realized that Prandtl's dimensional 2D BL equations

$$U\frac{\partial U}{\partial x} + V\frac{\partial U}{\partial y} = \nu\frac{\partial^2 U}{\partial y^2}, \tag{3.3a}$$

$$\frac{\partial U}{\partial x} + \frac{\partial V}{\partial y} = 0, \tag{3.3b}$$

may be reduced to the self-similar Blasius equation

$$2f'''(\eta) + f(\eta)f''(\eta) = 0, \tag{3.4}$$

where

$$\eta = y\sqrt{\frac{U_\infty}{\nu x}}, \tag{3.5}$$

and $f(\eta)$ is defined so that the stream function $\psi(x,y)$ follows as

$$\psi = \sqrt{\nu x U_\infty} f(\eta), \tag{3.6a}$$

$$U(x,y) = \frac{\partial \psi}{\partial y} = U_\infty f', \tag{3.6b}$$

$$V(x,y) = -\frac{\partial \psi}{\partial x} = \frac{1}{2}\sqrt{\frac{\nu U_\infty}{x}}\left(\eta f' - f\right), \tag{3.6c}$$

where the definition of the stream function ψ satisfies the continuity equation (2.12) identically. These results are essential to understand the challenges the Blasius boundary layer (BBL) poses to LST. As the base velocity in streamwise direction (3.6b) is not given explicitly but rather in terms of the solution of the Blasius equation (3.4), which may only be solved numerically, the Orr–Sommerfeld equation (OSE) (2.43), as a result, must be solved numerically. As is discussed by Grosch and Salwen (1978) in the context continuous spectra, analytical access to the OSE for a BBL is possible via asymptotic expansion of the OSE (2.43) for $y \to \infty$. In this case $\lim_{y\to\infty} U \to U_\infty$ applies, which used in the expanded OSE yields the asymptotic solution

$$\tilde{v}(y) = C_1 e^{\sigma y} + C_2 e^{-\sigma y} + C_3 e^{\alpha y} + C_4 e^{-\alpha y}, \tag{3.7}$$

with

$$\sigma = \sqrt{\alpha^2 + iRe(\alpha - \omega)}. \tag{3.8}$$

The linear stability of the BBL has been discussed extensively, see e.g. Mack (1984) for a thorough overview regarding LST for boundary layers or Bertolotti et al. (1992) for a discussion of linear and non-linear stability in the context of the BBL.

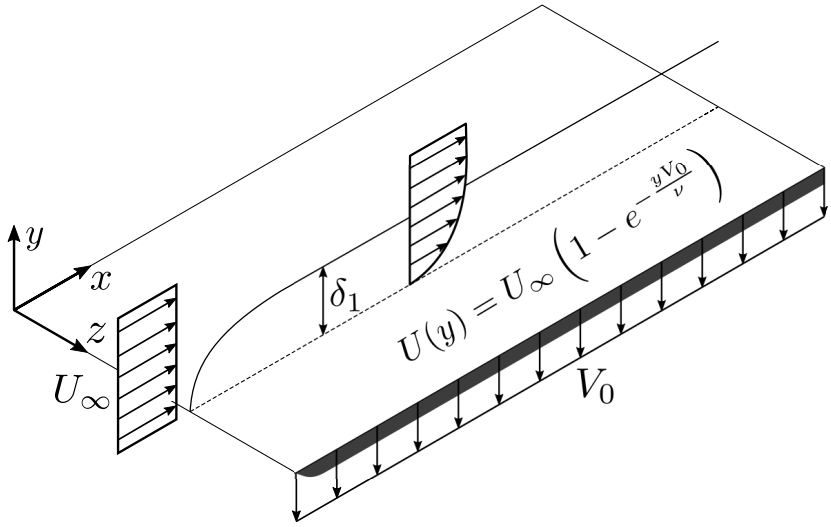

Figure 3.1: Schematic depiction of the three-dimensional (3D) asymptotic suction boundary layer (adapted from Yalcin et al. (2021))

3.1 Linear stability equations for the asymptotic suction boundary layer

The focus of the present chapter lies on the analytical LST of the asymptotic suction boundary layer (ASBL), which has been neglected in common literature to date. While common flat-plate boundary layers were thoroughly discussed after the establishment of Prandtl's BL theory, the presence of suction initially was not discussed. It was Thwaites (1946) who first showed that the presence of suction at the wall does not alter the structure of the Blasius solution principally when considering the BL very close to the leading edge. Already a decade before, Griffith and Meredith (1936) showed that for distances far enough away from the leading edge, the BL thickness asymptotically becomes constant, while the velocity profile U_i simultaneously becomes solely dependent on the wall-normal coordinate y. When assuming $U_i = U_i(y)$ and $V = -V_0$, the Prandtl BL equations reduce to

$$-V_0 \frac{\mathrm{d}U}{\mathrm{d}y} = \nu \frac{\mathrm{d}^2 U}{\mathrm{d}y^2}, \tag{3.9}$$

when the continuity equation is trivially satisfied.
The boundary conditions for (3.9) are

$$U(y = 0) = 0, \qquad U(y \to \infty) \to U_\infty. \tag{3.10}$$

Solving (3.9) with (3.10) gives the velocity profile for the ASBL

$$(U, V, W)^T = \left(U_\infty \left(1 - e^{-\frac{V_0}{\nu} y}\right), -V_0, 0\right)^T. \tag{3.11}$$

The ensuing velocity profile (3.11) is depicted in figure 3.1. The displacement thickness $\delta_1(x)$ (2.60) correspondingly asymptotically grows towards a constant value given by

$$\delta_1 = \int_0^\infty \left(1 - \frac{U(y)}{U_\infty}\right) \mathrm{d}y = \frac{\nu}{V_0}. \tag{3.12}$$

Thus, the displacement thickness readily provides a length scale for non-dimensionalization, which transforms $U(y)$ in (3.11) to

$$U(y) = U_\infty \left(1 - e^{-\frac{y}{\delta_1}}\right). \tag{3.13}$$

In order to non-dimensionalize the flow problem, the characteristic scales (2.29) are readily chosen as

$$L_c = \delta_1, \tag{3.14a}$$
$$U_c = U_\infty, \tag{3.14b}$$

which employed into (3.11) yields the non-dimensional profile

$$\left(U^+, V^+, W^+\right)^T (y^+) = \frac{(U,V,W)^T}{U_\infty}\left(\frac{y}{\delta_1}\right) = \left(U_\infty\left(1 - e^{-y^+}\right), -\frac{1}{Re}, 0\right)^T, \tag{3.15}$$

where the pluses as mentioned previously will be omitted hereafter for the sake of brevity. The definition of the Reynolds number (2.31) therefore gives the unique expression

$$Re = \frac{U_\infty \delta_1}{\nu} = \frac{U_\infty}{V_0}. \tag{3.16}$$

Hence, the Reynolds number for the ASBL is defined purely by the two velocity quantities in the flow problem. A high free-stream velocity to suction velocity ratio would yield the inertial forces superior whereas a relatively large suction velocity would imply shift towards dominating friction forces.
The base state (3.11) is two-dimensional in contrast to the profile assumed in section 2.4, which featured $V = 0$. As such, the OSE (2.43) is slightly modified by an additional term induced by the constant wall-normal suction velocity V_0. Taking this into account, (2.43) turns into

$$L_{mOS}(\tilde{v}(y)) \equiv \left[(iRe(\alpha U(y) - \omega) - \mathrm{D})\left(\mathrm{D}^2 - k^2\right) - iRe\alpha U''(y) - \left(\mathrm{D}^2 - k^2\right)^2\right]\tilde{v}(y) = 0, \tag{3.17}$$

where L_{mOS} denotes the modified Orr–Sommerfeld (OS) operator and (3.17) is hereafter referred to as modified Orr–Sommerfeld equation (mOSE). Correspondingly, the Squire equation (SE) (2.53) is modified to

$$L_{mSE}(\tilde{\eta}(y)) \equiv \left[(iRe(\alpha U(y) - \omega) - \mathrm{D}) - \left(\mathrm{D}^2 - k^2\right)\right]\tilde{\eta}(y) = -iRe\beta U'(y)\tilde{v}(y), \tag{3.18}$$

where analogously L_{mSE} denotes the modified Squire operator and (3.18) from now on is called modified Squire equation (mSE).
For the linearized Navier–Stokes equations (LNSE), novel ansatz functions in addition to (2.54) may be obtained via Lie symmetry analysis, as was elaborated by Nold and Oberlack (2013) and Nold et al. (2015) for plane canonical shear flows. For the inviscid LNSE (2.36) modified by the aforementioned suction term $V = -V_0$, an analysis was performed for the ASBL and details are provided in section 3.2.4.
The analytical solution for the inviscid ASBL was derived in Chiarulli and Freeman (1948), who demonstrated that the presence of constant suction modifies the OSE in such way that it can be transformed to the ordinary hypergeometric differential equation solved by Gaussian hypergeometric functions. This result was later corrected by Hughes and Reid (1965), who

despite the existence of analytical solutions preferred numerical studies of the inviscid equation with asymptotic methods, which yielded a critical Reynolds number of $Re_{cr} \approx 47000$. The solution to the viscous formulation was provided by Baldwin (1970) in terms of ${}_2F_3$ generalized hypergeometric functions. Analogous to the inviscid case, the study of stability in the viscous case was conducted numerically by Hocking (1975) via transformation of the underlying equations to a non-linear Schrödinger equation, which in turn yielded $Re_{cr} = 54370$. A more precise transition Reynolds number could be obtained by employing Chebyshev collocation methods popularized incidentally by Orszag (1971) in the context of hydrodynamic stability analysis. The first to employ these methods for the ASBL were Fransson and Alfredsson (2003), obtaining a more refined critical Reynolds number reading $Re_{cr} = 54382$.
As will be demonstrated hereafter, the analytical solution of the mOSE (3.17) for the ASBL is superior to numerical methods both in the accuracy of the computed critical Reynolds number as well as with regard to physical information included in the analytical eigenvalue problem (EVP) (2.60) later derived for the ASBL. As Baldwin (1970) showed for the stability problem of the viscous formulation of the ASBL, the mOSE (3.17) is in fact a generalized hypergeometric differential equation, which according to Olver et al. (2010) is defined by

$$(\vartheta(\vartheta + b_1 - 1)\cdots(\vartheta + b_q - 1) - y(\vartheta + a_1)\cdots(\vartheta + a_p))\, w(y) = 0, \tag{3.19}$$

where a_i and b_i denote parameters and

$$\vartheta = y\frac{\mathrm{d}}{\mathrm{d}y}. \tag{3.20}$$

Equation (3.19) is in turn solved by the generalized hypergeometric function $w(y) = {}_pF_q(\boldsymbol{a}, \boldsymbol{b}; y)$, where

$${}_pF_q\left(\begin{matrix} a_1, \ldots, a_p \\ b_1, \ldots, b_q \end{matrix}; y\right) = \sum_{k=0}^{\infty} \frac{(a_1)_k \cdots (a_p)_k}{(b_1)_k \cdots (b_q)_k} \frac{y^k}{k!}. \tag{3.21}$$

It can now be shown that the mOSE (3.17) concretely represents a ${}_2F_3$ generalized hypergeometric differential equation with $p = 2$ and $q = 3$ as given in (3.21) solved by the corresponding ${}_2F_3$ generalized hypergeometric function

$${}_2F_3\left(\begin{matrix} a_1, a_2 \\ b_1, b_2, b_3 \end{matrix}; y\right) = \sum_{k=0}^{\infty} \frac{(a_1)_k (a_2)_k}{(b_1)_k (b_2)_k (b_3)_k} \frac{y^k}{k!}, \tag{3.22}$$

where the Pochhammer symbol $(a)_n$ is defined as

$$(a)_0 = 1, \tag{3.23a}$$
$$(a)_k = a(a+1)(a+2)\cdots(a+k-1), \tag{3.23b}$$
$$(a)_k = \Gamma(a+k)/\Gamma(a), \tag{3.23c}$$

in which $\Gamma(a)$ denotes the Gamma function with the argument a and $k \notin \mathbb{Z}^-$. Solving the mOSE (3.17) consequently yields the solution space

$$\begin{aligned} \tilde{v}(y) = {} & C_1\, e^{ky}\, {}_2F_3\left(\begin{matrix} \boldsymbol{a_1} \\ \boldsymbol{b_1} \end{matrix}; -iRe\,\alpha\, e^{-y}\right) + C_2\, e^{-ky}\, {}_2F_3\left(\begin{matrix} \boldsymbol{a_2} \\ \boldsymbol{b_2} \end{matrix}; -iRe\,\alpha\, e^{-y}\right) \\ & + C_3\, e^{\frac{\sigma-1}{2}y}\, {}_2F_3\left(\begin{matrix} \boldsymbol{a_3} \\ \boldsymbol{b_3} \end{matrix}; -iRe\,\alpha\, e^{-y}\right) + C_4\, e^{-\frac{\sigma+1}{2}y}\, {}_2F_3\left(\begin{matrix} \boldsymbol{a_4} \\ \boldsymbol{b_4} \end{matrix}; -iRe\,\alpha\, e^{-y}\right), \end{aligned} \tag{3.24}$$

with

$$\boldsymbol{a_1} = \begin{pmatrix} -\tilde{k} - k \\ \tilde{k} - k \end{pmatrix}, \quad \boldsymbol{a_2} = \begin{pmatrix} \tilde{k} + k \\ -\tilde{k} + k \end{pmatrix}, \quad \boldsymbol{a_3} = \begin{pmatrix} \frac{1}{2} - \frac{\sigma}{2} + \tilde{k} \\ \frac{1}{2} - \frac{\sigma}{2} - \tilde{k} \end{pmatrix}, \quad \boldsymbol{a_4} = \begin{pmatrix} \frac{1}{2} + \frac{\sigma}{2} + \tilde{k} \\ \frac{1}{2} + \frac{\sigma}{2} - \tilde{k} \end{pmatrix}, \tag{3.25a}$$

$$\boldsymbol{b_1} = \begin{pmatrix} 1 - 2k \\ \frac{1}{2} + \frac{\sigma}{2} - k \\ \frac{1}{2} - \frac{\sigma}{2} - k \end{pmatrix}, \quad \boldsymbol{b_2} = \begin{pmatrix} 1 + 2k \\ \frac{1}{2} - \frac{\sigma}{2} + k \\ \frac{1}{2} + \frac{\sigma}{2} + k \end{pmatrix}, \quad \boldsymbol{b_3} = \begin{pmatrix} 1 - \sigma \\ \frac{3}{2} - \frac{\sigma}{2} + k \\ \frac{3}{2} - \frac{\sigma}{2} - k \end{pmatrix}, \quad \boldsymbol{b_4} = \begin{pmatrix} 1 + \sigma \\ \frac{3}{2} + \frac{\sigma}{2} + k \\ \frac{3}{2} + \frac{\sigma}{2} - k \end{pmatrix}, \tag{3.25b}$$

where

$$\tilde{k} = \sqrt{k^2 + 1}, \tag{3.26a}$$

$$\sigma = \sigma_{ASBL} = \sqrt{4k^2 + 1 + 4iRe(\alpha - \omega)}, \tag{3.26b}$$

$$\tag{3.26c}$$

in which σ_{ASBL} indicates a clear distinction when compared to the corresponding parameter occurring for the BBL as given in (3.8) and hereafter is called viscous parameter. This naming stems from the fact that the sub-solutions in (3.24) are classically called viscous modes, whereas the modes accompanied with the exponential functions $e^{\pm ky}$ are called inviscid solutions in the BBL, as is discussed by Grosch and Salwen (1978). As is further apparent from (3.24) and (3.25), the solutions $\tilde{v}_1(y)$ and $\tilde{v}_2(y)$ share a reflection symmetry in k, whereas similarly $\tilde{v}_3(y)$ and $\tilde{v}_4(y)$ have a reflection symmetry in σ. The solution to the mOSE (3.24) is complemented by the boundary condition (BC) set

$$\tilde{v}(y = 0) = 0, \qquad \mathrm{D}\tilde{v}(y)|_{y=0} = 0, \tag{3.27a}$$

$$\tilde{v}(y \to \infty) = 0, \qquad \mathrm{D}\tilde{v}(y)|_{y\to\infty} = 0. \tag{3.27b}$$

The BC at infinity (3.27b) concretely read

$$\tilde{v}(y \to \infty) = \lim_{y\to\infty} \left[C_1\, e^{ky} + C_2\, e^{-ky} + C_3\, e^{\frac{\sigma-1}{2}y} + C_4\, e^{-\frac{\sigma+1}{2}y} \right] = 0, \tag{3.28a}$$

$$\mathrm{D}\tilde{v}(y)|_{y\to\infty} = \lim_{y\to\infty} \left[C_1\, k\, e^{ky} - C_2\, k\, e^{-ky} + C_3 \left(\frac{\sigma - 1}{2} \right) e^{\frac{\sigma-1}{2}y} - C_4 \left(\frac{\sigma + 1}{2} \right) e^{-\frac{\sigma+1}{2}y} \right] = 0, \tag{3.28b}$$

where the rather simple structure is due to the fact that in general

$$\lim_{y\to 0} {}_pF_q \left(\begin{matrix} a_1, \ldots, a_p \\ b_1, \ldots, b_q \end{matrix}; y \right) \to 1, \tag{3.29}$$

applies for generalized hypergeometric functions. Moreover, the derivative of a generalized hypergeometric function, with an argument $z(y)$ instead of y, w.r.t y is given as

$$\frac{\mathrm{d}}{\mathrm{d}y} {}_pF_q \left(\begin{matrix} a_1, \ldots, a_p \\ b_1, \ldots, b_q \end{matrix}; z(y) \right) = \frac{\overline{a}}{\overline{b}} z'(y)\, {}_pF_q \left(\begin{matrix} a_1 + 1, \ldots, a_p + 1 \\ b_1 + 1, \ldots, b_q + 1 \end{matrix}; z(y) \right), \tag{3.30}$$

where in turn

$$\overline{a} = \prod_{i=1}^{p} a_i, \tag{3.31a}$$

$$\overline{b} = \prod_{i=1}^{q} b_i, \tag{3.31b}$$

gives the product over all elements of the parameter vectors $\boldsymbol{a}$ and $\boldsymbol{b}$, respectively.
Since by definition $k > 0$, the solution $v_1(y) = C_1\, e^{ky}$ diverges for $y \to \infty$, while $v_2(y) = C_2\, e^{-ky}$ converges. Therefore, $C_1 = 0$. The handling of the two remaining solutions depend solely on the real part of $\sigma \in \mathbb{C}$. In principle, $\sigma = \pm(\sigma_r + i\sigma_i)$ as σ is the root of a complex number (see 3.26b). Due to the reflection symmetry of $\tilde{v}_3(y)$ and $\tilde{v}_4(y)$ in σ, it is sufficient to focus on $\sigma = \sigma_r + i\sigma_i$ solely. For any value of k and Re, the real part σ_r is always greater than zero, for which $\tilde{v}_4(y) = C_4\, e^{-\frac{\sigma+1}{2}\, y}$ converges.
It can be shown that only the case $\sigma_r > 1$ is relevant, whereupon $C_3 = 0$. The remaining BC (3.27a) at the wall then reduce to

$$\tilde{v}(y=0) = C_2 \underbrace{{}_2F_3\left(\begin{matrix}\boldsymbol{a_2}\\ \boldsymbol{b_2}\end{matrix}; -iRe\,\alpha\right)}_{A_1(\alpha,\beta,\omega,Re)} + C_4 \underbrace{{}_2F_3\left(\begin{matrix}\boldsymbol{a_4}\\ \boldsymbol{b_4}\end{matrix}; -iRe\,\alpha\right)}_{A_2(\alpha,\beta,\omega,Re)} = 0, \tag{3.32a}$$

$$\begin{aligned}\mathrm{D}\tilde{v}(y)|_{y=0} = C_2 &\underbrace{\left[\frac{\overline{a}_2}{\overline{b}_2}\, {}_2F_3\left(\begin{matrix}\boldsymbol{a_2+1}\\ \boldsymbol{b_2+1}\end{matrix}; -iRe\,\alpha\right) iRe\,\alpha - k\, {}_2F_3\left(\begin{matrix}\boldsymbol{a_2}\\ \boldsymbol{b_2}\end{matrix}; -iRe\,\alpha\right)\right]}_{A_3(\alpha,\beta,\omega,Re)} \\ + C_4 &\underbrace{\left[\frac{\overline{a}_4}{\overline{b}_4}\, {}_2F_3\left(\begin{matrix}\boldsymbol{a_4+1}\\ \boldsymbol{b_4+1}\end{matrix}; -iRe\,\alpha\right) iRe\,\alpha - \left(\frac{\sigma+1}{2}\right) {}_2F_3\left(\begin{matrix}\boldsymbol{a_4}\\ \boldsymbol{b_4}\end{matrix}; -iRe\,\alpha\right)\right]}_{A_4(\alpha,\beta,\omega,Re)} = 0.\end{aligned} \tag{3.32b}$$

It is now, in principal, possible to solve for one of the constants and substitute them together with $C_1 = C_3 = 0$ into the solution (3.24). Thus, solving for C_2 in (3.32a) gives

$$C_2 = -C_4 \frac{{}_2F_3\left(\begin{matrix}\boldsymbol{a_4}\\ \boldsymbol{b_4}\end{matrix}; z(0)\right)}{{}_2F_3\left(\begin{matrix}\boldsymbol{a_2}\\ \boldsymbol{b_2}\end{matrix}; z(0)\right)}\, {}_2F_3\left(\begin{matrix}\boldsymbol{a_2}\\ \boldsymbol{b_2}\end{matrix}; z(y)\right), \tag{3.33}$$

with $z(y) = -iRe\alpha e^{-y}$, which substituted into (3.24) gives the eigenfunction

$$\tilde{v}(y) = C_4 \left[e^{-\frac{1}{2}(\sigma+1)y}\, {}_2F_3\left(\begin{matrix}\boldsymbol{a_4}\\ \boldsymbol{b_4}\end{matrix}; z(y)\right) - e^{-ky} \frac{{}_2F_3\left(\begin{matrix}\boldsymbol{a_4}\\ \boldsymbol{b_4}\end{matrix}; z(0)\right)}{{}_2F_3\left(\begin{matrix}\boldsymbol{a_2}\\ \boldsymbol{b_2}\end{matrix}; z(0)\right)}\, {}_2F_3\left(\begin{matrix}\boldsymbol{a_2}\\ \boldsymbol{b_2}\end{matrix}; z(y)\right) \right], \tag{3.34}$$

where the arbitrary constant C_4 accounts for the fact that (3.35) is a homogeneous linearly independent equation system. Moreover, physically C_4 implies that any magnitude of the eigenfunction (3.34) solves the mOSE (3.17).
The two conditions in (3.32) further establish a matrix equation of the type

$$\begin{pmatrix} A_1(\alpha,\beta,\omega,Re) & A_2(\alpha,\beta,\omega,Re) \\ A_3(\alpha,\beta,\omega,Re) & A_4(\alpha,\beta,\omega,Re) \end{pmatrix} \begin{pmatrix} C_2 \\ C_4 \end{pmatrix} = \begin{pmatrix} 0 \\ 0 \end{pmatrix}, \tag{3.35}$$

for which non-trivial solutions for C_2 and C_4 only exist for

$$\mathcal{D}(\alpha,\beta,Re,\omega) = \det\left(\boldsymbol{A}(\alpha,\beta,\omega,Re)\right) = 0, \tag{3.36}$$

which establishes the dispersion relation already presented in (2.60). In fact, the determinant in (3.36) defines an algebraic EVP of the form

$$\begin{aligned}
&\mathcal{D}(\alpha,\beta,Re,\omega)\\
&= {}_2F_3\left(\begin{matrix}\boldsymbol{a_2}\\ \boldsymbol{b_2}\end{matrix};-iRe\,\alpha\right)\left[iRe\,\alpha\,\frac{\overline{a}_4}{\overline{b}_4}\,{}_2F_3\left(\begin{matrix}\boldsymbol{a_4+1}\\ \boldsymbol{b_4+1}\end{matrix};-iRe\,\alpha\right)-\left(\frac{\sigma+1}{2}\right){}_2F_3\left(\begin{matrix}\boldsymbol{a_4}\\ \boldsymbol{b_4}\end{matrix};-iRe\,\alpha\right)\right]\\
&- {}_2F_3\left(\begin{matrix}\boldsymbol{a_4}\\ \boldsymbol{b_4}\end{matrix};-iRe\,\alpha\right)\left[iRe\,\alpha\,\frac{\overline{a}_2}{\overline{b}_2}\,{}_2F_3\left(\begin{matrix}\boldsymbol{a_2+1}\\ \boldsymbol{b_2+1}\end{matrix};-iRe\,\alpha\right)-k\,{}_2F_3\left(\begin{matrix}\boldsymbol{a_2}\\ \boldsymbol{b_2}\end{matrix};-iRe\,\alpha\right)\right]=0,
\end{aligned}\tag{3.37}$$

in which the eigenvalue is yet to be decided and decides whether the temporal or spatial EVP as discussed in section 2.4.3 is examined.

The mSE (3.18) is in fact a modified Bessel's equation of the form

$$y^2\frac{\mathrm{d}^2w(y)}{\mathrm{d}y^2}+y\frac{\mathrm{d}w}{\mathrm{d}y}-(y^2+\nu^2)w(y)=0,\tag{3.38}$$

where ν denotes a parameter of the second order ordinary differential equation (ODE) and $w(y)$ is the sought solution. Equation (3.38) is solved by functions of the type

$$I_\nu(y)=(\tfrac{1}{2}y)^\nu\sum_{k=0}^{\infty}\frac{(\frac{1}{4}y^2)^k}{k!\Gamma\left(\nu+k+1\right)},\tag{3.39a}$$

$$K_\nu(y)=\frac{\pi}{2}\frac{I_{-\nu}(y)-I_\nu(y)}{\sin\nu\pi},\tag{3.39b}$$

where $I_\nu(y)$ and $K_\nu(y)$ are called modified Bessel functions of first and second kind. With this, the inhomogeneous mSE (3.18) yields the solutions

$$\begin{aligned}
\tilde{\eta}(y)=&\,2iRe\,\beta\,e^{-\frac{y}{2}}\left[-I_{-\sigma}\left((i-1)\sqrt{2Re\,\alpha}\,e^{-\frac{y}{2}}\right)\int e^{-\frac{y}{2}}K_\sigma\left((i-1)\sqrt{2Re\,\alpha}\,e^{-\frac{y}{2}}\right)\tilde{v}(y)\,\mathrm{d}y\right.\\
&\left.+\;K_\sigma\left((i-1)\sqrt{2Re\,\alpha}\,e^{-\frac{y}{2}}\right)\int e^{-\frac{y}{2}}I_{-\sigma}\left((i-1)\sqrt{2Re\,\alpha}\,e^{-\frac{y}{2}}\right)\tilde{v}(y)\,\mathrm{d}y\right]\\
&+C_5\,e^{-\frac{y}{2}}\,I_{-\sigma}\left((i-1)\sqrt{2Re\,\alpha}\,e^{-\frac{y}{2}}\right)+C_6\,e^{-\frac{y}{2}}\,K_\sigma\left((i-1)\sqrt{2Re\,\alpha}\,e^{-\frac{y}{2}}\right),
\end{aligned}\tag{3.40}$$

with the BC at wall and at infinity

$$\tilde{\eta}(y=0)=0,\qquad \eta(y\to\infty)=0.\tag{3.41}$$

The results of the mOSE and mSE (3.24) and (3.40) with eigenvalues satisfying the EVP (3.36) now make it possible to derive the entire 3D perturbation field by virtue of the continuity equation and the definition of the wall-normal vorticity

$$i\alpha\tilde{u}(y)+\frac{\mathrm{d}\tilde{v}(y)}{\mathrm{d}y}+i\beta\tilde{w}(y)=0,\tag{3.42a}$$

$$\tilde{\eta}(y)=i\beta\tilde{u}(y)-i\alpha\tilde{w}(y).\tag{3.42b}$$

With this, the governing equations for a linear stability analysis (LSA) of the ASBL is laid, which is categorized into the temporal stability problem, discussed in the subsequent section, and the spatial stability problem, which follows afterwards in section 3.3.

3.2 Temporal stability analysis of the asymptotic suction boundary layer

For reasons unknown to the author, the thorough stability analysis of the ASBL has been neglected in literature. Thus, the results in Yalcin et al. (2021) fill a void in this regard and bring forth unique insights into the temporal algebraic EVP (3.36) via asymptotic analysis of the respective parameters. Furthermore, the existence of continuous modes as introduced by Grosch and Salwen (1978) is demonstrated and lastly a classical stability analysis with focus on the Tollmien–Schlichting (TS) modes is presented. This entire section is reproduced from Yalcin et al. (2021), with the permission of AIP Publishing.

3.2.1 Continuous temporal linear modes

It was shown by Grosch and Salwen (1978) that the classical linear modes acquired through the homogeneous BC set (3.27a) and (3.27b) are not necessarily the only physically plausible linear modes. Therein it was questioned, if the BC at infinity, demanding vanishing perturbation velocities therein, are adequate. A counter-proposal instead were so called relaxed BC of the type

$$\tilde{v}(y), \mathrm{D}\tilde{v}(y) \quad \text{bounded for} \quad y \to \infty, \tag{3.43}$$

which effectively relaxes the rather restrictive condition on the exponents in (3.24) such that the exponent a of an exponential function e^{ay} needs not to be strictly zero, but rather can take values in the number set

$$a \in \mathbb{Z}_0^- \quad \text{for any} \quad y \in \mathbb{R}_0^+. \tag{3.44}$$

Hence, the entire solution $\tilde{v}(y)$ stay bounded if the exponential functions in each sub-solution $\tilde{v}_i(y)$ stays bounded. For the ASBL, regardless of the relaxed BC (3.43)

$$C_1 = 0, \tag{3.45}$$

must apply, since $\tilde{v}_1(y) \to \infty$ as $y \to \infty$. It was shown previously that the solutions $\tilde{v}_2(y)$ and $\tilde{v}_4(y)$ are always bounded and, in fact, disappear at infinity due to their real exponents always being negative. This leaves the novel relaxed BC

$$\sigma_r - 1 = 0 \quad \text{as} \quad y \to \infty, \tag{3.46}$$

induced by the demanded boundedness of solution $\tilde{v}_3(y)$. As was elaborated in 2.4.4, the 3D temporal problem is superfluous in that it may be obtained readily via the LST of the 2D temporal problem through Squire's transformation (5.9). Thus, hereafter the 2D temporal stability problem is assumed with $\beta = 0$. Subsequently, the real and imaginary parts of the viscous parameter σ will be required for the derivation of the continuous modes as well as for assessing the eigenfunctions in section 3.2.3. Assuming

$$\sigma = \sqrt{a + bi} = \pm(\sigma_r + \sigma_i), \tag{3.47}$$

one obtains for σ_r and σ_i

$$\sigma_r = \frac{1}{\sqrt{2}}\sqrt{\sqrt{(4\,\alpha^2 + 4\,Re\,\omega_i + 1)^2 + 16\,Re^2(\alpha - \omega_r)^2} + (4\,\alpha^2 + 4\,Re\,\omega_i + 1)}, \tag{3.48a}$$

$$\sigma_i = \mathrm{sgn}(\Delta)\,\frac{1}{\sqrt{2}}\sqrt{\sqrt{(4\,\alpha^2 + 4\,Re\,\omega_i + 1)^2 + (4\,Re\,\alpha - 4\,Re\,\omega_r)^2} - (4\,\alpha^2 + 4\,Re\,\omega_i + 1)}, \tag{3.48b}$$

with $\Delta = \alpha - \omega_r$. Hence, the condition (3.46) is now given as

$$\frac{1}{\sqrt{2}}\sqrt{\sqrt{(4\,\alpha^2 + 4\,Re\,\omega_i + 1)^2 + 16\,Re^2(\alpha - \omega_r)^2} + (4\,\alpha^2 + 4\,Re\,\omega_i + 1)} = 1, \tag{3.49}$$

where the l.h.s. in (3.49) is the expanded real part of σ as defined in (3.26b). It is now possible to solve (3.49) for the designated growth rate $\omega_i = \omega_i(\omega_r, \alpha, Re)$, i.e.

$$\omega_i = -\left(\frac{\alpha^2}{Re} + Re(\alpha - \omega_r)^2\right), \tag{3.50}$$

due to which ω_i is parabolic w.r.t. its argument ω_r. Employing ω_i into the definition of the complex number

$$\omega = \omega_r + i\omega_i, \tag{3.51}$$

gives

$$\omega = \omega_r - i\left(\frac{\alpha^2}{Re} + Re(\alpha - \omega_r)^2\right). \tag{3.52}$$

As per (3.52), the ω_r-ω_i-spectrum is continuous. For a given streamwise wave number α and Reynolds number Re, the temporal growth rate ω_i is parabolic w.r.t. ω_r and always opened downwards.
An exemplary temporal continuous spectrum is given in figure 3.2 for $\alpha = 1$ and $Re = 500$. The spectrum is compared to the one obtained for the BBL in dashed lines, which is derived in Grosch and Salwen (1978). The parameters are identical in both cases. As can be deduced, both spectra are maximal at $\omega_r = 1$, where the imaginary part yields

$$\omega_i = -\alpha^2/Re. \tag{3.53}$$

Thus, for $Re \to \infty$ or $\alpha \to 0$ the temporal growth rate ω_i tends towards zero. Despite the damping character of these modes, they might nevertheless be very relevant to laminar-turbulence transition. The relaxed BC (3.43) implies that continuous modes do not decay in wall-normal direction but rather oscillate harmoniously into infinity with a specific wall-normal wavelength. In contrast, the classical linear modes computed from the EVP (3.36) decay naturally as per the BC at infinity (3.27b). And if the continuous modes persist long enough in time, i.e. ω_i in (3.53) tends towards zero, they may modulate the BL such that additional transition mechanisms are triggered. The phenomenon of disturbances induced by free-stream turbulence (FST) is well known to be a possible explanation for bypass transition at Reynolds numbers below the critical Reynolds number predicted by LST. An experimental notion of disturbances induced in a BL by FST was published by Kendall (1985). This phenomenon was further examined experimentally for suction boundary layers in detail by Yoshioka et al.

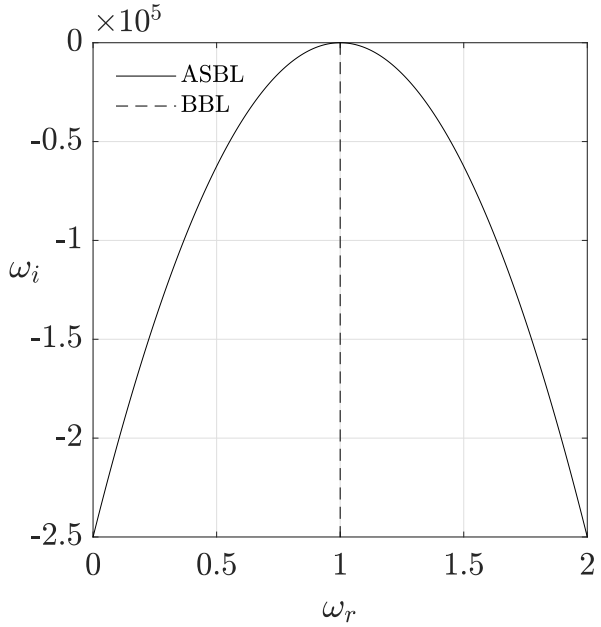

Figure 3.2: Temporal continuous spectrum for the ASBL (line) and the BBL (dashed line) with $\alpha = 1$ and $Re = 500$. For both spectra a maximum is located at $\omega_r = 1$ and $\omega_i = -\alpha^2/Re$. (adapted from Yalcin et al. (2021))

(2004). They observed a transition to turbulence at Reynolds numbers as low as $Re \approx 344$ at the presence of FST. Moreover, they confirmed a streaky structure of disturbances in streamwise direction. Transferred to modal disturbances, elongation of perturbations into the streamwise direction would in fact correspond to comparatively small streamwise wave numbers α, which in fact would coincide with (3.53), where small α induce temporal modes with minimal decay rates ω_i. At this point, this is not confirmed by experiments or simulations, but further investigations in this direction are certainly motivated by the present author. Furthermore, such persisting continuous modes with large wavelengths λ_x in streamwise direction might contribute to the introductory goals of understanding the formation of large-scale persisting superstructures.

3.2.2 Asymptotic analysis of the parameters in the temporal eigenvalue problem

One of the decisive advantages of solving the mOSE (3.17) analytically, rather than discretely via numerical methods, is the possibility to apply analytical methods on the arising solutions. One such analysis was demonstrated in the previous section by deriving continuous modes based on the analytical solution (3.24). Another powerful and insightful mathematical tool is asymptotic analysis. In this mathematical framework, the behavior of a solution is investigated in asymptotic limits. In the context of LST, the goal is basically to understand, how the designated eigenvalue, here $\omega \in \mathbb{C}$, behaves for asymptotic limits of the parameters of the algebraic EVP (3.36), concretely α and Re. Notice that the inclusion of β is discarded in view of Squire's theorem explained in detail in 2.4.4, which states that the 2D stability problem provides the most critical Reynolds number and any 2D modes may be transformed to a corresponding 3D mode by variation of β. As such, the following asymptotic analysis is reduced

to the 2D case, for which the zero and infinite limits of α and Re are considered. The 3D EVP (3.36) then becomes

$$\begin{aligned}&\mathcal{D}(\omega)_{\alpha,\beta,Re}\\&= {}_2F_3\left(\begin{matrix}\boldsymbol{a_2}\\\boldsymbol{b_2}\end{matrix};-iRe\,\alpha\right)\left[iRe\,\alpha\,\frac{\overline{a}_4}{\overline{b}_4}\,{}_2F_3\left(\begin{matrix}\boldsymbol{a_4+1}\\\boldsymbol{b_4+1}\end{matrix};-iRe\,\alpha\right)-\left(\frac{\sigma+1}{2}\right){}_2F_3\left(\begin{matrix}\boldsymbol{a_4}\\\boldsymbol{b_4}\end{matrix};-iRe\,\alpha\right)\right]\\&- {}_2F_3\left(\begin{matrix}\boldsymbol{a_4}\\\boldsymbol{b_4}\end{matrix};-iRe\,\alpha\right)\left[iRe\,\alpha\,\frac{\overline{a}_2}{\overline{b}_2}\,{}_2F_3\left(\begin{matrix}\boldsymbol{a_2+1}\\\boldsymbol{b_2+1}\end{matrix};-iRe\,\alpha\right)-\alpha\,{}_2F_3\left(\begin{matrix}\boldsymbol{a_2}\\\boldsymbol{b_2}\end{matrix};-iRe\,\alpha\right)\right]=0,\end{aligned}\tag{3.54}$$

where for the parameters $\{a_i, b_i\}$ of the ${}_2F_3$ generalized hypergeometric functions $k = \alpha$ applies as $\beta = 0$. This 2D EVP now forms the basis for the subsequent analyses.

Asymptotic analysis for small streamwise wave numbers and large Re

In the context of turbulent superstructures, it is most interesting to first focus on the zero limit of α, as in this case very large streamwise wavelengths are analyzed as per $\lambda_x = 2\pi/\alpha$. The general approach is sketched briefly:

- Declare a limit for a parameter, i.e. $\alpha \to 0$
- Assume a Laurent series for the designated eigenvalue $\omega(\alpha)$, i.e.

$$\omega(\alpha) = \sum_{n=-\infty}^{n=\infty} \omega_n\,\alpha^n,\tag{3.55}$$

  in which ω_n denotes the coefficient of the nth power of α in the series
- Substitute $\omega(\alpha)$ into the algebraic EVP (3.54) and asymptotically expand the equation
- Sort all terms in the ensuing equation from leading order to lower orders
- Hierarchically solve for the coefficients ω_n to obtain the entire series (3.55)

If successful, the result for $\omega(\alpha)$ thoroughly describes how the eigenvalue ω behaves, in the present case, for $\alpha \to 0$. It could for instance tend towards an insignificantly low value, obtain a positive imaginary part and thus become unstable or change its asymptotic behavior depending on choice of the arbitrary parameter Re.
The asymptotic expansion for the zero limit of α has been conducted and logged in appendix A.1. In summary, the expansion of the EVP for $\alpha \to 0$ is not feasible for any choice of ansatz, regardless of whether a Laurent series ansatz is assumed for $\omega(\alpha)$ or any other possible ansatz function in fact. This result was confirmed numerically by unsuccessfully trying to solve (3.54) for ω in the presence of very small α and arbitrary Re. The conclusion therefore is that for $\alpha \to 0$ there exists no solution for the eigenvalue and, thus, $\omega = \emptyset$. Physically, this result is more than remarkable as it would imply that perturbations with large streamwise wavelength λ_x are not admitted by the flow.
This seemingly implausible result is resolved by extending the asymptotic analysis not only to the streamwise wave number α but simultaneously also to the Reynolds number Re. In fact, it is apparent that products of Re and α appear in multiple terms, both in the solution of the mOSE (3.24) as well as in the viscous parameter σ in (3.26b). This provides a direct

hint that both parameters should be treated together rather than individually in the context of asymptotic analyses. Thus, a novel expansion is proposed, with the assumption that

$$\alpha \to 0, \quad \text{and} \quad Re \to \infty, \tag{3.56}$$

where α is of inverse order of Re, i.e. the product is of $O(1)$. This, in turn, leads to a distinguished limit Re_α of the form

$$Re_\alpha := Re\,\alpha, = O(1). \tag{3.57}$$

If now solutions $\omega(Re, \alpha)$ exist for the EVP (3.54), this would in turn imply that perturbations with large streamwise wavelengths λ_x do in fact exist, but only in the large Re limit. These results would furthermore coincide with observations made by Hutchins and Marusic (2007), who reported a clear interdependence of large Reynolds numbers and large streamwise structures in a turbulent channel-flow. Corresponding results for the ASBL are thoroughly discussed in Khapko et al. (2016) and Ferro et al. (2021). This finding represents an important step towards explaining where turbulent superstructures originate from.
Now, wherever a pair $Re\alpha$ appears in the 2D EVP (3.54), as per (3.57) this product is replaced by Re_α. An ansatz of the form (3.55) once again is employed for ω. A first observation is that when (3.57) and (3.55) are employed into (3.54), subsequently expanding the EVP yields

$$\omega_n = 0 \qquad \text{for} \quad n \leq 0, \tag{3.58}$$

which reduces the Laurent series (3.55) to

$$\omega(\alpha) = \sum_{n=1}^{n=\infty} \omega_n\, \alpha^n. \tag{3.59}$$

It seems that the viscous parameter σ given in (3.26b) is of central importance for the expansion. Using (3.57) and (3.59) into (3.26b) yields

$$\sigma(\omega(\alpha)) = \sqrt{1 + 4iRe_\alpha\,(1-\omega_1)} - \frac{2iRe_\alpha\,\omega_2}{\sqrt{1 + 4iRe_\alpha\,(1-\omega_1)}}\,\alpha + O(\alpha^2), \tag{3.60}$$

in which now the leading order is $O(1)$, due to which σ is not singular, which would be the case for $n \leq 0$ in (3.59).
The next step is to expand the 2D EVP (3.54) with (3.57), (3.59) and (3.60). The detailed expansion is given in A.2. Considering only the leading order of the expanded 2D EVP now gives

$$\begin{aligned}\mathcal{D}(\omega_1, Re_\alpha)^{O(1)} = \frac{\omega_1}{\omega_1 - 1}\Bigg[&\frac{iRe_\alpha(\sigma_0 - 1)}{(1+\sigma_0)(3+\sigma_0)}\,{}_1F_2\left(\begin{matrix}\frac{1}{2}(1+\sigma_0)\\ (2+\sigma_0), \frac{1}{2}(5+\sigma_0)\end{matrix}; -iRe_\alpha\right)\\ &+ \frac{1}{2}(1+\sigma_0)\,{}_1F_2\left(\begin{matrix}\frac{1}{2}(-1+\sigma_0)\\ (1+\sigma_0), \frac{1}{2}(3+\sigma_0)\end{matrix}; -iRe_\alpha\right)\Bigg]\\ &- \frac{1}{1-\omega_1}\,{}_1F_2\left(\begin{matrix}\frac{1}{2}(-1+\sigma_0)\\ (1+\sigma_0), \frac{1}{2}(3+\sigma_0)\end{matrix}; -iRe_\alpha\right) = 0,\end{aligned} \tag{3.61}$$

where $\sigma_0 = \sqrt{1 + 4i\,Re_\alpha\,(1-\omega_1)}$ and the superscript $O(1)$ denotes that the leading order of the expansion is considered. The result is an expanded EVP for the eigenvalue $\omega_1(Re_\alpha)$, in which the only parameter is Re_α. Consequently, the leading order behavior of the eigenvalue

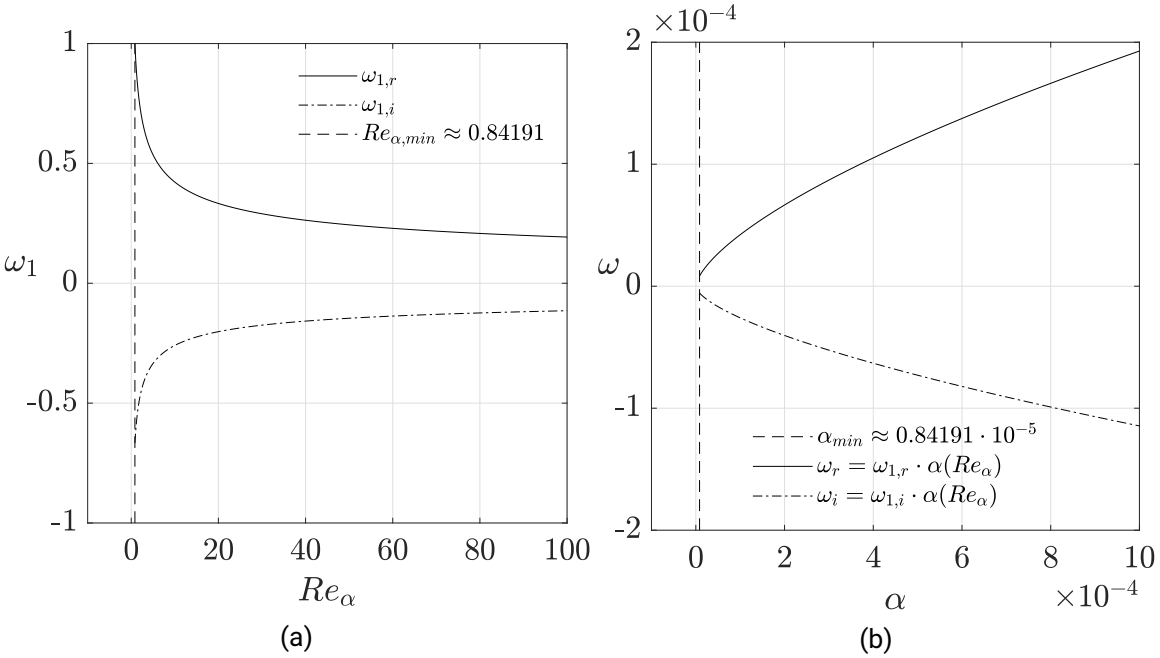

Figure 3.3: (a) The Laurent-series coefficient ω_1 in (3.59) is plotted vs. $Re_\alpha = Re\,\alpha$ as defined in (3.57). The lower threshold below which $\omega_1(Re_\alpha)$ yields no solutions is $Re_{\alpha,min} \approx 0.84191$. (b) Employing ω_1 into (3.59) and Re_α with a fixed Re into (3.57) gives the actual physical parameters ω and α, which is concretely plotted for $Re = 1.0 \times 10^5$. (adapted from Yalcin et al. (2021))

ω is dependent not only of a single parameter but rather of the interplay between Re and α. In figure 3.3a, the Laurent series coefficient ω_1 is plotted versus the distinguished limit Re_α. As is visible, for these limits, i.e. $\alpha \to 0$ and $Re \to \infty$, only a single solution curve exists. While at first it looks like the solution becomes singular for decreasing Re_α, it in fact reaches a lower limit at $Re_\alpha \approx 0.84191$, below which the expanded EVP (3.61) has no solution. Thus, for a given large Reynolds number, there is an upper bound for the streamwise wavelength λ_x of a perturbation. If larger perturbation shall be admitted to the system, the Reynolds number correspondingly needs to increase.
The computed solutions $\omega_1(Re_\alpha)$ should be converted to the desired eigenvalue ω and the actual parameter α. For this, first the range Re_α, which is analyzed in figure 3.3a must be employed into (3.57) to give a corresponding range of α by defining a fixed Reynolds number, which in figure 3.3b has been set to $Re = 1.0 \times 10^5$. Then, ω is obtained by substituting the acquired range α and the Laurent series coefficient ω_1 into (3.59). The resulting plot is given for the real and imaginary part of ω in figure 3.3b. As can be seen, the eigenvalue ω reaches an absolute minimum for $\alpha_{min} = 0.84191 \times 10^{-5}$, which by definition of Re_α (3.57) is of order $O(Re^{-1})$. Figure 3.4a shows the corresponding results for ω when solving the original EVP (3.54). The resulting eigenvalue curve shows that indeed $\alpha_{min} = 0.84191 \times 10^{-5}$ represents a cutoff wave number, below which no solutions are found. The employed solver was re-adjusted to residual tolerances as low as $O(10^{-200})$. It shows that the lack of solutions is not a numerical problem but rather a mathematical consequence of the actual EVP. Figure 3.4a also shows that the lower threshold is not a product of the asymptotic expansion but deeply engraved into the original EVP (3.54). The accuracy of the eigenvalues obtained from the expanded

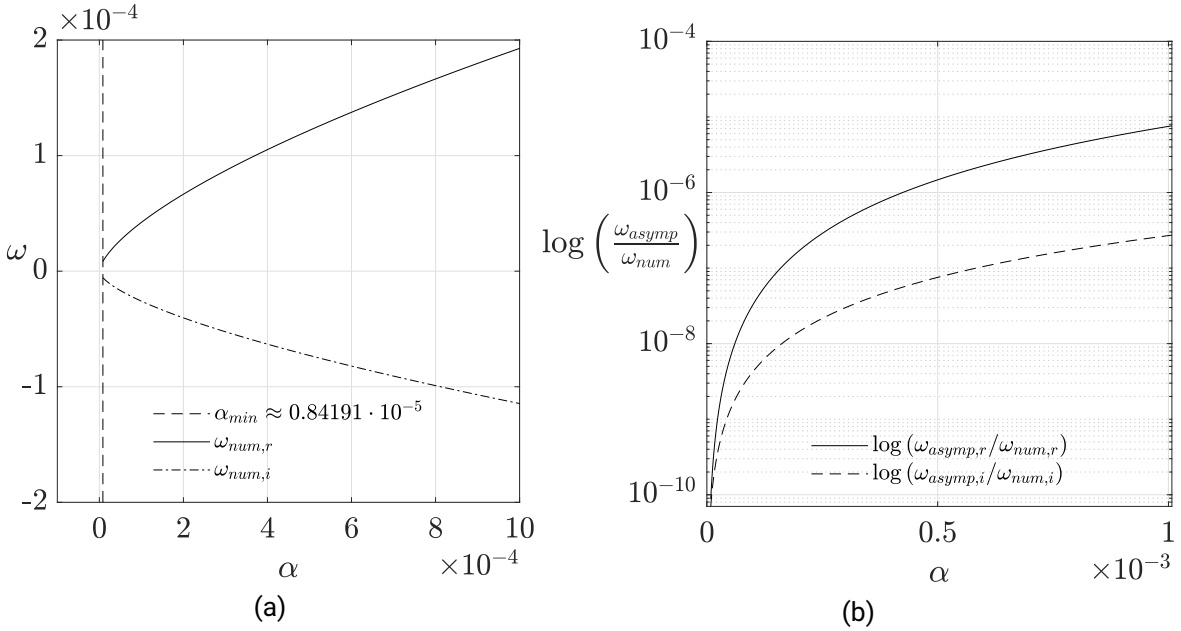

Figure 3.4: (a) Computations of solutions ω in the original EVP (3.54) for $Re = 1.0 \times 10^5$ in surrounding of the lower threshold $\alpha_{min} = 0.84191 \times 10^{-5}$, which is seemingly identical to the results obtained for the expanded EVP in figure 3.3b. (b) Visualization of the semi-logarithmic error of the eigenvalues computed from the expanded EVP (3.61) relative to the eigenvalues obtained from the full EVP (3.54). (adapted from Yalcin et al. (2021))

EVP (3.61) in relation to the eigenvalues from the original EVP are illustrated in figure 3.4b semi-logarithmically. Logically, the error for the smallest α is minimal and in the order of $O(10^{-10})$ whereas the error increases due to α gradually moving away from the zero limit assumed for the expanded EVP, where nevertheless good agreement between asymptotic and actual eigenvalues is observed.
A legitimization of the distinguished limit approach (3.57) may, in fact, be obtained by analyzing the underlying ODE, i.e. the mOSE (3.17). Therein, for $\alpha \to 0$, the terms scaling with the base velocity profile $U(y) = 1 - e^{-y}$ and its second derivative $U''(y)$ would be of negligible order compared to the remaining terms. As such, all information about the base flow would be lost in the zero limit of α. This occurrence is not restricted to the mOSE but also applies for the original OSE (2.43). In the context of stability theory, the information about the underlying base flow is naturally important. Conveniently, the terms scaling with the velocity profile $U(y)$ and its second derivative $U''(y)$ are accompanied by the Reynolds number Re. It is therefore possible to keep these terms in the leading order, if in addition to $\alpha \to 0$ the aforementioned limit $Re \to \infty$ is assumed. Reintroducing the distinguished limit Re_α as defined in (3.57) and expanding the mOSE (3.17) finally gives

$$\frac{\mathrm{d}^4\tilde{v}(y)}{\mathrm{d}y^4} + \frac{\mathrm{d}^3\tilde{v}(y)}{\mathrm{d}y^3} - \left(iRe_\alpha - iRe_\alpha \frac{\omega}{\alpha} - iRe_\alpha\, e^{-y}\right) \frac{\mathrm{d}^2\tilde{v}(y)}{\mathrm{d}y^2} - iRe_\alpha\, e^{-y}\, \tilde{v}(y) + O(\alpha) = 0, \quad (3.62)$$

for the 2D case. Additionally, in order to retain the eigenvalue ω in (3.62), ω must be of the same order as α. This is the case if the reduced Laurent series (3.59) is assumed for ω, i.e.

$$\omega(\alpha) = \omega_1 \alpha + O(\alpha^2). \quad (3.63)$$

Therefore, the distinguished limit (3.57) as well as the leading order of the Laurent series

(3.59) are reconfirmed by asymptotic expansion of the mOSE (3.17).
In summary, the 2D EVP (3.54) may only be expanded in the zero limit of α if simultaneously the infinite limit of Re is assumed. It was shown that the ensuing expanded EVP (3.61) yields a lower threshold $Re_{\alpha,min} \approx 0.84191$ below which there are no solutions for ω_1 and, thus, for ω. This in turn implies that for a given large Reynolds number, there is a cutoff streamwise wave number α or wavelength λ_x, which defines the size of the largest structures in streamwise direction. This finding corresponds to famous results in open channel-flow and the ASBL (Hutchins and Marusic, 2007; Khapko et al., 2016; Ferro et al., 2021). To the best knowledge of the present author, these results obtained via asymptotic analyses are unprecedented and mark an important milestone in linking turbulent superstructures and linear modes in the laminar base state of a wall-bounded shear flow.

Asymptotic analysis of the inviscid limit $Re \to \infty$

The thorough analysis of the inviscid case, i.e. $Re \to \infty$, has been treated in detail for the analytical solution of the mOSE in Baldwin (1970) and in a more recent study based on the triple-deck theory published by Dempsey and Walton (2017) based on the LNSE (2.36) for the ASBL. Baldwin's results are purely mathematical and discarded at this point due to a lack of replicability. In the more recent work by Dempsey and Walton (2017), a triple-deck behavior was introduced for the perturbed ASBL in the limit of large Reynolds numbers for the lower branch of the neutral stability curve, as shown later in 3.5. Incidentally, the theory of triple decks was developed to better understand BL separation Stewartson and Williams (1969), Messiter (1970), and Neiland (1970), but the theory can also be used to derive the asymptotic behavior of the lower neutral branch. For this case, the stationary ASBL is decomposed into three physically distinct parts, namely the lower, main, and upper decks. In the corresponding analysis, asymptotic expansions in each deck combined with the BC for the perturbation velocities as well as fitting conditions in the transition regions yield that the lower branch in the limiting case of large Reynolds number is given asymptotically by $\alpha = O(Re^{-1/4})$. The asymptote is plotted in a point-dashed line in 3.5 and qualitatively seem to replicate the actual lower branch computed in the following section.

3.2.3 Temporal stability characteristics of the asymptotic suction boundary layer

To the author's knowledge, neither the temporal nor the spatial stability map for the ASBL have been fully published and thoroughly analyzed. Both for the following computations of the temporal 2D EVP (3.54) as well as for the spatial computations presented in section 3.3, Muller's algorithm, a second order secant method, was used to compute the solutions ω parametrized by α and Re. The critical value triple $[\alpha_{cr}, \omega_{cr}, Re_{cr}]$ is compared with the value obtained by a numerical solutions of the mOSE by Hocking (1975) and Fransson and Alfredsson (2003).

The remaining asymptotic analyses for $\alpha \to \infty$ and $Re \to 0$ are to be found in the appendix in the sections A.3 and A.4.

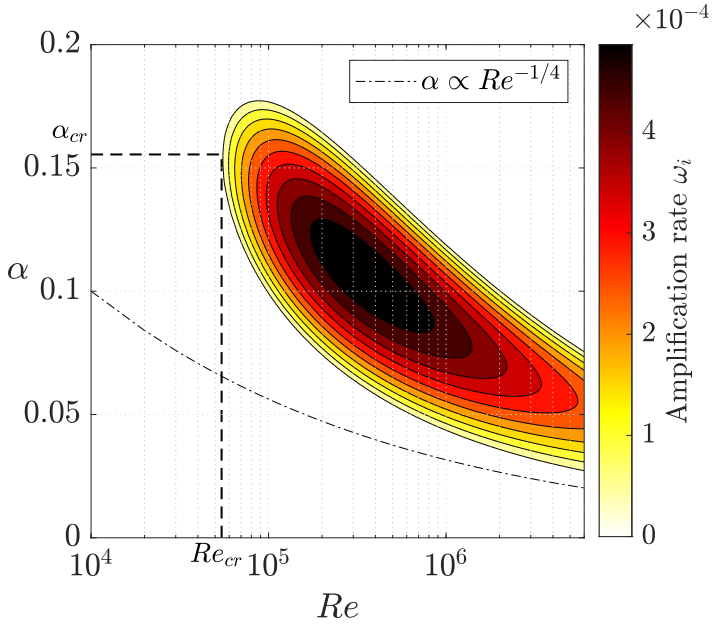

Figure 3.5: Depiction of the 2D temporal stability map presenting the temporal growth rate of the least stable TS modes as discussed in figure 2.2. The colored shades represent unstable modes whereas blank areas are areas of stability. The Reynolds number axis is given logarithmically. The point-dashed line gives the asymptote derived by Dempsey and Walton (2017) via the triple-deck theory for large Re. (adapted from Yalcin et al. (2021))

Computations of the temporal Tollmien-Schlichting modes of the asymptotic suction boundary layer

The principal goal of LSA is to find the least stable modes, the TS modes, for a given set of parameters $\{\alpha, Re\}$ and discern at which Reynolds number the temporal growth rate becomes positive for the first time, which would in turn correspond to modes growing for $t \to \infty$. The respective parameter set is called critical parameter set $\{\alpha_{cr}, \omega_{cr}, Re_{cr}\}$, where $\omega_i = 0$. The visualization is typically done in a temporal stability map, which represents a contour plot, where ω_i is plotted vs. Re and α. The temporal stability map showing only the TS modes for the ASBL is shown in figure 3.5 and was computed up for Reynolds numbers between $Re = 1.0 \times 10^4$ – 6.0×10^6 and streamwise wave numbers between $\alpha = 0.001 - 0.2$. Larger streamwise wave numbers were examined for sample supercritical Reynolds numbers $Re > Re_{cr}$ and were found to yield stable modes with ω_i exclusively. Based on the asymptotic analysis conducted for large α (see section A.3) extensive computations were not performed globally for larger streamwise wave numbers, as expanding the EVP (3.54) $\alpha \to \infty$ gives $\omega_i < 0$, i.e. stable modes without exception. The stabilizing effect of suction on BL stability is best studied by comparing the critical value triple of the ASBL profile to the BBL. Critical values were first calculated by Hocking (1975), who gave $\{\alpha_{cr,ASBL} = 0.1555, \omega_{cr,ASBL} = 0.023325, Re_{cr,ASBL} = 54370\}$ by solving the LNSE in streamfunction formulation with methods first employed in Stewartson and Stuart (1971), in which a plane Poiseuille profile was examined. The initial-value problem is investigated with asymptotic and multi-scale methods. For a detailed approach, the reader is referred to the cited papers. In more recent years, a different critical value triple was obtained by Fransson and Alfredsson (2003), who employed a Chebyshev collocation method

in wall-normal direction. The triple computed in this work was given as $\{\alpha_{cr,ASBL} = 0.1555$, $\omega_{cr,ASBL} = 0.02331$, $Re_{cr,ASBL} = 54382\}$. Due to the approximating nature of both approaches, the true critical value triple remained unknown. In this work we use the EVP (3.54) based on the analytical solution (3.24) to accurately calculate the critical value triple up to $O(10^{-22})$ and with high decimal accuracy even for the Reynolds number. For this, a 2D bisection method was employed to narrow down the critical point systematically. Such a method is highly dependent on the starting point, the computations were tracked manually to adjust the parameter range when necessary. The critical value triple computed in this work based on (3.54) is

$$\alpha_{cr} = 0.15546, \tag{3.64a}$$
$$\omega_{cr} = 0.023297, \tag{3.64b}$$
$$Re_{cr} = 54378.62032, \tag{3.64c}$$

of which the Re_{cr} is in fact located between the previously given critical Reynolds numbers provided by Hocking (1975) and Fransson and Alfredsson (2003). The residuum of the EVP (3.54) with the critical values in (3.64c) is of order $O(10^{-22})$, while the positive imaginary part $\omega_{cr,i}$ is of order $O(10^{-14})$. It should be mentioned that due to the analytical nature of the EVP (3.54), the residuum as well as the decimals in (3.64c) can be refined further, with computation time being the only limiting factor. The point to be made is that numerical schemes, such as Chebyshev collocation schemes, provide results which are highly dependant on factors such as the used mappings, the number of collocation points or the cut-off length L. The form of the stability map in figure 3.5 is reminiscent of a stability map for the BBL. For increasing Reynolds numbers the upper and lower branch of the neutrally stable curve relocate to lower streamwise wave numbers. Simultaneously, both branches move closer to each other as the Reynolds number increases. It is worth noticing that global stability is ensured for any streamwise wave number $\alpha \geq 0.178$, regardless of the Reynolds number and this is also validated by the asymptotic analysis for $\alpha \to \infty$.

Temporal eigenvalue spectra and the corresponding wall-normal eigenfunctions $\tilde{v}(y)$

For each parameter combination of Re and α there exists a spectrum consisting of the TS mode as well as additional modes representing further solutions of the EVP (3.54). We aim to answer two questions about these temporal spectra:
(i) How do the spectra behave for varying Re and α?
(ii) How do the TS waves behave for varying Re and α?
With the multiple eigenvalues admitted by (3.54) computation strongly depends on an initial guess and also delivers only one value at a time. Hence, a two-step scheme is employed. First, all spectra were estimated using a Chebyshev collocation scheme. For the computation, the semi-infinite domain normal to the wall was truncated at $L = 500$ and mapped to $\eta \in [-1, 1]$ using an algebraic linear mapping of the form

$$y = \frac{L}{2}(\eta + 1), \tag{3.65}$$

where η denotes the resulting mapped wall-normal coordinate. The number of collocation points were set to $n = 600$. We note that the emerging spectra were strongly influenced by the truncation length L as well as the number of collocation points n.
It is important to notice that the sole employment of Chebyshev schemes is not sufficient to

acquire physically correct spectra due to the existence of spurious modes. Hence, in in order to filter out spurious modes as well as drastically increase the accuracy of higher modes in the spectra, all resulting modes were reiterated on account of the analytical EVP (3.54). For this purpose, all modes obtained by the Chebyshev method were employed as starting points into the non-linear root finder described in section 3.2.3. The residuals for the EVP (3.54) were set to a very low threshold, until the iteration was halted. It proved necessary to set this threshold to $tol = 10^{-80}$, except for the case $Re = 500000$, where a tolerated residual of $tol = 10^{-100}$ had to be taken. The reason for these very low residuals was the persistence of some spurious modes, which did not disappear for lower residuals. For this reason the number of digits had to be increased to 100 and 120 respectively.

The resulting spectra are shown in figures 3.6 and 3.7. In figure 3.6 the spectra were computed for a fixed $Re = Re_{cr}$ and varying α. Branches of unfiltered eigenspectra for plane Poiseuille flow were classified in Mack (1976) as an A-branch when $c_r \to 0$, a P-branch when $c_r \to 1$ or an S-branch when $c_r \to 2/3$, with c_r denoting the real part of the phase velocity. Even though inherently different, the eigenvalue spectra for the BBL (Schmid et al., 2002) were in fact classified analogously, in which the continuous spectrum was described as a hybrid P-S-mode family, whereas the scattered modes made up the A-mode family. Due to the conceptual similarity to the eigenspectrum of the BBL, the seemingly scattered modes computed and visualized in figures 3.6 and 3.7 are identified as modes in the A-mode family.

In figure 3.6 the eigensprectra in Re_{cr} are compared for varying orders of α. For very small $\alpha = 0.001$ (see figure 3.6a) the spectrum is sparse, while already showing a behavior that is maintained for other α, i.e. the spectrum in most cases maintains a mode very close to the continuous spectrum with the remaining modes sparsely connecting TS mode and the mode in the vicinity of the continuous spectrum. In figure 3.6b the amount of modes increase, seemingly forming an arch-like structure. For the critical $\alpha = \alpha_{cr}$, however, an additional second quasi-branch seems to emerge (see figure 3.6c), featuring two ”off-track” modes, while the far right mode is separated from the rest of the spectrum. Finally, the gap between the far right mode and the rest of the modes appears to widen towards the largest $\alpha = 1$, given in figure 3.6d.

Comparison of various orders of Re at the critical wave number α_{cr} curiously reveals a similar behavior of the spectrum. The smallest Reynolds number $Re = 500$ (see figure 3.7a) features a rather sparse spectrum, again containing a TS mode, a far right mode and modes in between. The number of modes increases at first with increasing Reynolds numbers ($Re = 5000$, see figure 3.7b). Increasing the orders then again unveils the aforementioned second branch, which for the largest Reynolds number $Re = 500000$ gains additional modes (see figure 3.7d). Interesting enough, for this Reynolds number the far right mode seems to disappear, which could be verified by reducing the tolerated residual of the EVP (3.54) as well as increasing the number of digits in Maple.

For the critical point (3.64c), selected eigenfunctions $v_r(y)$ are plotted in figures 3.8a - 3.8d by substituting the parameters α and Re as well as the eigenvalue ω of interest, taken from figure 3.7c, into (3.34). In general, a trend can be observed in the evolution of the eigenfunctions with increasing proximity to the continuous spectrum. While the TS eigenfunction shows typical behavior in figure 3.8a, the modes very close to the continuous spectrum induce oscillatory wall-normal eigenfunctions (see figures 3.8c and 3.8d). Interesting enough, these oscillatory eigenfunctions seemingly form a symmetric band with respect to some mid-point in y, in which they are non-zero with some distance to the wall.

Due to their relevance for the stability of the flow, it remains to be examined which factors

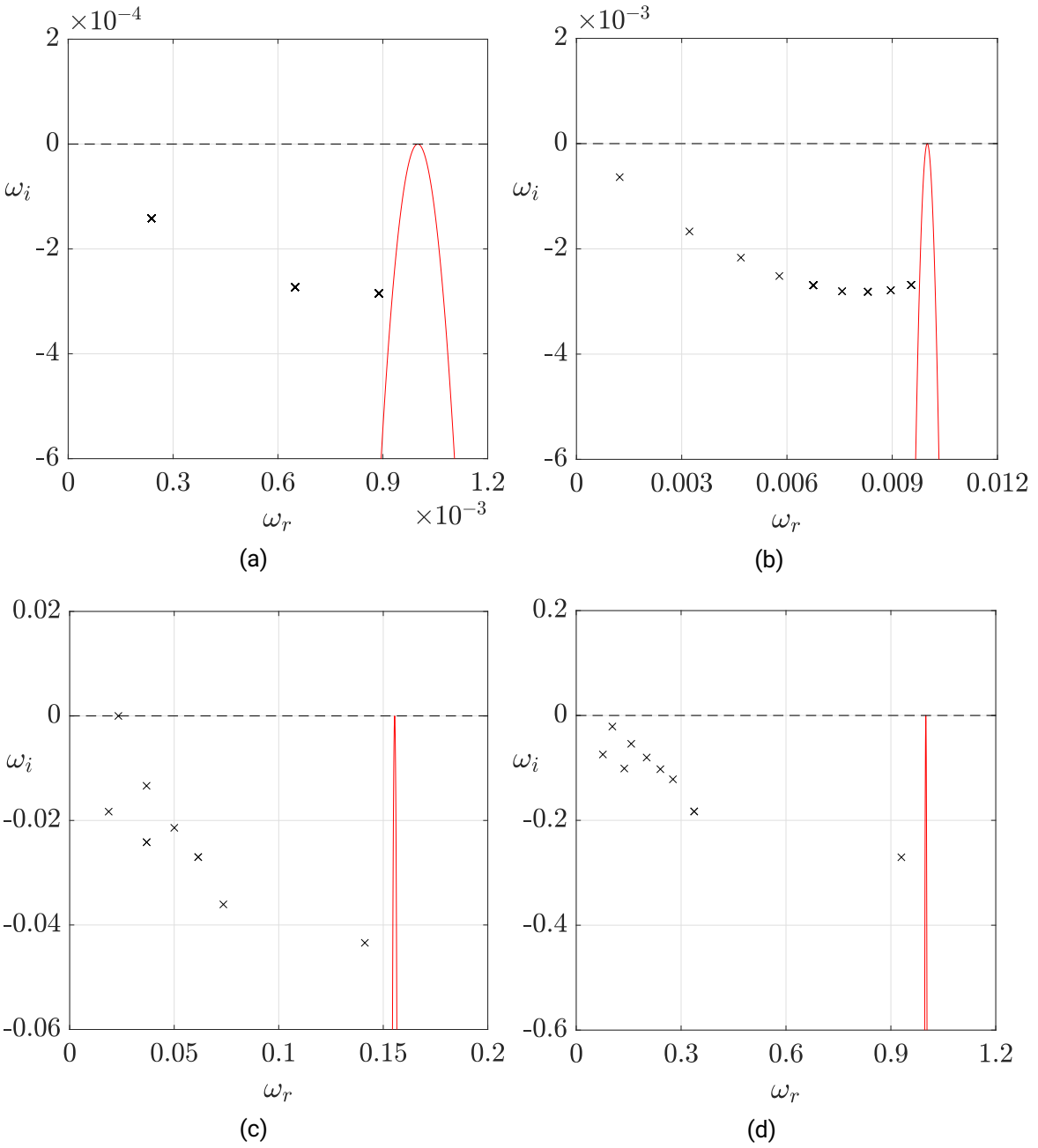

Figure 3.6: Temporal spectra are displayed at fixed $Re_{cr} = 54378.62032$ and varying α: (a) $\alpha = 0.001$; (b) $\alpha = 0.01$; (c) $\alpha_{cr} = 0.15546$; (d) $\alpha = 1$. Here and in figure 6 the red parabola denote the temporal continuous spectra given by (3.52). (adapted from Yalcin et al. (2021))

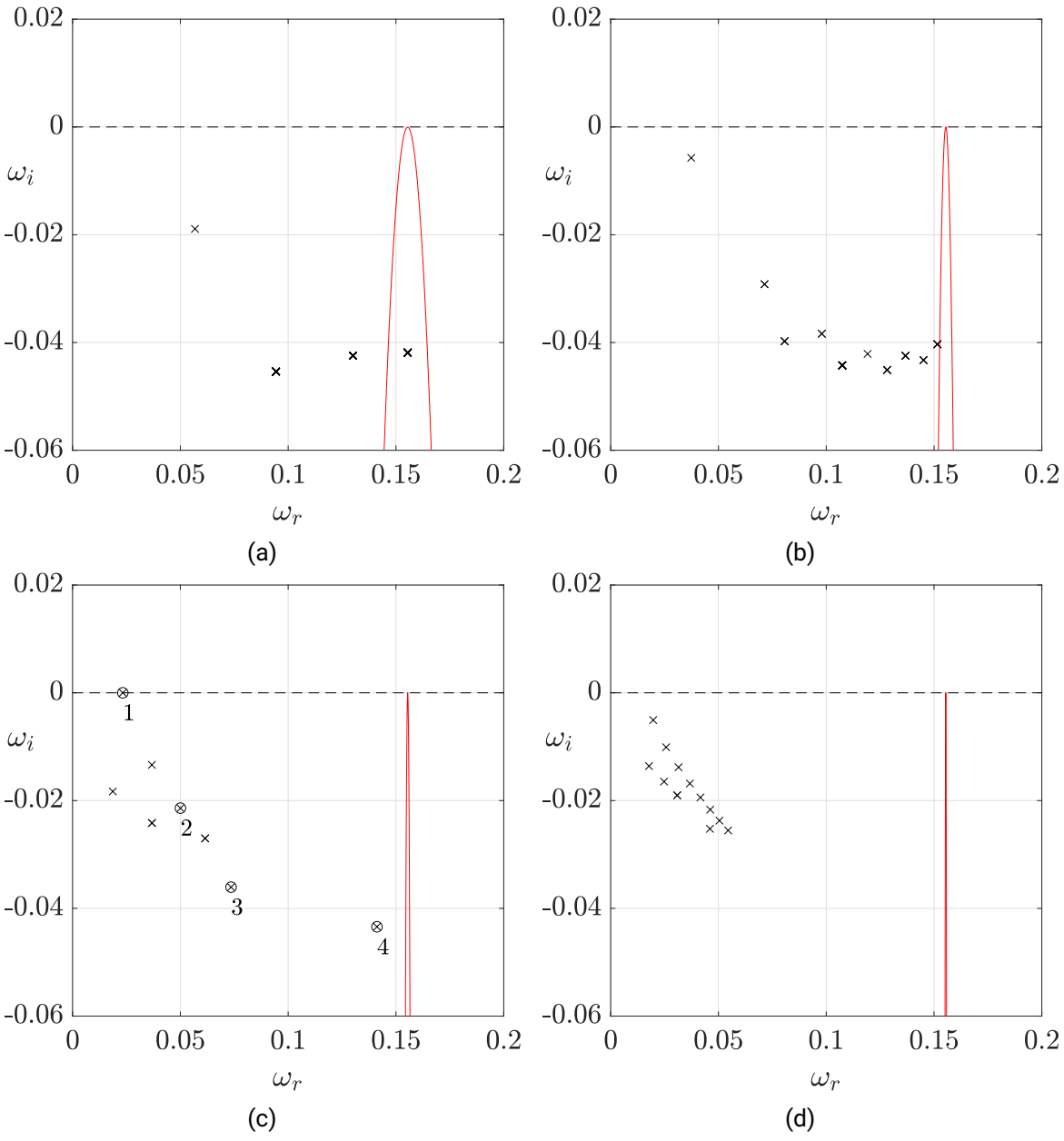

Figure 3.7: Temporal spectra are displayed at fixed $\alpha_{cr} = 0.15546$ and varying Re: (a) $Re = 500$; (b) $Re = 5000$; (c) $Re_{cr} = 54378.62032$; (d) $Re = 500000$. The spectra were obtained analogous to figure 3.6. Eigenfunctions of the eigenvalues $1 - 4$ in figure (c) are shown in figure 3.8. (adapted from Yalcin et al. (2021))

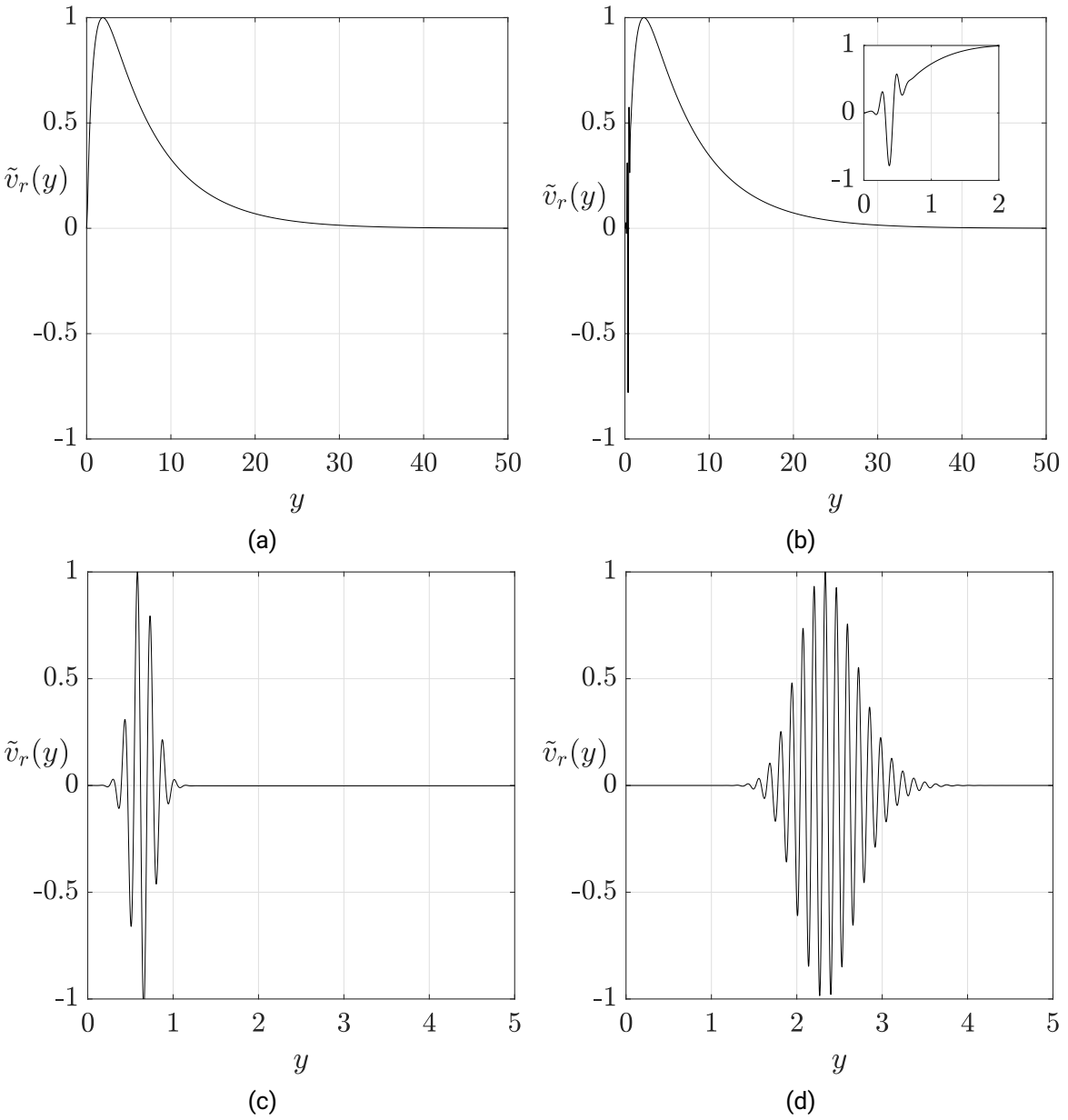

Figure 3.8: Eigenfunctions of the wall-normal disturbance $v_r(y)$ vs. y are plotted for the critical parameters Re_{cr} and α_{cr} given in (3.64c). The corresponding ω are given in figure 3.7c where eigenfunctions for selected ω are shown: (a) $\omega_1 = 0.023296$, (b) $\omega_2 = 0.050041 - 0.021402i$, (c) $\omega_3 = 0.073523 - 0.036063i$, (d) $\omega_4 = 0.14120 - 0.043418i$. (adapted from Yalcin et al. (2021))

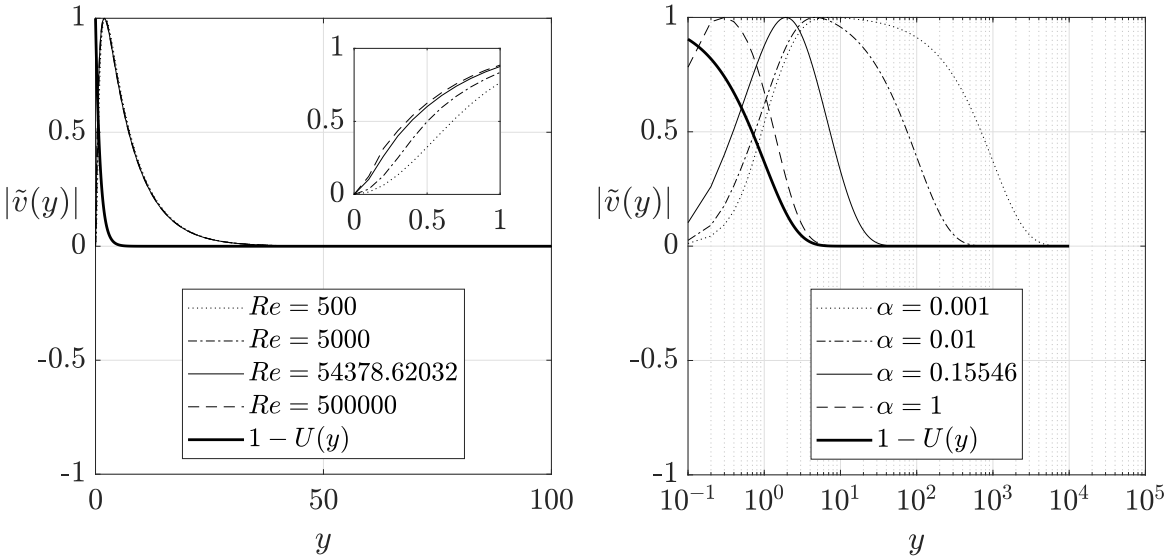

Figure 3.9: TS eigenfunctions $\tilde{v}_r(y)$ parametrized by Re at fixed $\alpha = \alpha_{cr}$ (a) and α at fixed $Re = Re_{cr}$ (b). The critical parameters can be taken from (3.64c). For comparison we have displayed the laminar base solution in the form $1 - U(y)$. (adapted from Yalcin et al. (2021))

influence the reach of the possibly unstable TS modes into the far-field. For this, the magnitude of the eigenfunctions $|\tilde{v}(y)|$ is plotted vs. y for varying Re and fixed α_{cr} (see figure 3.9a) and for varying α and fixed Re_{cr} (see figure 3.9b). It is quite remarkable that varying the orders of Re hardly affects the decay of $|\tilde{v}(y)|$ in wall-normal direction while varying α influences the reach of $|\tilde{v}(y)|$ into the far-field decisively. This finding describes quantitatively how the magnitude of the eigenfunction $\tilde{v}(y)$ behaves for varying Re and α. In comparison to the laminar base flow, especially such TS waves comprised by small α, severely outreach the BL thickness δ by many factors. The investigation of $|\tilde{v}(y)|$ therefore indicates that the inviscid part of the eigenfunction, i.e. the term decaying with $e^{-\alpha y}$ in $\tilde{v}(y)$ as given in (3.34), dominates. It is quite enlightening, however, to extend the analysis to the perturbation velocity $v(x, y, t) = \tilde{v}(y)\, e^{i(\alpha x - \omega t)}$. When employing the eigenfunction $\tilde{v}(y)$, given in (3.34), into the normal mode ansatz (NMA) (2.54), one gets

$$\begin{aligned} v(x,y,t) &= \tilde{v}(y)\, e^{i(\alpha x - \omega_r t)}\, e^{\omega_i t} \\ &= e^{i(\alpha x - \frac{\sigma_i}{2} y - \omega_r t)}\, e^{-\frac{\sigma_r + 1}{2} y + \omega_i t}\, {}_2F_3\left(\begin{matrix}\boldsymbol{a_4}\\ \boldsymbol{b_4}\end{matrix}; -iRe\,\alpha\, e^{-y}\right) \\ &\quad - \hat{c}\, e^{i(\alpha x - \omega_r t)}\, e^{-\alpha y + \omega_i t}\, {}_2F_3\left(\begin{matrix}\boldsymbol{a_2}\\ \boldsymbol{b_2}\end{matrix}; -iRe\,\alpha\, e^{-y}\right), \end{aligned} \tag{3.66}$$

with $\hat{c} = {}_2F_3\left(\boldsymbol{a_4}, \boldsymbol{b_4}; -iRe\,\alpha\right) / {}_2F_3\left(\boldsymbol{a_2}, \boldsymbol{b_2}; -iRe\,\alpha\right)$ and σ_r and σ_i as defined in (3.48a) and (3.48b). It becomes apparent that each wall-normal velocity perturbation is comprised by two waves, one wave due to the viscous part of the solution moving in the $x - y$ plane, i.e. the first addend in (3.66), and the inviscid part moving purely in streamwise direction which is comprised by the second addend in (3.66). In the limit $y \to \infty$ the ${}_2F_3$ hypergeometric functions asymptotically converge to 1, which gives

$$\lim_{y \to \infty} v(x,y,t) = e^{i(\alpha x - \frac{\sigma_i}{2} y - \omega_r t)}\, e^{-\frac{\sigma_r + 1}{2} y + \omega_i t} - \tilde{c}\, e^{i(\alpha x - \omega_r t)}\, e^{-\alpha y + \omega_i t}. \tag{3.67}$$

Comparison with Mack (1976) unveils that in the limit of large y two analogous wave components also exists in the BBL of the form

$$\lim_{y\to\infty} v_{BBL}(x,y,t) = e^{i(\alpha x-\sigma_{BBL,R}\, y-\omega_r t)} e^{-\sigma_{BBL,I}\, y+\omega_i t} + \tilde{c}\, e^{i(\alpha x-\omega_r t)} e^{-\alpha y+\omega_i t}. \tag{3.68}$$

Now, clearly for the ASBL two specific decay mechanisms occur in y - direction:

(i) The viscous wave propagating in the x-y-plane decays with $e^{-\frac{\sigma_r+1}{2}y}$.
(ii) The inviscid wave propagating in x-direction which decays with $e^{-\alpha y}$.

In order to capture the full dynamics, we will conduct a separate analysis of each respective wave as both wave parts have different propagation directions. An analysis of the inviscid waves was already conducted in figures 3.9a and 3.9b, as the inviscid waves seemingly dominate the magnitude of $\tilde{v}(y)$, which as we will see in section 3.2.3 is true for any combination of α and Re. However, an analysis of the viscous waves needs to be conducted still. For this purpose, the propagation angle as well as the decay rate of the viscous waves are examined in the following section.

Directional wave-propagation of viscous waves and their spatial y-decay

From (3.66), the viscous wave part of the wall-normal perturbation velocity $v(x,y,t)$ is given by

$$v_{vis}(x,y,t) = e^{i(\alpha x-\frac{\sigma_i}{2}y-\omega_r t)}\, e^{-\frac{\sigma_r+1}{2}y+\omega_i t}\, {}_2F_3\left(\begin{matrix}\boldsymbol{a_4}\\ \boldsymbol{b_4}\end{matrix}; -iRe\,\alpha\, e^{-y}\right). \tag{3.69}$$

There are two essential pieces of information that can be extracted from (3.69), the wave propagation angle θ as well as a measure of length characterizing the spatial decaying behavior for large y.
On top of the already known streamwise wave number α, we may define a wall-normal wave number $\frac{\sigma_i}{2}$. The comparison of the signs of α and σ_i determines whether the viscous waves move towards or away from the wall. The sign of σ_i is determined by $\text{sgn}(\alpha-\omega_r)$, as is given in (3.48b). For the domain $1.0\times10^4 \leq Re \leq 1.0\times10^6$ and $1.0\times10^{-4} \leq \alpha \leq 1.0$ it turns out that $\alpha-\omega_r > 0$ and $\omega_r > 0$. Thus, α and $-\frac{\sigma_i}{2}$ without exception bear opposing signs while $\omega_r > 0$, due to which the viscous waves defined in (3.69) in all cases move towards the wall at a propagation angle

$$\theta = \arctan\left(-\frac{\sigma_i}{2\alpha}\right). \tag{3.70}$$

The magnitude of $\frac{\sigma_r+1}{2}$ on the other hand determines at what rate the viscous waves (3.69) decay in wall-normal direction. In this sense, the inverse

$$\delta_\sigma = \frac{2}{\sigma_r+1}, \tag{3.71}$$

defines a characteristic length scale, which describes how far into the far-field the viscous waves persist. Further, if transformed back to dimensional quantities, we observe that δ_σ is a multiple of the BL displacement thickness $\delta_1 = \nu/V_0$. Hence, this quantity hereafter is called wave decay-rate length (WDRL).
Now, σ_r in (3.48a) by definition is always positive. Hence, δ_σ reaches a maximum when σ_r becomes minimal (or ideally zero). Close examination of (3.48a) reveals that σ_r in fact becomes

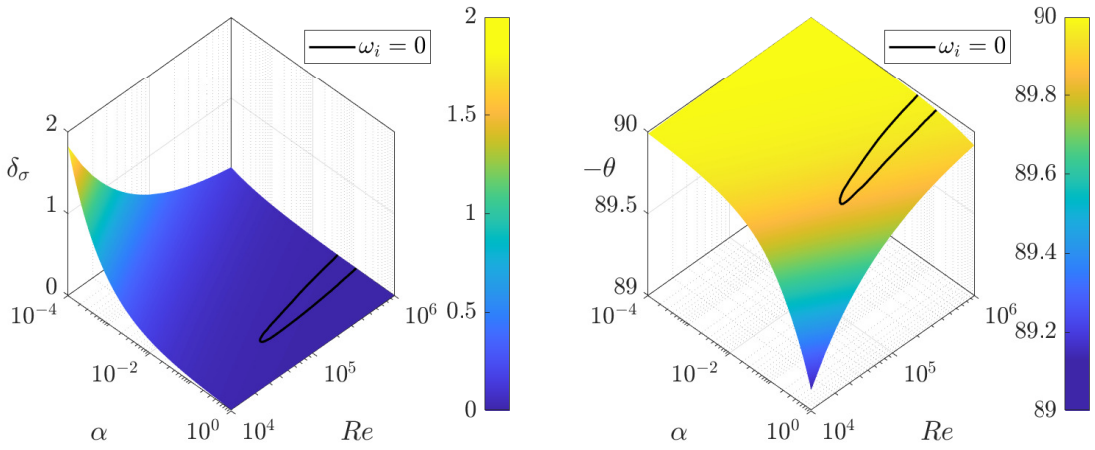

(a) (b)

Figure 3.10: (a) WDRL δ_σ as given in (3.71) as a function of α and Re. (b) Wave propagation angle Θ as given in (3.70) as a function of α and Re (in degrees) (adapted from Yalcin et al. (2021))

minimal when $\alpha = \omega_r$ and ω_i is negative. While negative ω_i are quite common, the question is pending whether or not there is a point at which α is indeed equal to ω_r. If such a case occurs, it would have great effect on the longevity of the viscous modes into the far-field. And indeed, there is a very specific point at which α is equal to ω_r! Such an occurrence was witnessed in section 3.2.2 when the necessity of a distinguished limit emerged in order to expand the EVP (3.54) for very small wave numbers. It became apparent that only for $Re_\alpha = Re\,\alpha = O(1)$ do solutions for ω exist in the zero limit of α. A computation of the expanded EVP (3.61) revealed a lower threshold for $Re_{\alpha,min} \approx 0.84191$, below which no solutions exist for ω. In the limit $Re_\alpha \to Re_{\alpha,min}$, however, the eigenvalue ω converges towards $\omega_{min} = \alpha - i\frac{2}{3}\alpha$. Thus, for the lower threshold of Re_α does the extraordinary case $\omega_r = \alpha$ occur. In this point, σ_r becomes minimal and gets very close to zero.

This result may be verified in figure 3.10a. In this figure, the WDRL δ_σ is calculated and visualized for the given parameters. In almost the entire parameter range is $\delta_\sigma < 1$, which means that the WDRL is smaller than the displacement thickness δ_1. However, at $Re = 1.0 \times 10^4$ and $\alpha = 1.0 \times 10^{-4}$ a maximum for δ_σ can be witnessed, clearly approaching the theoretical maximum $\delta_{\sigma,max} = 2$. In this point, the WDRL becomes larger than δ_1. In other words, the viscous waves clearly reach well into the far-field. It is quite remarkable that the distinguished limit theorized in section 3.2.2 eventually plays a key role for the WDRL. This shows that this limit indeed has an actual physical significance for the perturbation waves.

The wave propagation angle θ defined in (3.70) is additionally plotted for the same parameter range in figure 3.10b. It is important to notice that the wave propagation angle θ remains close to 90 degrees throughout the entirety of the analyzed parameter region $[\alpha, Re]$. The viscous part of the wave (3.66) as a result has almost no streamwise variation for the Reynolds numbers investigated in figure 3.10b, being emitted perpendicular to the wall into the far-field, where the viscous wave eventually decays. An exemplary viscous TS wave is given in figure 3.11. The wave characteristics are calculated by (3.69) with the given parameters $Re = 1.0 \times 10^4$ and $\alpha = 1.0 \times 10^{-4}$ giving $Re_\alpha = 1.0$ as per (3.57). Hence, the parameters are very close to the minimum of the distinguished limit $Re_{\alpha,min} \approx 0.84191$, for which due to the explanations regarding figure 3.10a the WDRL is almost maximal and via (3.71) is calculated to $\delta_\sigma = 1.82360$.

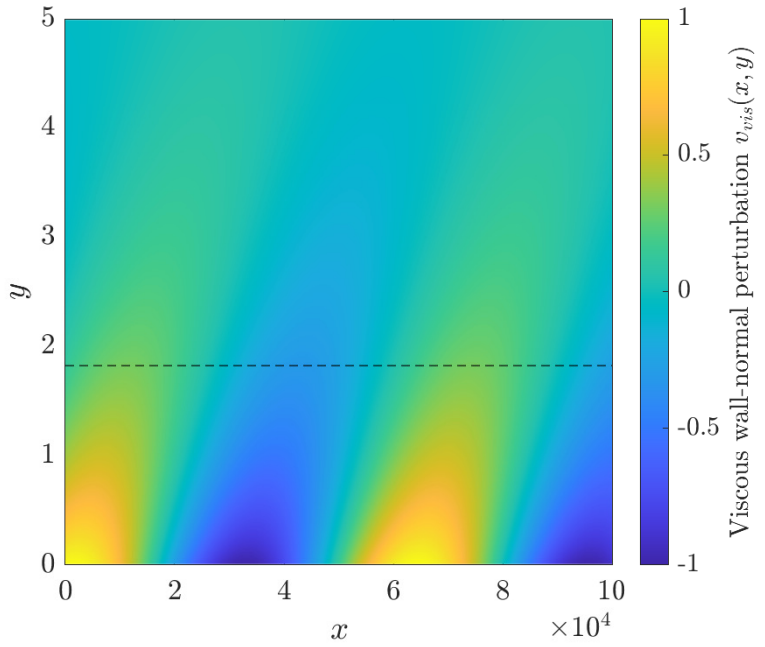

Figure 3.11: Viscous part of the harmonic wall-normal perturbation velocity (3.66) rescaled to unity at $Re = 1.0 \times 10^4$ and $\alpha = 1.0 \times 10^{-4}$, accounting for $Re_\alpha = 1.0$. The black-dashed line represents the WDRL (3.71), which for the present wave gives $\delta_\sigma = 1.82360$. The propagation angle yields $\theta = 89.99064°$.

As such, the viscous wave persists well into the free-stream. A striking feature of the wave is an extreme elongation into the streamwise direction with $\lambda_x = 2\pi \times 10^4$ as well as a propagation angle of $\theta = 89.99064°$, i.e. approximately a right angle. In the context of large-scale structures, further investigation of modes very close to the distinguished limit are motivated due to this streamwise elongation and persistence into the far-field.

3.2.4 Symmetry-induced ansatz modes

Throughout this work the ansatz of choice for transform the LNSE to a system of ODE, namely the coupled OSE and SE, was the classical NMA, leading to the mOSE as given in (3.17). However, it was shown previously in Nold and Oberlack (2013) that for linear plane shear flows a specific symmetry induces the Kelvin mode as well as a merging of Kelvin and normal modes. Also, for shear flows of algebraic, exponential and logarithmic form additional symmetries exist, which induce other alternative ansatz functions for the eigenfunctions (Nold and Oberlack, 2013; Nold et al., 2015). Very recently, the existence of such symmetry-induced ansatz functions were derived on analyzed for rotational shear flows by Gebler et al. (2021), who discovered novel alternative modes with algebraic growth mechanisms and subsequently conducted numerical simulations visualizing remarkable large-scale patterns in the 2D plane. Based on the methods presented in these works, two new invariant ansatz functions were derived for the ASBL by Mirzayev (2016). The analysis was conducted for the 2D inviscid LNSE with a ASBL base

profile, which in stream function formulation is given as

$$\left[\frac{\partial}{\partial t} + (1 - e^{-y})\,\frac{\partial}{\partial x} - \frac{1}{Re}\,\frac{\partial}{\partial y}\right]\,\Delta\Psi + e^{-y}\,\frac{\partial \Psi}{\partial x} = 0. \tag{3.72}$$

The underlying Lie algebra is then given by

$$\begin{aligned} X_1 = \frac{\partial}{\partial t} \qquad X_2 = \frac{\partial}{\partial x} \qquad X_3 = \Psi\frac{\partial}{\partial \Psi} \qquad X_4 = e^{\frac{1}{Re}}\left[\frac{\partial}{\partial t} + \frac{\partial}{\partial x} - \frac{1}{Re}\frac{\partial}{\partial y}\right], \\ X_\theta = \theta(x,y,t)\,\frac{\partial}{\partial \Psi}. \end{aligned} \tag{3.73}$$

The symmetries X_1 and X_2 stand for translations in time and space while X_3 stands for a scaling symmetry in the stream function. These symmetries would also arise in the viscous LNSE. However, the fourth symmetry X_4 - only present in the inviscid case - is novel and lays the ground for the derivation of new invariant ansatz function. The detailed derivation of the now presented Lie algebra as well as the ansatz functions can be found in Mirzayev (2016). Notice that that results here are different, as Nold only considered the case $V_0 = 0$.

Double-exponential ansatz function

Employing the symmetries X_2, X_3 and X_4 and following the procedure given in detail in Nold et al. (2015) we arrive at the ansatz function

$$\Psi(x,y,t) = \Phi(Re\,y + t)\,e^{Re\,\omega\,e^{\frac{t}{Re}} + \alpha x + Re\,\alpha\,y}. \tag{3.74}$$

Evidently, the streamfunction would then be comprised of a traveling wave solution $\Phi(Re\,y+t)$ and an exponential part in which the temporal growth or decay due to ω is of double-exponential type. It is immediately apparent that the wave-type behavior is not consistent with the BC at the wall, as for $y = 0$ the time t remains as a variable. An attempt is made to instead introduce a generic set of homogeneous BC at negative and positive infinity. The solution satisfying these BC shall than be superposed to achieve an additional satisfaction of the wall BC.
A variable transformation of the form

$$\tilde{x} = x, \qquad \tilde{y} = Re\,y + t, \qquad \tilde{t} = t, \tag{3.75}$$

then gives

$$\Psi(\tilde{x},\tilde{y},\tilde{t}) = \Phi(\tilde{y})\,e^{Re\,\omega\,e^{\frac{\tilde{t}}{Re}} + \alpha\,\tilde{x} + \alpha\,(\tilde{y} - \tilde{t})}. \tag{3.76}$$

Substituting (3.76) into (3.72) indeed leads to a variable reduction and the ensuing ODE is then given as

$$(\omega\,e^{\frac{\tilde{y}}{Re}} - \alpha)\,\Phi''(\tilde{y}) + (2\,\alpha\,\omega\,e^{\frac{\tilde{y}}{Re}} - 2\,\alpha^2)\,\Phi'(\tilde{y}) + \left(\alpha^2\left(1 + \frac{1}{Re^2}\right)(1 + e^{\frac{\tilde{y}}{Re}}) - 1\right)\Phi(\tilde{y}) = 0. \tag{3.77}$$

This second order ODE can be solved in terms of Gaussian hypergeometric functions of the form

$$\begin{aligned}\Phi(\tilde{y}) = C_1 \Bigg[&\left(\alpha\, e^{\left(-\alpha+\frac{i}{Re}\sqrt{\alpha^2-1}\right)\tilde{y}} - \omega\, e^{\left(\frac{1}{Re}-\alpha+\frac{i}{Re}\sqrt{\alpha^2-1}\right)\tilde{y}} \right) \\ &{}_2F_1\left(\begin{matrix} 1+i(\alpha+\sqrt{\alpha^2-1}),\ 1+i(-\alpha+\sqrt{\alpha^2-1}) \\ 1+2i\sqrt{\alpha^2-1} \end{matrix}; \frac{\omega}{\alpha}\, e^{\frac{\tilde{y}}{Re}} \right) \Bigg] \\ + C_2 \Bigg[&\left(\alpha\, e^{\left(-\alpha-\frac{i}{Re}\sqrt{\alpha^2-1}\right)\tilde{y}} - \omega\, e^{\left(\frac{1}{Re}-\alpha-\frac{i}{Re}\sqrt{\alpha^2-1}\right)\tilde{y}} \right) \\ &{}_2F_1\left(\begin{matrix} 1+i(\alpha-\sqrt{\alpha^2-1}),\ 1+i(-\alpha-\sqrt{\alpha^2-1}) \\ 1-2i\sqrt{\alpha^2-1} \end{matrix}; \frac{\omega}{\alpha}\, e^{\frac{\tilde{y}}{Re}} \right) \Bigg]\end{aligned} \tag{3.78}$$

Demanding vanishing wall-normal velocity perturbations at positive infinity in the original variable space, i.e.

$$-\frac{\partial \Psi(x,y,t)}{\partial x}\bigg|_{y\to\infty} = -\left[\alpha\, \Phi(Re\, y + t)\, e^{Re\,\omega\, e^{\frac{t}{Re}} + \alpha x + Re\,\alpha\, y} \right]_{y\to\infty} = 0, \tag{3.79}$$

requires an expansion of (3.76) at large $\tilde{y} = Re\, y + t$. Asymptotic expansions of Gaussian hypergeometric functions are taken from Olver et al. (2010) in the case of large arguments. The rather lengthy calculations are omitted at this point for the sake of clarity whereupon BC (3.79) is expanded as

$$\begin{aligned}\frac{\partial \Psi(x,y,t)}{\partial x}\bigg|_{y\to\infty} = &C_1 \left(\frac{\omega_1}{\Gamma_1} e^{\left(-i\frac{Re}{\alpha}\right)\tilde{y}} - \frac{\omega_2}{\Gamma_2} e^{\left(i\frac{Re}{\alpha}\right)\tilde{y}} \right) \\ &+ C_2 \left(\frac{\omega_3}{\Gamma_3} e^{\left(-i\frac{Re}{\alpha}\right)\tilde{y}} - \frac{\omega_4}{\Gamma_4} e^{\left(i\frac{Re}{\alpha}\right)\tilde{y}} \right) = 0,\end{aligned} \tag{3.80}$$

where

$$\omega_1 = -\omega \left(\frac{\omega}{\alpha}\right)^{-(1+i(\sqrt{\alpha^2-1}+\alpha))}, \tag{3.81a}$$

$$\omega_2 = -\omega \left(\frac{\omega}{\alpha}\right)^{-(1+i(\sqrt{\alpha^2-1}-\alpha))}, \tag{3.81b}$$

$$\omega_3 = -\omega \left(\frac{\omega}{\alpha}\right)^{-(1+i(-\sqrt{\alpha^2-1}+\alpha))}, \tag{3.81c}$$

$$\omega_4 = -\omega \left(\frac{\omega}{\alpha}\right)^{-(1+i(-\sqrt{\alpha^2-1}-\alpha))}, \tag{3.81d}$$

and

$$\Gamma_1 = \Gamma(1+i(\sqrt{\alpha^2-1}-\alpha))\,\Gamma(i(\sqrt{\alpha^2-1}-\alpha)), \tag{3.82a}$$

$$\Gamma_2 = \Gamma(1+i(\sqrt{\alpha^2-1}+\alpha))\,\Gamma(i(\sqrt{\alpha^2-1}+\alpha)), \tag{3.82b}$$

$$\Gamma_3 = \Gamma(1+i(-\sqrt{\alpha^2-1}-\alpha))\,\Gamma(i(-\sqrt{\alpha^2-1}-\alpha)), \tag{3.82c}$$

$$\Gamma_4 = \Gamma(1+i(-\sqrt{\alpha^2-1}+\alpha))\,\Gamma(i(-\sqrt{\alpha^2-1}+\alpha)), \tag{3.82d}$$

with $\Gamma(z)$ denoting the gamma function.
The expanded BC (3.80) yields non-trivial solutions for C_1 and C_2 only if

$$\frac{\omega_1}{\Gamma_1}\frac{\omega_4}{\Gamma_4} - \frac{\omega_2}{\Gamma_2}\frac{\omega_3}{\Gamma_3} = 0. \tag{3.83}$$

Closer examination of (3.81) reveals that

$$\omega_1\,\omega_4 = \omega_2\,\omega_3, \tag{3.84}$$

so that (3.83) reduces to

$$\Gamma_1\,\Gamma_4 = \Gamma_2\,\Gamma_3. \tag{3.85}$$

Lastly, two identities of gamma functions are utilized:

$$\Gamma(z+1) = z\,\Gamma(z), \tag{3.86a}$$

$$\Gamma(i\,z)^2 = \frac{\pi}{y\sinh(\pi\,y)}, \tag{3.86b}$$

which employed into (3.85) yields

$$\frac{\sinh\left(\pi\,\left(-\sqrt{\alpha^2-1}-\alpha\right)\right)}{\sinh\left(\pi\,\left(\sqrt{\alpha^2-1}-\alpha\right)\right)} = \frac{\sinh\left(\pi\,\left(-\sqrt{\alpha^2-1}+\alpha\right)\right)}{\sinh\left(\pi\,\left(\sqrt{\alpha^2-1}+\alpha\right)\right)}, \tag{3.87}$$

which is satisfied only if

$$\alpha = \pm 1. \tag{3.88}$$

Obviously, this result is too restricting in the sense of a proper stability analysis, especially as no further information on the actual eigenvalue ω is encapsulated. Hence, further analysis of this ansatz is omitted and declared not expedient in the context of LSA.

Alternative exponential ansatz function

Upon utilization of all symmetries X_1 to X_4, a second new ansatz function occurs for the 2D inviscid ASBL given by

$$\Psi(x,y,t) = \varphi(y(1-\lambda)Re + t - \lambda x)\,e^{\alpha(Rey+x)}, \tag{3.89}$$

where α and Re denote the wave number in streamwise direction and the Reynolds number respectively, while λ consists of the group parameters generated in the Lie symmetry analysis. In analogy with the previous example, the variables are transformed to simplify the argument of the amplitude function so that

$$\tilde{x} = x \qquad \tilde{y} = y(1-\lambda)Re + t - \lambda x \qquad \tilde{t} = t, \tag{3.90}$$

trasnforms (3.89) to

$$\Psi(\tilde{x},\tilde{y},\tilde{t}) = \varphi(\tilde{y})\,e^{\alpha\frac{\tilde{y}-\tilde{t}+(1+\lambda)\tilde{x}}{(1-\lambda)Re}}. \tag{3.91}$$

Employing (3.91) into (3.72) and solving for $\varphi(\tilde{y})$ in the arising ODE gives

$$\varphi(\tilde{y}) = C_1\,e^{(\kappa_1+\kappa_2)\tilde{y}} + C_2\,e^{(\kappa_1-\kappa_2)\tilde{y}} + C_3\,e^{\frac{\alpha}{\lambda}\tilde{y}}, \tag{3.92}$$

where

$$\kappa_1 = \alpha\frac{(\lambda-1)Re^2+\lambda}{(\lambda-1)^2Re^2+\lambda^2}, \quad \kappa_2 = \frac{\sqrt{(Re^2+1)\lambda^2 - 2Re^2\lambda + (1-\alpha^2)Re^2}}{(\lambda-1)^2Re^2+\lambda^2}. \tag{3.93}$$

Employing (3.92) into (3.91) and transforming the variables back into the original coordinate system gives

$$\begin{aligned}\Psi(x,y,t) = {} & C_1\, e^{Re([1-\lambda](\kappa_1+\kappa_2)+\alpha)y}\, e^{(\alpha-\lambda(\kappa_1+\kappa_2))x}\, e^{(\kappa_1+\kappa_2)t} \\ & + C_2\, e^{Re([1-\lambda](\kappa_1-\kappa_2)+\alpha)y}\, e^{(\alpha-\lambda(\kappa_1-\kappa_2))x}\, e^{(\kappa_1-\kappa_2)t} \\ & + C_3\, e^{Re([1-\lambda]\frac{\alpha}{\lambda}+\alpha)y}\, e^{\frac{\alpha}{\lambda}t}.\end{aligned} \tag{3.94}$$

In order to analyze the BC at infinity, it is convenient to introduce parameter transformations of the form

$$\begin{aligned}\alpha - \lambda(\kappa_1+\kappa_2) &= i\alpha_1, \qquad & \kappa_1+\kappa_2 &= \beta_1 \\ \alpha - \lambda(\kappa_1-\kappa_2) &= i\alpha_2, \qquad & \kappa_1-\kappa_2 &= \beta_2,\end{aligned} \tag{3.95}$$

where α_1 and α_2 are assumed to be real. The remaining solution needs to be rejected as the dependence with respect to x is lost in the process of retransformation. Employing (3.95) into (3.94) then gives rise to

$$\Psi(x,y,t) = C_1\, e^{Re(\kappa_1+i\alpha_1)y}\, e^{i\alpha_1 x}\, e^{\kappa_1 t} + C_2\, e^{Re(\kappa_2+i\alpha_2)y}\, e^{i\alpha_2 x}\, e^{\kappa_2 t}. \tag{3.96}$$

Finally, the BC at infinity can be evaluated. We have

$$\begin{aligned}u(x,y\to\infty,t) = {} & \left.\frac{\partial\Psi(x,y,t)}{\partial y}\right|_{y\to\infty} \\ & = C_1\, Re(\kappa_1+i\alpha_1)\, e^{Re(\kappa_1+i\alpha_1)y}\, e^{i\alpha_1 x}\, e^{\kappa_1 t} \\ & + C_2\, Re(\kappa_2+i\alpha_2)\, e^{Re(\kappa_2+i\alpha_2)y}\, e^{i\alpha_2 x}\, e^{\kappa_2 t} = 0,\end{aligned} \tag{3.97}$$

and

$$\begin{aligned}v(x,y\to\infty,t) = {} & -\left.\frac{\partial\Psi(x,y,t)}{\partial x}\right|_{y\to\infty} \\ & = C_1\, i\alpha_1\, e^{Re(\kappa_1+i\alpha_1)y}\, e^{i\alpha_1 x}\, e^{\kappa_1 t} \\ & + C_2\, i\alpha_2\, e^{Re(\kappa_2+i\alpha_2)y}\, e^{i\alpha_2 x}\, e^{\kappa_2 t} = 0.\end{aligned} \tag{3.98}$$

The only way to satisfy both BC is to demand $\kappa_{1,r} < 0$ and $\kappa_{2,r} < 0$, after which immediately temporal decay can be concluded. Hence, temporal stability may be concluded for the alternative exponential ansatz function.

3.3 Spatial stability analysis of the asymptotic suction boundary layer

Analytical studies of the spatial stability problem for the ASBL are surprisingly scarce. The aforementioned studies of Fransson and Alfredsson (2003) are primarily experimental and numerical. Several questions regarding the spatial 2D and 3D development of linear modes for the ASBL remain unanswered until today. This section therefore aims to examine the spatial stability problem classically via computation of the spatial TS modes. The emerging spatial stability map gives a clearer picture on how spatial amplification rates scale with the Reynolds number and the wave frequency. Analogous to section 3.2.1, the spatial continuous spectra for

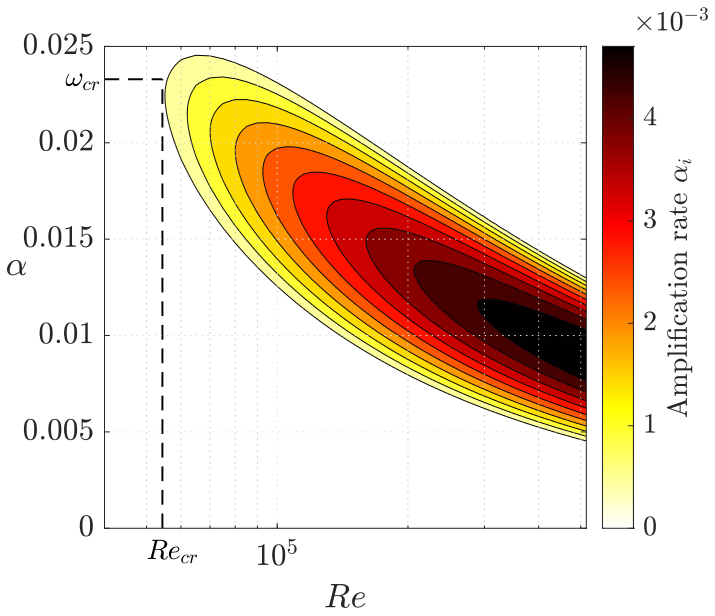

Figure 3.12: 2D spatial stability map with spatial amplification rate α_i plotted semilogarithmically with $4.0 \times 10^4 \leq Re \leq 5.0 \times 10^5$. Blank areas describe linearly stable modes. The critical triplet is given in (3.64c).

the ASBL are derived, which aims to yield bounded solutions for the eigenfunctions $\tilde{v}(y)$ at positive infinity. Surprisingly, due to the occurrence of quadratic α_i in the ensuing BC $v(y \to \infty)$ bounded, two solution branches occur for the spatial amplification rate. Furthermore, it turns out that one of the branches may provide continuous modes with $\alpha_i < 0$, leading to growth in the streamwise direction and thus giving rise a new class of unstable spatial eigenvalues. To the knowledge of the present author, spatial continuous modes were not correctly derived in previous works on the ASBL.

3.3.1 Computation of the spatial Tollmien-Schlichting modes of the asymptotic suction boundary

The methodology of computing spatial eigenvalues of the algebraic EVP (3.54) is analogous to the temporal computations, which is why for the methods employed the reader is referred to section 3.2. Figure 3.12 shows the stability map computed from $Re_{min} = 4.0 \times 10^4$ to $Re_{max} = 5.0 \times 10^5$ and from $\omega_{min} = 0.001$ to $\omega_{max} = 0.025$. The colored area illustrates the unstable TS modes whereas the blank areas are regions of stability. The upper limit of ω was chosen such that the uppermost unstable point of the stability map is included in the figure. When comparing the map with the spatial BBL (see e.g. Mack (1984)) similarities are striking, with a major difference being the critical Reynolds number $Re_{cr} = 54378.62032$, which is two orders of magnitude larger than for the BBL, for which Fransson and Alfredsson (2003) give $Re_{cr,BBL} = 518.7$. For the limit $Re \to \infty$ it appears that both the upper and lower branch of neutral stability decline towards lower ω. An asymptotic expansion for large Re is difficult to conduct as for this case not only the argument of the ${}_2F_3$-functions in (2.60) diverge but also the parameters. Expanding a generalized hypergeometric functions asymptotically with this

premise was attempted by Baldwin (1970) for the viscous ASBL, but the ensuing expansion is hardly utilisable and comprehensible. The critical triple was previously given in (3.64c).

3.3.2 Continuous spatial linear modes

In analogy to the continuous modes derived in the temporal case, spatially developing continuous modes are derived in this section for the ASBL. Again, the viscous parameter σ given in (3.26b) must be split into real and imaginary part giving

$$\sigma = \sqrt{s + i\, s_r} = \pm(\sigma_r + i\, \sigma_i), \tag{3.99}$$

with

$$s_r = 4\alpha_r^2 + 4\beta^2 - 4\alpha_i^2 + 1 - 4Re\alpha_i, \tag{3.100a}$$
$$s_i = 8\alpha_r\alpha i + 4Re\alpha_r - 4Re\omega, \tag{3.100b}$$

so that

$$\sigma_r = \frac{1}{\sqrt{2}}\sqrt{\sqrt{s_r^2 + s_i^2} + s_r}, \tag{3.101a}$$
$$\sigma_i = \mathrm{sgn}(s_i)\frac{1}{\sqrt{2}}\sqrt{\sqrt{s_r^2 + s_i^2} - s_r}. \tag{3.101b}$$

Due to the aforementioned reflection symmetry in σ, it is sufficient to only consider the plus sign in (3.99). The relaxed BC (3.43) for the ASBL once again reads

$$\sigma_r - 1 = 0. \tag{3.102}$$

Now, employing (3.101a) into (3.102) gives the parameter equation

$$\frac{1}{\sqrt{2}}\sqrt{\sqrt{s_r^2 + s_i^2} + s_r} = 1, \tag{3.103}$$

which needs to be satisfied to yield bounded amplitudes $\tilde{v}(y \to \infty)$. As spatial stability is examined, (3.103) is correspondingly solved for $\alpha_i(\alpha_r, \beta, \omega, Re)$. Doing so yields a quadratic equation of the form

$$\underbrace{\left(4\alpha_r^2 - 1\right)}_{a_2}\alpha_i^2 + \underbrace{Re\left(4\alpha_r^2 - 4\omega\alpha_r - 1\right)}_{a_1}\alpha_i + \underbrace{\alpha_r^2 + Re^2\left(\alpha_r - \omega\right)^2 + \beta^2}_{a_0} = 0, \tag{3.104}$$

which gives the solution pair

$$\alpha_{i,[+,-]} = \frac{1}{2a_2}\left(-a_1 \pm \sqrt{a_1^2 - 4a_2a_0}\right). \tag{3.105}$$

This result in itself is quite remarkable, as it implies a duality in α_i for every given parameter set $\{\alpha_r, \beta, \omega, Re\}$. The interesting cases are surely those where $\alpha_i < 0$, which re-employed into the NMA (2.54) would lead to growth of the continuous modes in streamwise direction. As can be taken from (3.105), the sign of α_i depends on the sign of a_2, which in turn solely depends on α_r as well as the sum or difference inside the bracket. Notice that $a_0 > 0$ regardless of which parameters are chosen as every term is quadratic. Also, for sufficiently large Re the absolute values for $\alpha_{i,[+,-]}$ take a minimum for $\alpha_r = \omega$, as then the term scaling with Re^2 in a_0 disappears. In the following, the three cases $\alpha_r < 1/2$, $\alpha_r = 1/2$ and $\alpha_r > 1/2$ are examined due to their implications for the sign of a_2.

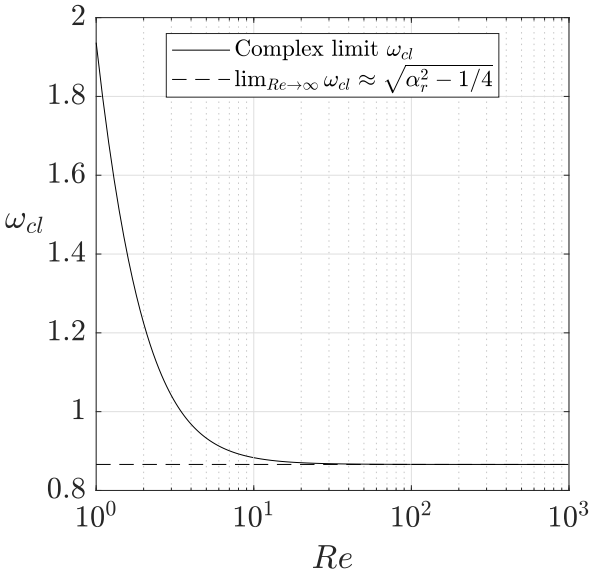

Figure 3.13: The complex limit ω_{cl}, below which α_i yields complex values and thus no continuous modes exist, is plotted for $\alpha_{cr} = 1$ and various orders of Re. The asymptotics for large Re as given in (3.111) is visualized in dashed lines.

Case 1: $\alpha_r < \frac{1}{2}$

The first case to be considered is $\alpha_r < \frac{1}{2}$, which leads to $a_2 < 0$. Since $a_0 > 0$, it can be followed that $\sqrt{a_1^2 - 4a_2a_0} > |a_1|$. Additionally, as $\omega > 0$, the linear coefficient $a_1 < 0$. The condition for $\alpha_i < 0$ therefore is

$$\alpha_{i,[+,-]} < 0 \qquad \rightarrow \qquad |a_1| \pm \sqrt{a_1^2 - 4a_2a_0} > 0. \tag{3.106}$$

As the root is larger than a_1, only the plus sign needs to be considered. Therefore, since both addends in (3.106) are larger than zero, the solution $\alpha_{i,+}$ is always negative, i.e.

$$\alpha_{i,+} = \frac{1}{2a_2}\left(-a_1 + \sqrt{a_1^2 - 4a_2a_0}\right) < 0. \tag{3.107}$$

As a result, this case reveals a set of unstable spatial 3D continuous modes. Substituting (3.107) into (3.102) will reveal that indeed $\sigma_r = 1$ applies for this case, thus meeting the condition of boundedness at infinity. An exemplary amplification map is shown in figure 3.14 for $\alpha_r = 0.1$ and $\beta = 0$. It clearly becomes visible how the solution set $\alpha_{i,+}$ is purely negative and thus unstable with (2.54) whereas $\alpha_{i,-}$ is without exception positive and therefore stable. The most unstable $\alpha_{i,+}$, shown in figure 3.14a, occur in those cases where both Re and ω are large, while the least unstable modes are to be found for low Re. On the other hand, the least stable $\alpha_{i,-}$ in figure 3.14b take a clear minimum at $\omega = \alpha_r = 0.1$, which corresponds to the least stable modes. Likewise, there is a tendency for the modes to get more stable the larger Re and ω are.

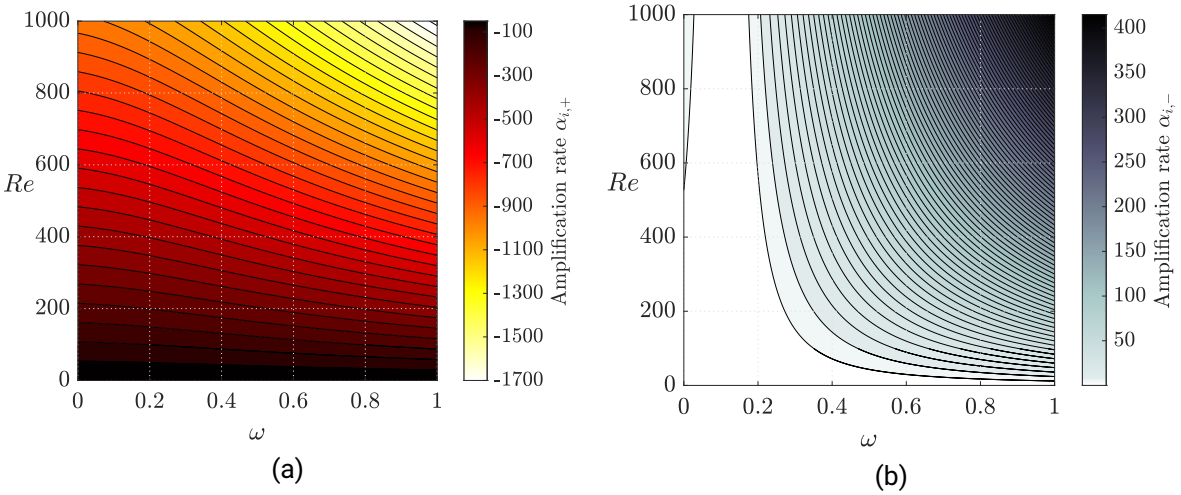

Figure 3.14: The 2D amplification map ($\beta = 0$) for (a) the positive solution $\alpha_{i,+}$ and (b) the negative solution $\alpha_{i,-}$ is plotted vs ω and Re with $\alpha_r = 0.1$. The lines indicate isolevels of amplification. All positive solutions are amplified while the negative solutions are damped. A minimum in α_i is clearly visible at $\omega = \alpha_r = 0.1$.

Case 2: $\alpha_r = \frac{1}{2}$

This case is rather trivial, as the quadratic equation (3.104) degenerates into a linear equation for $a_2 = 0$, leading to

$$\alpha_i = -\frac{a_0}{a_1}. \tag{3.108}$$

It can easily be seen from (3.104) that $a_1 < 0$ and $a_0 > 0$ regardless of the parameters a_r, β, ω and Re. Therefore, in this case all existing continuous modes are positive and stable.

Case 3: $\alpha_r > \frac{1}{2}$

The last case to be analyzed is the one producing $a_2 > 0$. Now, the sign of a_1 depends on the chosen ω. Moreover, since the term $4a_2a_0$ in (3.105) is now always positive, certain parameter combinations may lead to the radicand being negative, whereupon complex α_i would emerge, which clearly contradicts the assumption that $\alpha_i \in \mathbb{R}$. The condition to yield a negative radicand is

$$a_1^2 - 4a_2a_0 < 0. \tag{3.109}$$

which lets a condition arise for ω, namely

$$\omega < \sqrt{\alpha_r^2 + \frac{4\alpha_r^4}{Re^2} - \frac{\alpha_r^2}{Re^2} - \frac{1}{4}} = \omega_{cl}, \tag{3.110}$$

where the r.h.s. is the limit ω_{cl} below which α_i takes complex values. For $Re \to \infty$ this expression simplifies to

$$\lim_{Re\to\infty} \omega_{cl} = \sqrt{\alpha_r^2 - \frac{1}{4}}. \tag{3.111}$$

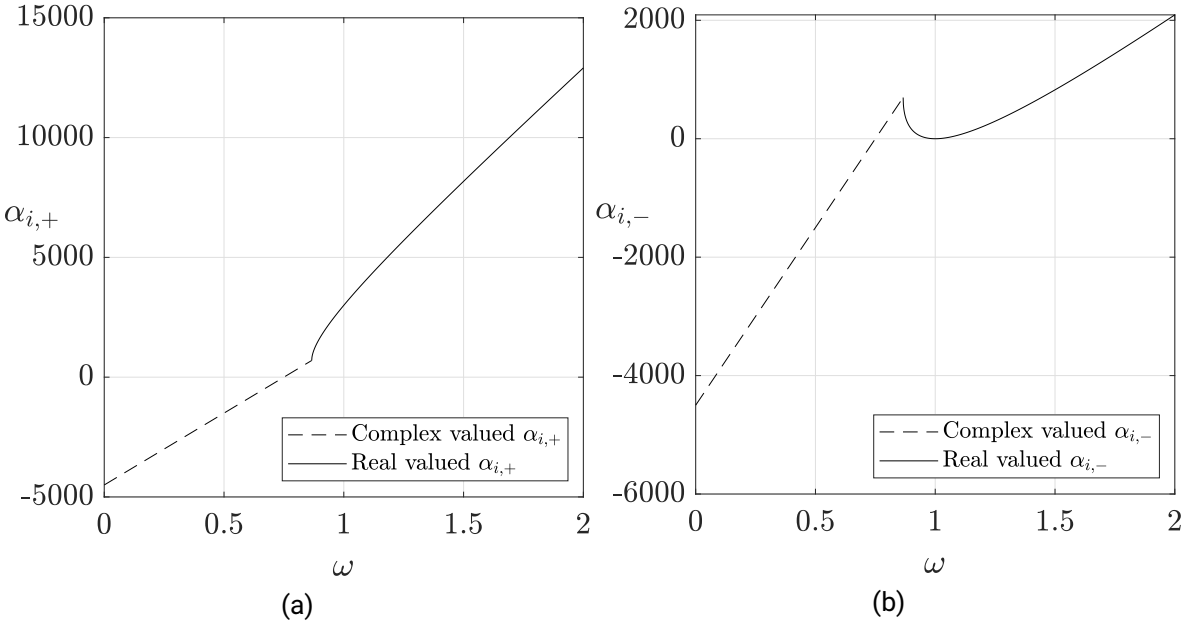

Figure 3.15: The spatial growth rate α_i plotted for (a) its positive solution and (b) its negative solution according to (3.105) for $\alpha_r = 1$ and $Re = 1000$. As can be seen, α_i adopts complex values for $\omega \lessapprox 0.866$, which is the value arising for the threshold in (3.110). Above this thresholds α_i is purely positive with a global minimum for $\alpha_{i,-}$ at $\omega = \alpha_r = 1$.

This complex limit ω_{cl} and its large Reynolds number asymptotic is visualized for $\alpha_{cr} = 1$ in figure 3.13. For sufficiently large Re this condition simplifies to

$$\omega \lessapprox \sqrt{\alpha_r^2 - \frac{1}{4}}. \tag{3.112}$$

If this condition is satisfied, α_i is complex. This implies that in this parameter region no continuous modes exist capable of satisfying the relaxed BC (3.43), i.e. $\sigma_r = 1$. However, there still exist the classical linear modes presented in the previous section. And yet, it is interesting that there are certain parameter combination for which only classical linear modes and no continuous modes exist.
What still remains is the question whether for the case $\alpha_r > \frac{1}{2}$ unstable spatial modes may be obtained. The corresponding condition is

$$-a_1 + \sqrt{a_1^2 - 4a_2a_0} < 0. \tag{3.113}$$

First, the sign of a_1 needs to be clarified. As $a_2 > 0$ and $\sqrt{a_1^2 - 4a_2a_0} < |a_1|$ due to $a_0 > 0$, a negative a_i may only arise if $a_1 > 0$. This means for ω that

$$\omega < \alpha_r - \frac{1}{4\alpha_r}, \tag{3.114}$$

while simultaneously in order for α_i to stay real

$$\omega \geq \sqrt{\frac{4\alpha_r^4}{Re^2} + \alpha_r^2\left(1 - \frac{1}{Re^2}\right) - \frac{1}{4}}, \tag{3.115}$$

has to apply. However, it can be shown that the expression on the r.h.s. of (3.114) is always smaller than the r.h.s. of (3.115) regardless of Re, thus making it impossible for both conditions to apply simultaneously. Thus, only for the cases where $\alpha_r < 1/2$ may unstable modes possibly arise. Figure 3.15 shows an exemplary visualization for purely stable spatial continuous modes at $\alpha_r = 1$.

Due to the relaxed BC (3.43), the eigenfunctions for the spatial continuous modes are different than the ones for the classical linear modes as the sub-solution $\tilde{v}_3(y)$ in (3.24) is retained. In order to obtain a specific eigenfunction, it is necessary to specify (3.43) so that the solution at infinity takes a specific, albeit oscillating, value. For the sake of simplicity, the BC is set as

$$\tilde{v}(y \to \infty) = 1, \tag{3.116}$$

which together with the wall BC $\tilde{v}(y=0) = \mathrm{D}\tilde{v}(y=0) = 0$ complements the BC set necessary to obtain the eigenfunction $\tilde{v}(y)$. The result is given by

$$\begin{aligned}\tilde{v}(y) = C_3 \Bigg[& e^{-ky}\, {}_2F_3\left(\begin{matrix}\boldsymbol{a_2}\\ \boldsymbol{b_2}\end{matrix}; -iRe\,\alpha e^{-y}\right)\left(\frac{{}_2F_3\left(\begin{matrix}\boldsymbol{a_4}\\ \boldsymbol{b_4}\end{matrix}; -iRe\,\alpha\right)}{{}_2F_3\left(\begin{matrix}\boldsymbol{a_2}\\ \boldsymbol{b_2}\end{matrix}; -iRe\,\alpha\right)}\frac{\rho_1}{\rho_2} - \frac{{}_2F_3\left(\begin{matrix}\boldsymbol{a_3}\\ \boldsymbol{b_3}\end{matrix}; -iRe\,\alpha\right)}{{}_2F_3\left(\begin{matrix}\boldsymbol{a_2}\\ \boldsymbol{b_2}\end{matrix}; -iRe\,\alpha\right)}\right) \\ & + e^{\frac{\sigma-1}{2}y}\, {}_2F_3\left(\begin{matrix}\boldsymbol{a_3}\\ \boldsymbol{b_3}\end{matrix}; -iRe\,\alpha e^{-y}\right) + e^{-\frac{\sigma+1}{2}y}\, {}_2F_3\left(\begin{matrix}\boldsymbol{a_4}\\ \boldsymbol{b_4}\end{matrix}; -iRe\,\alpha e^{-y}\right)\frac{\rho_1}{\rho_2}\Bigg],\end{aligned} \tag{3.117}$$

where the parameter vectors $\boldsymbol{a_i}$ and $\boldsymbol{b_i}$ are defined in (3.25) and ρ_1 and ρ_2 are constants comprised of generalized hypergeometric functions given as

$$\begin{aligned}\rho_1 = {} & \frac{\overline{a_3}}{\overline{b_3}} iRe\alpha\, {}_2F_3\left(\begin{matrix}\boldsymbol{a_3}+\boldsymbol{1}\\ \boldsymbol{b_3}+\boldsymbol{1}\end{matrix}; -iRe\,\alpha\right) + \frac{\sigma-1}{2}\, {}_2F_3\left(\begin{matrix}\boldsymbol{a_3}\\ \boldsymbol{b_3}\end{matrix}; -iRe\,\alpha\right) \\ & - \frac{\overline{a_2}}{\overline{b_2}} iRe\alpha \frac{{}_2F_3\left(\begin{matrix}\boldsymbol{a_3}\\ \boldsymbol{b_3}\end{matrix}; -iRe\,\alpha\right)\, {}_2F_3\left(\begin{matrix}\boldsymbol{a_2}+\boldsymbol{1}\\ \boldsymbol{b_2}+\boldsymbol{1}\end{matrix}; -iRe\,\alpha\right)}{{}_2F_3\left(\begin{matrix}\boldsymbol{a_2}\\ \boldsymbol{b_2}\end{matrix}; -iRe\,\alpha\right)} + k\, {}_2F_3\left(\begin{matrix}\boldsymbol{a_3}\\ \boldsymbol{b_3}\end{matrix}; -iRe\,\alpha\right),\end{aligned} \tag{3.118a}$$

$$\begin{aligned}\rho_2 = {} & \frac{\overline{a_4}}{\overline{b_4}} iRe\alpha\, {}_2F_3\left(\begin{matrix}\boldsymbol{a_4}+\boldsymbol{1}\\ \boldsymbol{b_4}+\boldsymbol{1}\end{matrix}; -iRe\,\alpha\right) - \frac{\sigma+1}{2}\, {}_2F_3\left(\begin{matrix}\boldsymbol{a_3}\\ \boldsymbol{b_3}\end{matrix}; -iRe\,\alpha\right) \\ & - \frac{\overline{a_2}}{\overline{b_2}} iRe\alpha \frac{{}_2F_3\left(\begin{matrix}\boldsymbol{a_4}\\ \boldsymbol{b_4}\end{matrix}; -iRe\,\alpha\right)\, {}_2F_3\left(\begin{matrix}\boldsymbol{a_2}+\boldsymbol{1}\\ \boldsymbol{b_2}+\boldsymbol{1}\end{matrix}; -iRe\,\alpha\right)}{{}_2F_3\left(\begin{matrix}\boldsymbol{a_2}\\ \boldsymbol{b_2}\end{matrix}; -iRe\,\alpha\right)} + k\, {}_2F_3\left(\begin{matrix}\boldsymbol{a_4}\\ \boldsymbol{b_4}\end{matrix}; -iRe\,\alpha\right).\end{aligned} \tag{3.118b}$$

Admittedly, the eigenfunctions are formed by a quite long expression, for which it seems difficult to evaluate the numerous ${}_2F_3$ generalized hypergeometric functions in (3.117). However, owing to modern computer algebra systems, it is possible to evaluate such terms in reasonable computation times with sufficient resolution in wall-normal direction. The remaining constant C_3 must be chosen upon quantifying the relaxed BC (3.43) at infinity. Instead of demanding

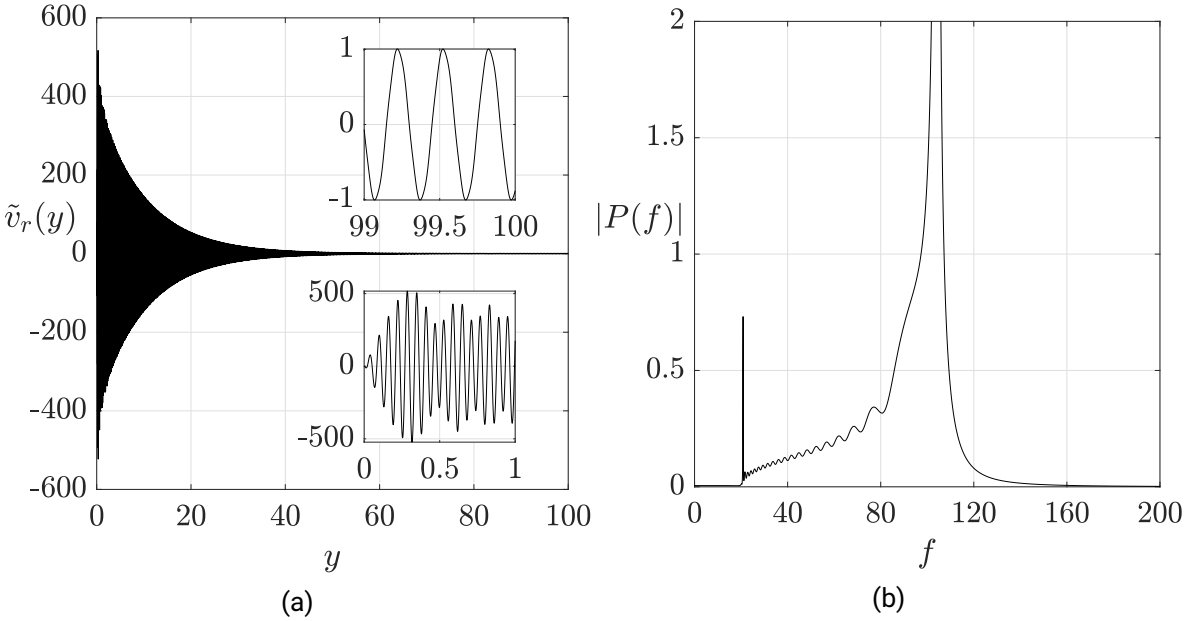

Figure 3.16: (a) Computation of the real part of the eigenfunction $\tilde{v}_r(y)$ as given in (3.117) for $Re = 100$ and $\alpha_r = \omega = 0.1$, which in figure 3.14b contributed to a maximum amplification rate α_i. Two window plots for the range $y \in [0, 1]$ and $y \in [99, 100]$ are displayed, respectively. (b) Single-sided power spectrum of the eigenfunction acquired from the fast Fourier transformation (FFT) of $\tilde{v}_r(y)$, where the amplitude $|P(f)|$ is plotted versus the wave numbers f. A local maximum corresponding to the wall-normal wave number k_y defined in (3.121) at $f \approx 20.8$ and a global maximum at $f \approx 104.2$ can be observed.

(3.117) merely to be bounded, one must instead assume a concrete value to be adapted at infinity, for instance

$$\tilde{v}(y \to \infty) = 1, \tag{3.119}$$

which would give

$$C_3 = 1. \tag{3.120}$$

Strictly speaking though, (3.119) is not correct as σ is complex and therefore (3.117) expands towards

$$\tilde{v}(y \to \infty) \to C_3\, e^{ik_y y}, \tag{3.121}$$

where $k_y = \sigma_i/2$ denoting the wall-normal wave number defined with σ_i given in (3.101b). Thus, the eigenfunction $\tilde{v}(y)$ oscillates at infinity and (3.119) must be stated more precisely as

$$\max\left(\tilde{v}(y \to \infty)\right) = 1, \tag{3.122}$$

where instead the maximum of $\tilde{v}(y)$ at infinity is required to be unity. The constant C_3 for this case would adapt (3.120) nevertheless. An exemplary depiction of the wall-normal eigenfunction $\tilde{v}(y)$ corresponding to a spatial continuous mode with $\alpha = \omega = 0.1$ and $Re = 100$ may be referred to in figure 3.16a. As defined in (3.121), the wall-normal wave number k_y is half the imaginary part of the viscous parameter σ_i given in (3.101b), which scales with $O(\sqrt{Re})$. For the concrete parameters, the viscous parameter σ yields

$$\sigma(\alpha_r = \omega = 0.1, Re = 100) \approx 1 - 41.66671i, \quad \Rightarrow \quad k_y \approx 20.83336. \tag{3.123}$$

The wall-normal wavelength in turn reads

$$\lambda_y = \frac{2\pi}{k_y} \approx 0.30159. \tag{3.124}$$

Considering the upper window plot in figure 3.16a, which shows the eigenfunction at large distances from the wall with $y \in [99, 100]$, the wavelength qualitatively corresponds to (3.124). Moreover, the amplitude is correctly adapting to the demanded amplitude induced by $C_3 = 1$. In the near wall region $y \in [0, 1]$ one discerns a more diverse oscillation with superposed wave elements of high and low wave numbers. A wave number analysis obtained via FFT is given in figure 3.16b, where the amplitude $|P(f)|$ scaled by the number of sample points $N = 1.0 \times 10^5$ is plotted vs the wave numbers f. The qualitative observations from figure 3.16a are now quantified. Evidently, the frequencies range from a minimal wave number equalling k_y as given in (3.123) to a maximum wave number of approximately $f \approx 160$. A second distinct, global maximum is located at $f \approx 104.2$. The wide range of wave numbers have their origin in the generalized hypergeometric functions given in the eigenfunction (3.117), which in the near wall region are at their maximum amplitude and thereof gradually decay in magnitude towards the free-stream. As was mentioned, the mode is selected such that maximal amplification is achieved. Concretely, the selected wave parameters employed into (3.107) gives

$$\alpha_{i,+} = -104.16677, \tag{3.125}$$

which corresponds to enormous growth rates in the streamwise direction. The streamwise wavelength in turn yields

$$\lambda_x = \frac{2\pi}{\alpha_r} \approx 62.83185, \tag{3.126}$$

i.e. considerable elongation in the streamwise direction. If such modes turn out to physically exist and indeed grow rapidly, they would surely evolve into large-scale streamwise structures. As was further claimed in section 3.2.1, the eigenfunctions emerging for continuous modes strongly resemble turbulent fluctuations in the free-stream, which similarly are manifold in their respective wall-normal wave numbers. As such, continuous modes of the ASBL provide an interesting physical model for FST, which in turn could shed new light on the transition process in view of free-stream induced transition in the ASBL (Yoshioka et al., 2004). A yet-to-be proven assumption is that even if the classical linear modes computed from (3.37) are stable, as is evidently the case for the considered Reynolds number $Re = 100$, the present spatial continuous modes could positively contribute to triggering transition in the flow. Whether this is actually the case is left for future numerical studies.

3.4 Conclusive remarks

The theory of linear stability was revisited for the temporal and spatial stability problem of the ASBL, representing a BL flow existing on a semi-infinite domain.
For the ASBL, the point was attempted to be made that although eigenvalue spectra may be obtained rather effortlessly via discretizing the mOSE with Chebyshev collocation schemes, several aspects of linear stability are neglected by not employing the known analytical solution. Asymptotic analysis, for instance, is made possible by the presence of analytical solution, which allows for insightful analyses of the underlying EVP with regard to its parameters. As is known

for other wall-bounded shear flows, in the infinite limit for streamwise wave numbers α, all modes are inevitably stable whereas small streamwise wave numbers curiously did not yield asymptotic solutions for the temporal eigenvalue ω. Instead it could be shown that only in the distinguished limit $Re_\alpha = Re\alpha$ with $Re \to \infty$, $\alpha \to 0$ and $Re = O(\alpha^{-1})$ asymptotic solutions exist for the eigenvalue ω. In fact, solutions are proved to only exist for $Re_\alpha > 0.84191$, which therefore provides a measure for the largest possible elongation in streamwise direction of perturbation velocities. It further was demonstrated that the distinguished limit via analysis of the OSE is in fact a common feature of wall-bounded shear flows in general. Previous numerical simulations by Hutchins and Marusic (2007), Khapko et al. (2016), and Ferro et al. (2021) on wall-bounded shear flows showed how in the near-wall region the pre-multiplied energy spectra have energy maxima at streamwise wave numbers of order $O(Re)$, which seems to be connected to the aforementioned distinguished limit. Thus, a remarkable link was established in this chapter between linear modes in the laminar base state and large-scale streamwise structures in turbulent flows.

In addition, a thorough linear and spatial stability analysis was conducted for the ASBL, resulting in detailed stability maps for both cases. The temporal stability map revealed a region of maximal amplification at $Re \approx 5.0 \times 10^5$. The critical triplet $\{\alpha_{cr}, \omega_{cr}, Re_{cr}\}$ could be computed to five significant digits. This represents a genuine advantage of analytical solutions over discrete methods as the critical Reynolds number can be computed up to arbitrary accuracies simply by increasing the number of digits in the employed solver. Previously in the literature, the critical Reynolds number was given as $Re_{cr} = 54382$ by Fransson and Alfredsson (2003), who employed Chebyshev collocation schemes. This value was significantly improved to $Re_{cr} = 54378.62032$ in the present chapter.

Another invaluable benefit of analytical solutions is the possibility of filtering discrete temporal and spatial spectra, where the spurious modes employed as initial guesses into the non-linear root solver of the analytical EVP are quickly identified as false solutions. The result are corrected temporal and spatial spectra, including only those modes which actually represent physical solutions. The analysis of the respective wall-normal eigenfunctions $\tilde{v}(y)$ of four different modes for Re_{cr} and α_{cr} showed how the eigenfunctions increasingly oscillate in wall-normal direction the further away modes are from the most critical TS mode in the ω_r-ω_i-spectra.

Furthermore, a measure for the persistence of perturbations in wall-normal direction was derived, i.e. the WDRL δ_σ defined as the inverse of the wall-normal wave number. It turns out that the viscous parts of the eigenfunction persist furthest into the far field in aforementioned distinguished limit Re_α. Thus, the distinguished limit not only provides an upper bound for the elongation in streamwise direction for large Reynolds numbers but also modes parametrized in the distinguished limit Re_α also have the largest WDRL $\delta_{\sigma,max} = 2$, equal to twice the displacement thickness δ_1. These modes therefore resemble superstructures, which were initially characterized to have length scales in the order of the characteristic length of the flow problem, which for the ASBL is given as δ_1.

Furthermore, novel symmetry-induced ansatz functions were examined for the inviscid stability problem of the ASBL, based on seminal works by Nold and Oberlack (2013), Nold et al. (2015), and Mirzayev (2016). In addition to the NMA, a double-exponential ansatz function and alternative exponential ansatz function arises for the ASBL. Due to their travelling wave character in the x-y-plane, the classical BC at the wall cannot be satisfied. The attempt was made to introduce an artificial BC at negative infinity instead. Unfortunately, this BC proved to be too restrictive on the solutions of the reduced ODE. Further research in this direction is motivated as the employed BC surely can and should be improved upon.

Lastly, temporal and continuous spectra for derived for the ASBL. The more interesting case was given by the continuous spatial modes, which revealed a solution branching for which the positive branch gave rise to unstable modes when $\alpha_r < 0.5$. The maximum amplification rates α_i for these cases are adopted for $\alpha_r = \omega$, regardless of Re. One such continuous mode was visualized for $\alpha = \omega = 0.1$, which is characterized by small wall-normal wavelengths of the eigenfunction $\tilde{v}(y)$ as well as the presence of multiple wave numbers in wall-normal direction. The corresponding signal is reminiscent of turbulent fluctuations in FST and could therefore prove to be a useful physical model for investigating FST induced bypass transition. The actual existence of these modes as well as their implications for bypass transition is left for future studies.

4 Destabilization of plane Couette flow via wall-normal constant transpiration

The following section is based on an unpublished manuscript by Sun et al. (2022) I co-authored, which in turn is derived from a master thesis I supervised written by Sun (2020). The linear stability analysis (LSA) of the plane Couette flow with transpiration (PCFT) was conducted with the same methods employed in the previous chapter for the asymptotic suction boundary layer (ASBL). The results of the stability analysis are elaborated in a joint effort, where specifically the computation of eigenvalues was conducted by Weihang Sun based on Maple scripts written and provided by me as well as on open source collocation schemes by Schmid et al. (2002). The transformation of PCFT to the ASBL was solely elaborated by me.

In the field of hydrodynamic stability it is well-known that classical linear stability theory (LST) fails to correctly predict laminar-turbulent transition in wall-bounded shear flows. It was discovered by Orszag and Kells (1980) that plane Couette flow (PCF) transitions in the presence of finite-amplitude disturbances despite PCF being linearly stable both in two-dimensional (2D) and three-dimensional (3D).
As indicated, LST fails for PCF and, furthermore, it exhibits linear stability for any Reynolds number (Romanov, 1973). This, however, is in stark contrast to the fact that transition occurs in direct numerical simulation (DNS) at Reynolds numbers of order $Re = O(10^3)$ (Orszag and Kells, 1980), which was further specified to a Reynolds number of $Re \approx 375$, at which turbulent spots can be sustained, in DNS performed by Lundbladh and Johansson (1991). In the numerical work of Orszag and Kells (1980), it is further discovered that 3D finite-amplitude disturbances are responsible for transition to turbulence whereas no 2D finite-amplitude disturbances occurred in the corresponding DNS. Nagata (1990) further found a lower bound at $Re = 125$ for the existence of turbulence driving 3D finite-amplitude disturbance, below which instability may not occur. Transition to turbulence of PCF was experimentally studied by Tillmark and Alfredsson (1992) and Daviaud et al. (1992), who found transition to occur at $Re \approx 360$ and $Re \approx 370$ respectively, which is close to the numerically determined transitional Reynolds number. What remained was an in-depth description of the transitional process and the corresponding formation of patterns.
Now, non-modal stability analysis has contributed greatly to understanding the phenomenon of transition due to transient growth arising from non-orthogonal eigenfunctions for PCF, which is thoroughly discussed by Trefethen et al. (1993). The success of non-modal stability theory by no means implies, however, that modal LST is exhausted entirely. In fact, it is one of the key results in this chapter that the presence of transpiration destabilizes PCF and for large enough transpiration rates leads to instabilities. It was shown by Floryan (2003) how in laminar PCF with sinusoidal transpiration at the lower wall large-scale streamwise vortices arise. They further reported that the threshold amplitude of transpiration needed for onset scales with

$Re^{-1.15}$. Thus, transpiration seemingly destabilizes PCF in contrast to stabilization via suction in boundary layers. The destabilizing nature of transpiration on certain wall-bounded shear flows is not new and has, for instance, been reported for Taylor-Couette flow by Gallet et al. (2010). A more generalized view of destabilization via wall permeability in channel flows is further discussed by Tilton and Cortelezzi (2006). The present chapter extends these results to PCF.
As for the numerical investigation of PCFT, a DNS was conducted by Kraheberger et al. (2018), who discovered that characteristic turbulent stationary rolls known to exist in classical PCF are maintained in the present of transpiration and move towards the wall where suction is exhibited.
In section 4.1, the governing stability equations for PCFT are established. Incidentally, a remarkable transformation from PCFT to the ASBL when assuming infinitely large transpiration rates is derived in section 4.2. Then, in section 4.3 in analogy to the stability analysis of the ASBL in chapter 3 a classical LSA is presented for varying transpiration rates and Reynolds numbers both for the temporal and spatial stability problem. Finally, discrete spectra and eigenfunctions are examined for PCFT and presented in 4.4.

4.1 Governing stability equations for plane Couette flow with transpiration

The base flow discussed in this chapter is the 2D PCF, i.e. a lower stationary wall with $U(0) = 0$ and an upper wall moving at constant velocity with $U(y) = U_w$, where both walls are parallel at a distance h. Additionally, constant transpiration moving in positive wall-normal direction y is assumed, yielding $V = V_0$ in the entire field. Before actually deriving the laminar base state, the dimensionless Navier–Stokes equations (NSE) are acquired by performing non-dimensionalization as defined in (2.29). In contrast to the ASBL, two independent Reynolds numbers must be defined, representing both velocity scales U_w and V_0, respectively, which gives

$$Re = \frac{U_w h}{\nu}, \quad Re_V = \frac{V_0 h}{\nu}, \tag{4.1}$$

where Re is the classical Reynolds number and Re_V denotes the transpiration Reynolds number, which is a non-dimensional number representing the transpiration rate. Solving the NSE (2.28) after non-dimensionalization gives the non-dimensional laminar base profile

$$U(y) = \frac{e^{Re_V y} - 1}{e^{Re_V} - 1}, \quad V(y) = \frac{Re_V}{Re}, \tag{4.2}$$

where the wall-normal coordinate has additionally been non-dimensionalized by the wall-distance h. Figure 4.1 depicts the velocity profile corresponding to (4.2) for varying Re_V. For increasingly large transpiration Reynolds numbers Re_V, a boundary layer (BL) effect is observed, squeezing the profile towards the upper wall. This BL effect becomes relevant for the distribution of collocation points for the Chebyshev collocation schema employed in section 4.3. In analogy to the LSA presented in chapter 3, a normal mode ansatz (NMA) is assumed for the 2D PCFT with $\beta = 0$, which is given by

$$v(x, y, t) = \tilde{v}(y)\, e^{i(\alpha x - \omega t)}. \tag{4.3}$$

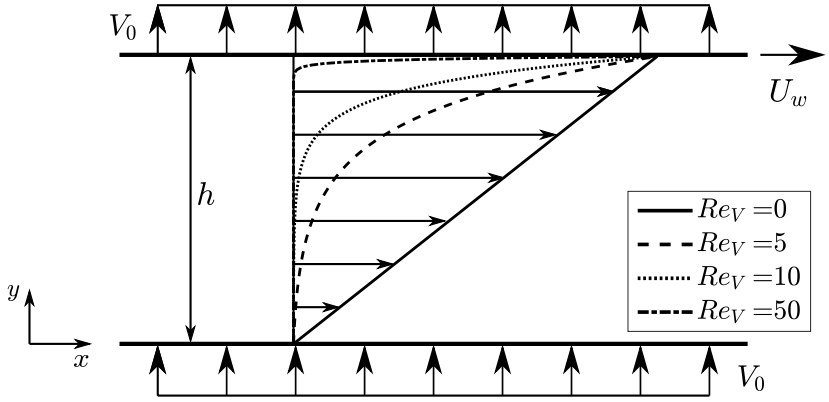

Figure 4.1: The non-dimensional velocity profile of PCF with wall-transpiration rates from $Re_V = 0$ (classical PCF) to $Re_V = 50$. (adapted from Sun et al. (2022))

The derivation of the modified Orr–Sommerfeld equation (mOSE) for PCFT is conducted in analogy to section 2.4.2. With (4.3) the mOSE for PCFT resultantly reads

$$\left[\left(-i\omega + i\alpha U(y) + \frac{Re_V}{Re}\mathrm{D}\right)\left(\mathrm{D}^2 - \alpha^2\right) - i\alpha \mathrm{D}^2 U(y) - \frac{1}{Re}\left(\mathrm{D}^2 - \alpha^2\right)^2\right]\tilde{v}(y) = 0, \tag{4.4}$$

where D denotes the derivative with respect to y. Each boundary condition (BC) at both walls, respectively, is correspondingly given by

$$\tilde{v}(y=0) = 0, \qquad \mathrm{D}\tilde{v}(y)|_{y=0} = 0, \tag{4.5a}$$

$$\tilde{v}(y=1) = 0, \qquad \mathrm{D}\tilde{v}(y)|_{y=1} = 0. \tag{4.5b}$$

Analogous to the mOSE of the ASBL (3.17), the solution of (4.4) is based on ${}_2F_3$ generalized hypergeometric functions equivalent to (3.24) of the form

$$\begin{aligned}\tilde{v}(y) = {} & C_1\, e^{\alpha y}\, {}_2F_3\left(\begin{matrix}\mathbf{a_1}\\ \mathbf{b_1}\end{matrix}; z(y)\right) + C_2\, e^{-\alpha y}\, {}_2F_3\left(\begin{matrix}\mathbf{a_2}\\ \mathbf{b_2}\end{matrix}; z(y)\right) \\ & + C_3\, e^{Re_V \frac{1-\sigma}{2} y}\, {}_2F_3\left(\begin{matrix}\mathbf{a_3}\\ \mathbf{b_3}\end{matrix}; z(y)\right) + C_4\, e^{Re_V \frac{1+\sigma}{2} y}\, {}_2F_3\left(\begin{matrix}\mathbf{a_4}\\ \mathbf{b_4}\end{matrix}; z(y)\right),\end{aligned} \tag{4.6}$$

where the viscous parameter σ and $z(y)$ read

$$\sigma = \frac{\sqrt{(Re_V^2 + 4\alpha^2)(e^{Re_V} - 1) + 4i(-\alpha + \omega - \omega e^{Re_V})Re}}{Re_V \sqrt{e^{Re_V} - 1}}, \tag{4.7a}$$

$$z(y) = \frac{i\alpha Re e^{Re_V y}}{Re_V^2\left(e^{Re_V} - 1\right)}. \tag{4.7b}$$

The parameters of the generalized hypergeometric functions a_{ij} and b_{ij} in turn are given by

$$\begin{aligned}&\mathbf{a_1} = \begin{bmatrix}-\kappa + \tilde{\alpha}\\ \kappa + \tilde{\alpha}\end{bmatrix}, \quad \mathbf{a_2} = \begin{bmatrix}-\kappa - \tilde{\alpha}\\ \kappa - \tilde{\alpha}\end{bmatrix}, \quad \mathbf{a_3} = \begin{bmatrix}\frac{1-\sigma}{2} - \kappa\\ \frac{1-\sigma}{2} + \kappa\end{bmatrix}, \quad \mathbf{a_4} = \begin{bmatrix}\frac{1+\sigma}{2} + \kappa\\ \frac{1+\sigma}{2} - \kappa\end{bmatrix}; \\ &\mathbf{b_1} = \begin{bmatrix}1 + 2\tilde{\alpha}\\ \frac{1+2\tilde{\alpha}+\sigma}{2}\\ \frac{1+2\tilde{\alpha}-\sigma}{2}\end{bmatrix}, \mathbf{b_2} = \begin{bmatrix}1 - 2\tilde{\alpha}\\ \frac{1-2\tilde{\alpha}-\sigma}{2}\\ \frac{1-2\tilde{\alpha}+\sigma}{2}\end{bmatrix}, \mathbf{b_3} = \begin{bmatrix}1 - \sigma\\ \frac{3+2\tilde{\alpha}-\sigma}{2}\\ \frac{3-2\tilde{\alpha}-\sigma}{2}\end{bmatrix}, \mathbf{b_4} = \begin{bmatrix}1 + \sigma\\ \frac{3+2\tilde{\alpha}+\sigma}{2}\\ \frac{3-2\tilde{\alpha}+\sigma}{2}\end{bmatrix},\end{aligned} \tag{4.8}$$

with $\tilde{\alpha} = \alpha/Re_V$ and $\kappa = \sqrt{\tilde{\alpha}^2 + 1}$. The derivative of $\tilde{v}(y)$ later evaluated at $y = 0$ and $y = 1$ in (4.5) is given by

$$\begin{aligned}\frac{\mathrm{d}\tilde{v}(y)}{\mathrm{d}y} = {} & C_1 \left[\alpha\, {}_2F_3\left(\begin{matrix}\mathbf{a_1}\\ \mathbf{b_1}\end{matrix}; z(y)\right) + Re_V z(y) \frac{\overline{a}_1}{\overline{b}_1} {}_2F_3\left(\begin{matrix}\mathbf{a_1}+\mathbf{1}\\ \mathbf{b_1}+\mathbf{1}\end{matrix}; z(y)\right)\right] \\ & + C_2 \left[-\alpha\, {}_2F_3\left(\begin{matrix}\mathbf{a_2}\\ \mathbf{b_2}\end{matrix}; z(y)\right) + Re_V z(y) \frac{\overline{a}_2}{\overline{b}_2} {}_2F_3\left(\begin{matrix}\mathbf{a_2}+\mathbf{1}\\ \mathbf{b_2}+\mathbf{1}\end{matrix}; z(y)\right)\right] \\ & + C_3 Re_V \left[\frac{1-\sigma}{2} {}_2F_3\left(\begin{matrix}\mathbf{a_3}\\ \mathbf{b_3}\end{matrix}; z(y)\right) + z(y) \frac{\overline{a}_3}{\overline{b}_3} {}_2F_3\left(\begin{matrix}\mathbf{a_3}+\mathbf{1}\\ \mathbf{b_3}+\mathbf{1}\end{matrix}; z(y)\right)\right] \\ & + C_4 Re_V \left[\frac{1+\sigma}{2} {}_2F_3\left(\begin{matrix}\mathbf{a_4}\\ \mathbf{b_4}\end{matrix}; z(y)\right) + z(y) \frac{\overline{a}_4}{\overline{b}_4} {}_2F_3\left(\begin{matrix}\mathbf{a_4}+\mathbf{1}\\ \mathbf{b_4}+\mathbf{1}\end{matrix}; z(y)\right)\right].\end{aligned} \tag{4.9}$$

where $\overline{a_i}$ and $\overline{b_i}$ are given in (3.31) and the derivative of the generalized hypergeometric functions (3.30) is employed. The four BC (4.5) in combination with the derivative of the eigenfunction now give rise to the homogeneous matrix equation

$$A_{ij}(\alpha, \omega, Re_V, Re)\, C_j = [0, 0, 0, 0]^T, \tag{4.10}$$

where the $\{i, j\} \in [1, 4]$. For a non-trivial solution the determinant of the coefficient matrix $\boldsymbol{A}$ has to vanish, yielding the dispersion relation

$$\mathcal{D}(\alpha, \omega, Re_V, Re) := \det\left(\boldsymbol{A}(\alpha, \omega, Re_V, Re)\right) = 0, \tag{4.11}$$

which essentially states an algebraic eigenvalue problem (EVP) for PCFT. Before proceeding to the analyses of the temporal and spatial stability problems, the asymptotic limit $Re_V \to \infty$ is examined. As will be demonstrated, for this limit PCFT can be transformed into the ASBL. Thus, for large Re_V, the stability equations derived for the ASBL in section 3.2 may readily be used for stability analyses for PCFT, which is advantageous as the corresponding EVP of the ASBL (3.35) consists of the determinant of a 2x2 matrix rather than a matrix 4x4 as derived for PCFT in (4.10).

4.2 Transformation to the asymptotic suction boundary layer in the large Re_V limit

As was elaborated in the context of figure 4.1, PCFT essentially evolves from a linear shear flow into an exponential flow with BL characteristics with increasing transpiration rates. Physically speaking, an increasing V_0 leads to flow blockage in the entire bulk and squeezes the flow profile to the upper wall. Albeit being an entirely different flow, the ASBL shares striking similarities with PCFT, both in the physical manifestation as well as in the mathematical representation of the solved Orr–Sommerfeld equation (OSE). By virtue of its definition, the ASBL also features BL characteristics. Thus, both laminar base profiles are characterized by exponential functions, concretely reading

$$\text{PCFT:} \quad U(y) = \frac{e^{Re_V y} - 1}{e^{Re_V} - 1}, \qquad V(y) = \frac{Re_V}{Re}, \tag{4.12a}$$

$$\text{ASBL:} \quad U(y) = 1 - e^{-y}, \qquad V(y) = -\frac{1}{Re}, \tag{4.12b}$$

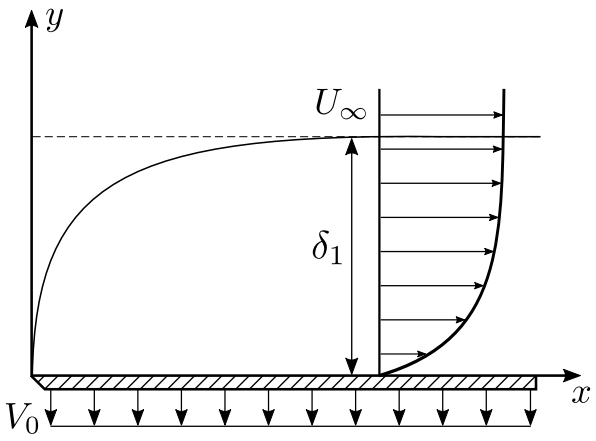

Figure 4.2: The dimensionless velocity profile of the ASBL with the displacement thickness δ_1 and wall-normal constant suction V_0. (adapted from Sun et al. (2022))

where $Re = U_\infty/V_0$ for the ASBL, which is obtained by taking the displacement thickness δ_1 as the characteristic length scale. Upon comparing PCFT at high Re_V and the ASBL, as depicted in figure 4.2, the velocity profiles turn out to be complementary. For PCFT, at the upper wall, where the BL is observed, the velocity reaches its maximum from where it decays exponentially towards the lower wall. In contrast, the ASBL reaches its minimum at the lower wall and recovers towards the free-stream velocity U_∞ for increasing distances from the wall. What essentially separates both flow profiles is a velocity shift. This discrepancy is resolved by employing the Galileo invariance of Newtonian mechanics, i.e. adding a negative velocity shift to PCFT of the form

$$\Delta U^* = -U_w, \tag{4.13}$$

in dimensional variables or

$$\Delta U = -1, \tag{4.14}$$

after non-dimensionalization. Adding the velocity shift (4.14) to (4.2) gives

$$\tilde{U}(y) = U(y) + \Delta U = \frac{e^{Re_V y} - 1}{e^{Re_V} - 1} - 1 = \frac{e^{Re_V y} - e^{Re_V}}{e^{Re_V} - 1}. \tag{4.15}$$

Naturally, the velocity profiles would not yet be identical. The velocity profile of PCFT exposed to (4.13) is mirrored around the y-axis when compared to the ASBL, as may easily be deduced from figure 4.1. Furthermore, the flow is still locked up by the both walls whereas the ASBL is defined on a semi-infinite domain. The latter difference may be accounted for via a coordinate transformation of the form

$$\tilde{y} = (1 - y)\, Re_V, \tag{4.16}$$

where $Re_V \to \infty$ is assumed since the BL phenomena for PCFT occur for large transpiration rates. A transformation as given in (4.16) has two effects. Firstly, the domain is mirrored around the x-axis, mapping the upper wall to the lower wall and vice versa. Secondly, by scaling with Re_V the formerly lower wall is mapped to infinity, i.e.

$$y = 0 \quad \Rightarrow \quad \tilde{y} \to \infty, \tag{4.17a}$$

$$y = 1 \quad \Rightarrow \quad \tilde{y} = 0, \tag{4.17b}$$

which as a result maps the domain between the two walls to a semi-infinite domain as given for the ASBL. Employing transformation (4.16) into (4.15) gives

$$\tilde{U}(\tilde{y}) = \frac{e^{Re_V}\left(e^{-\tilde{y}} - 1\right)}{e^{Re_V} - 1}. \tag{4.18}$$

The large Re_V limit then induces

$$\lim_{Re_V \to \infty} \tilde{U}(\tilde{y}) = e^{-\tilde{y}} - 1, \tag{4.19}$$

which equals the profile of the ASBL given in (4.12b) mirrored around the y-axis.
Now, the usefulness of such transformation in the context of LST is not yet established. After all transforming $U(y)$ and y in the mOSE (4.4) would not lead to any noteworthy simplifications. What may be attempted, though, is a transformation of the mOSE of PCFT (4.4) to the mOSE of the ASBL, which is given in (3.17), where a striking similarity is obvious. Both equations differ in the velocity profiles $U(y)$ as well as in the terms scaling inversely with the Reynolds number Re^{-1}. In fact, as will be demonstrated subsequently, the mOSE of PCFT can be transformed such that the base flow $U(y)$ is replaced by (4.19). For this, transformations of the wave parameters ω and α are going to be necessary. Once the mOSE of the ASBL is obtained, the extensive stability analyses performed for the ASBL in chapter 3 may be readily used for PCFT in the large Re_V limit.
First, a transformation of the wall-normal coordinate is necessary, given by

$$\mathrm{D}^n = (Re_V)^n \tilde{\mathrm{D}}^n, \tag{4.20}$$

where $\tilde{\mathrm{D}}^n$ is the nth derivative with respect to $\tilde{y}$. Considering (4.4), it becomes apparent that α must also be transformed so that later on the appearing powers of Re_V due to the transformation of the derivatives are cancelled out globally, i.e.

$$\alpha = -Re_V \tilde{\alpha}, \tag{4.21}$$

where the minus sign is readily explained upon comparing the transformed velocity profile (4.18) and the velocity profile of the ASBL:

$$\text{PCFT:} \quad \tilde{U}(\tilde{y}) = e^{-\tilde{y}} - 1, \tag{4.22a}$$

$$\text{ASBL:} \quad U(y) = 1 - e^{-y}. \tag{4.22b}$$

Subsequently, the velocity shift $\Delta U = -1$ is obtained via

$$\omega = Re_V(\tilde{\omega} - \tilde{\alpha}). \tag{4.23}$$

One central problem remains, which are the terms scaling with Re^{-1}. These terms will remain with a fourth power of Re_V, while all other terms will scale with a 3rd power of Re_V. This last hurdle is overcome by comparing the definitions of the Reynolds numbers for PCFT and the ASBL:

$$\text{PCFT:} \quad Re = \frac{U_w h}{\nu}, \quad Re_V = \frac{V_0 h}{\nu}, \tag{4.24a}$$

$$\text{ASBL:} \quad Re = \frac{U_\infty \delta_1}{\nu} = \frac{U_\infty}{V_0}. \tag{4.24b}$$

If one now assumes that $U_w = U_\infty$, a novel Reynolds number analogous to the Reynolds number for the ASBL must be defined for PCFT, which gives

$$\text{PCFT:} \quad \tilde{Re} := \frac{Re}{Re_V} = \frac{U_w}{V_0}. \tag{4.25}$$

With this, all necessary transformations are established. Employing all tilde quantities into the mOSE for PCFT (4.4) gives

$$\begin{aligned}\left[\left(-i\tilde{\omega} + i\tilde{\alpha}(-\tilde{U}(\tilde{y})) - \frac{1}{\tilde{Re}}\tilde{\mathrm{D}}\right)\left(\tilde{\mathrm{D}}^2 - \tilde{\alpha}^2\right) - i\tilde{\alpha}\tilde{\mathrm{D}}^2\left(-\tilde{U}(\tilde{y})\right)\right. \\ \left. -\frac{1}{\tilde{Re}}\left(\tilde{\mathrm{D}}^2 - \tilde{\alpha}^2\right)^2\right]\tilde{v}\left(1 - \frac{\tilde{y}}{Re_V}\right) = 0,\end{aligned} \tag{4.26}$$

which is mathematically equivalent to the mOSE of the ASBL given by (3.17). The four BC after transformation are lastly given by

$$\tilde{v}(y=0) = 0 \quad \Rightarrow \quad \tilde{v}(\tilde{y} = Re_V) = 0, \tag{4.27a}$$
$$\tilde{v}(y=1) = 0 \quad \Rightarrow \quad \tilde{v}(\tilde{y} = 0) = 0, \tag{4.27b}$$
$$\mathrm{D}\tilde{v}|_{y=0} = 0 \quad \Rightarrow \quad \tilde{\mathrm{D}}\tilde{v}|_{\tilde{y}=Re_V} = 0, \tag{4.27c}$$
$$\mathrm{D}\tilde{v}|_{y=1} = 0 \quad \Rightarrow \quad \tilde{\mathrm{D}}\tilde{v}|_{\tilde{y}=0} = 0, \tag{4.27d}$$

which completes the boundary value problem. After this point, the reader is referred to chapter 3, which presents a thorough temporal LST based on the analytical solution of the mOSE (3.17). One therefore saves the effort of examining PCFT for large Re_V in terms of the rather intricate solutions of (4.4) derived in section 4.1 and computed in the subsequent section 4.3. Moreover, a steep rise of computation time is observed when solving for eigenvalues at large Re_V. Thus, obtaining solutions via the ASBL is evidently more economic as well as arguably quite elegant.

4.3 Stability characteristics of plane Couette flow with transpiration

In this section, the stability characteristics of PCFT analogous to the ASBL are discussed. Due to the additional parameter Re_V, the parameter space automatically is increased by one dimension, due to which the 2D stability map is replaced by a 3D stability surface. The focus shall be laid on how the transpiration Reynolds number Re_V influences the stability of PCF, which without transpiration is known to be linearly stable, as was shown by Romanov (1973). Naturally, the critical quadruplet $\{\alpha_{cr}, \omega_{cr}, Re_{V,cr}, Re_{cr}\}$ is sought. Finally, spectra and eigenfunctions of PCFT are analyzed and compared to those of classical PCF.

4.3.1 Neutral stability surfaces, curves and critical parameters

The stability analysis presented here is reduced to the temporal case. The exclusion of the spatial stability case is justified in view of negligible knowledge gain obtained by including spatial stability analysis. The stability surfaces and maps presented for the temporal case hereafter are almost identical to the spatial case and therefore left undiscussed. In principal,

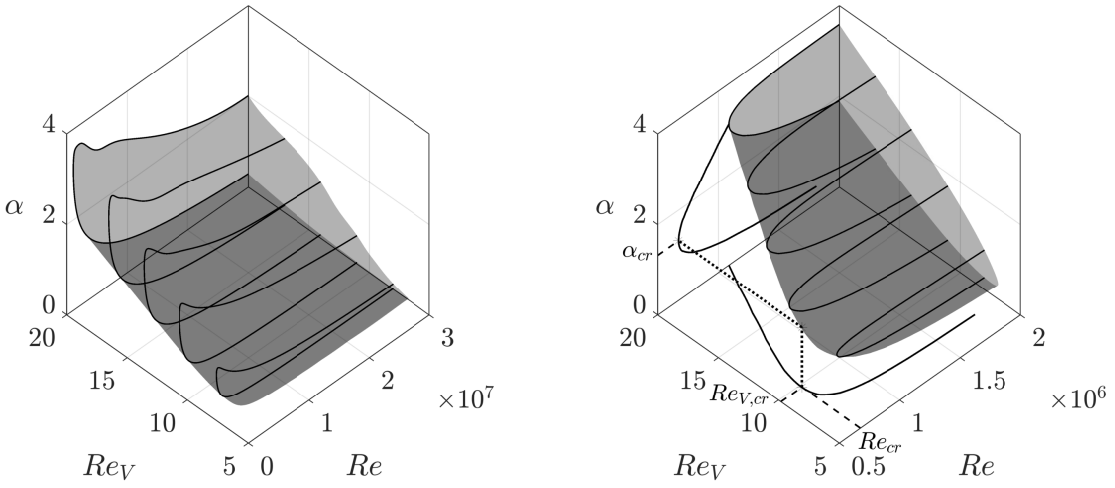

Figure 4.3: (a) Temporal stability surface for PCFT parametrized by α, Re_V and Re, where every point on the surface corresponds to a neutrally stable mode and points within correspond to unstable modes. (b) Temporal stability surface displayed with a maximum Reynolds number $Re_{max} = 2.0 \times 10^6$, where the surface is projected onto the α-Re-plane and the Re_V-Re-plane, respectively. The critical quadruplet may be referred to in (4.28d). (adapted from Sun et al. (2022))

the results in this chapter could be acquired in analogy to the ASBL, i.e. numerically solving the algebraic EVP (4.11) for its most unstable roots $\omega \in \mathbb{C}$. Due to the dispersion relation for PCFT being comprised by the determinant of a 4x4 matrix $\boldsymbol{A}$, the corresponding algebraic EVP is comprised of 24 non-zero terms containing products of ${}_2F_3$ generalized hypergeometric functions and their parameters. Computing an eigenvalue for such an extensive EVP in itself is computationally costly. This problem is amplified by the fact that Re_V increases the parameter space by one dimension. Thus, employing the homotopy method described in section 2.4.3 proved to be impractical. Therefore, the computation of the temporal eigenvalue spectra are conducted with Chebyshev collocation schemes published by Schmid et al. (2002). The code was adjusted to correctly solve the mOSE of PCFT (4.4). Further information of the code may be referred to in (Schmid et al., 2002).
The eigenvalue spectra were computed for $\alpha \in [0, 4.0]$, $Re_V \in [0, 20.0]$ and $Re \in [0, 3.0 \times 10^7]$. The analysis of large Re_V was omitted in view of increasingly costly and unreliable results. Fortunately, this case can be bypassed by exploitation of the transformations presented in section 4.2, thanks to which the analysis can in principal be performed with the stability equations of the ASBL.
Figure 4.3a displays the neutral stability surface obtained for above mentioned parameter space. This in itself is already a remarkable results, as it proves that PCF indeed becomes unstable in the presence of transpiration. The minimal transpiration Reynolds number, above which instability is possible, was quantified as $Re_{V,min} \approx 6.71$, as the asymptote in figure 4.4 indicates. All modes up to a Reynolds number of $Re = 3.0 \times 10^7$ with $Re_V < Re_{V,min}$ are calculated to be stable. It is assumed that this minimal transpiration Reynolds number holds for all Re so that all modes below this threshold should be stable, as is PCF representing the

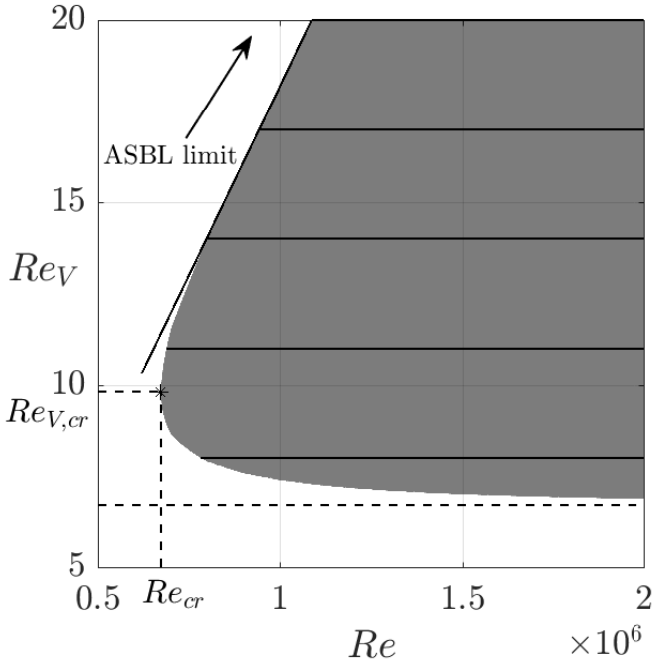

Figure 4.4: Projection of the temporal stability surface from figure 4.3b onto the Re-Re_V-plane in 2D. The critical parameters are given in (4.28d). The red-dashed line marks a threshold at $Re_V \approx 6.71$ below which all modes are stable regardless of Re and α. (adapted from Sun et al. (2022))

case $Re_V = 0$.
The lowest critical Reynolds number amounts to $Re_{cr} = 668350.49152$ and is displaced in figures 4.3b and 4.4. The corresponding critical quadruplet is given by

$$\alpha_{cr} = 1.32052, \tag{4.28a}$$
$$\omega_{cr} = 1.12311, \tag{4.28b}$$
$$Re_{V,cr} = 9.79923, \tag{4.28c}$$
$$Re_{cr} = 668350.49152, \tag{4.28d}$$

where all critical parameters are computed up to the fifth significant decimal in analogy to the critical triplet of the ASBL given in (3.64c). Notice that direct comparability of the parameters defined for the ASBL and for PCFT, respectively, is not quite possible due to the utilization of different characteristic length and velocity scales. Figure 4.3b shows projections of the neutral stability curve onto the α-Re- and Re_V-Re-planes. Of particular interest is the Re-Re_V-plane, which is depicted in figure 4.4. The projection of the neutral stability surface reveals a distinctive slope for the upper branch. The slope m is defined by

$$m := \frac{\Delta Re_V}{\Delta Re}, \tag{4.29}$$

for large enough Re_V. In section 4.2 it was shown that PCFT may be transformed to the ASBL in the limit $Re_V \to \infty$, which shall be referred to as ASBL-limit. For this transformation, the two Reynolds numbers in PCFT had to be redefined to a novel single Reynolds number $\tilde{Re}$

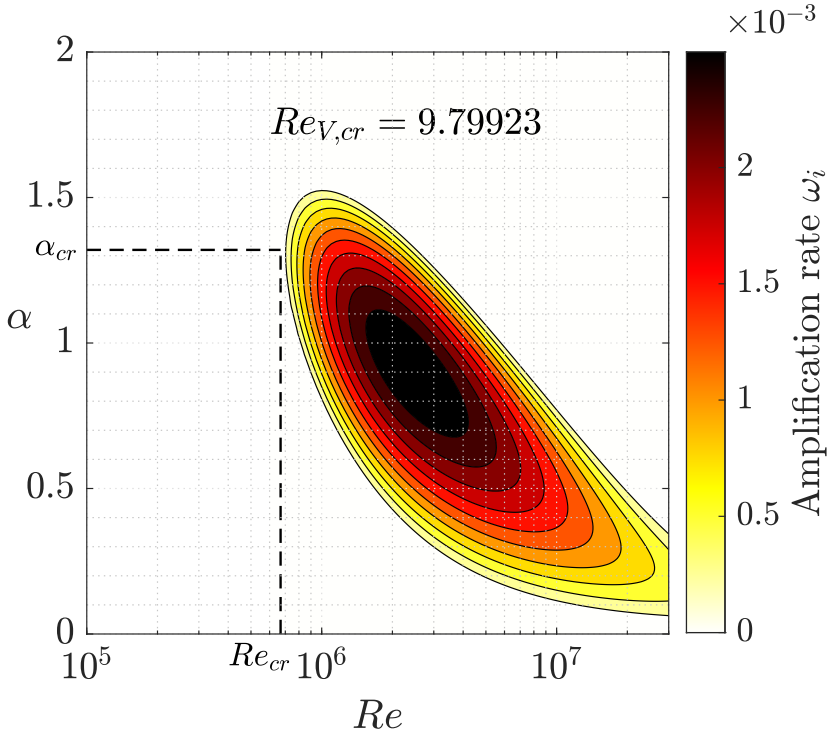

Figure 4.5: Temporal stability map given at the critical transpiration Reynolds number $Re_{V,cr} = 9.79923$. Shaded areas indicate unstable modes with maximum growth rates of $\omega_{i,max} \approx 2.5 \times 10^{-3}$. The shape of the thumb curve is similar to the corresponding stability map for the ASBL displayed in figure 3.5 (adapted from Sun et al. (2022))

defined in (4.25). Quite remarkably, this definition is inverse to the slope m given in (4.29). Even more remarkable is the value m^{-1} adapts for large Re_V, which in figure 4.4 roughly reads

$$m^{-1} = \frac{\Delta Re}{\Delta Re_V} \approx 55000. \tag{4.30}$$

Notice that the critical Reynolds number in the ASBL is given by $Re_{cr,ASBL} = 54378.62032$. The inverse of slope of the asymptote pointing towards the ASBL-limit shares the definition with $\tilde{Re}$, which in turn was introduced to transform PCFT to the ASBL for large Re_V. Furthermore, the inverse of the slope not only adapts roughly the same value as $Re_{cr,ASBL}$, the asymptote itself serves as a boundary between stable and unstable modes. These results together with the transformations in section 4.2 establish a remarkable unification of two initially very different wall-bounded shear flows in the limit $Re_V \to \infty$. Whether this unification can be expanded to other wall-bounded shear flows with transpiration is yet to be answered. The author motivates further investigations in this direction, e.g. examining plane Poiseuille flow with transpiration. Finally, the temporal stability map at the critical transpiration Reynolds number $Re_{V,cr} \approx 9.79923$ is displayed in figure 4.5. Comparison to figure 3.5 immediately reveals similarities of the temporal stability maps of ASBL and PCFT. Not only is the shape of the thumb curve similar, but even an area of maximum amplification is present in both stability maps.

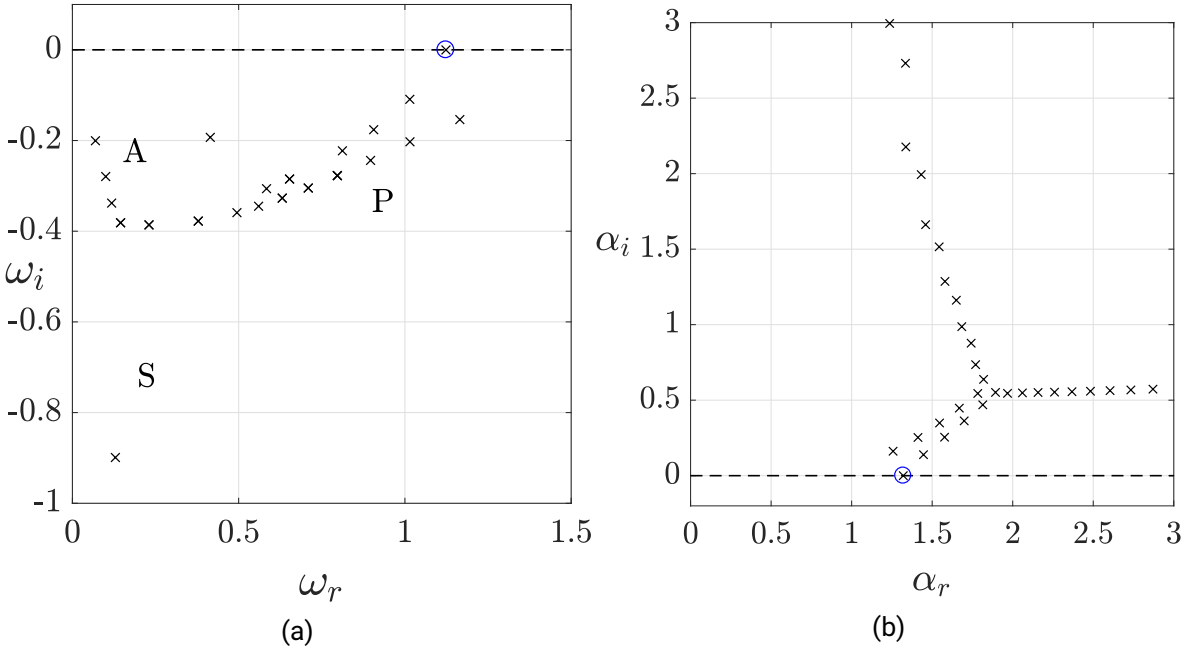

Figure 4.6: Temporal (a) and spatial (b) spectrum of PCFT for the critical parameters α_{cr} or ω_{cr}, respectively, as well as $Re_{V,cr}$ and Re_{cr} as given in (4.28d). The neutrally stable Tollmien–Schlichting (TS) mode is encircled in blue. In the temporal spectrum, the A-, P- and S-branches are discernible. (adapted from Sun et al. (2022))

4.4 Spectra and eigenfunctions

Similar to the spectra computed for the ASBL, the spectra of PCFT were first obtained with the adjusted Chebyshev collocation scheme of Schmid et al. (2002) and subsequently all spectra are filtered with the analytical EVP (4.11) by substituting all modes as initial guesses, which iteratively combs out spurious modes. This method combines the speed of Chebyshev collocation schemes with the physical correctness of the analytical solution of the mOSE (4.4). This method is highly suggested by the present author, as in many works in common literature, authors usually plot the spectra obtained by Chebyshev collocation schemes without questioning whether subsequently discussed modes are actually physical solutions of the mOSE or rather numerical artifacts. For the present spectra, the residual tolerance for filtering was set to $tol = 10^{-100}$, implying that a mode employed into the algebraic EVP must be reiterable to this precision in order to be regarded as a physical mode. Spurious modes generally are relocated to physical modes so that eventually the spectra contain physical modes exclusively. Figure 4.6a displays the temporal spectrum in the critical point with the respective parameters given in (4.28d). The TS mode is prominently located at the line of neutral stability and encircled in blue. The y-shaped temporal spectrum PCF is known for is quite discernible, albeit being distorted towards the vertical axis at $\omega_r = 0$. The A-, P- and S-branches were introduced for plane Poiseuille flow by Mack (1976), who extensively studied the respective temporal eigenvalue spectra. The branch going towards $\omega_r \to 0$ therein is called the A-branch, $\omega_r \to \alpha$ is the direction the P-branch is classically evolving towards whereas the S-branch forms a vertical line at $\omega_r \approx 2/3\alpha$. While the A- and P-branches are clearly following these categorizations, the S-branch is very sparse and shifted towards $\omega_r \approx 0.1$.

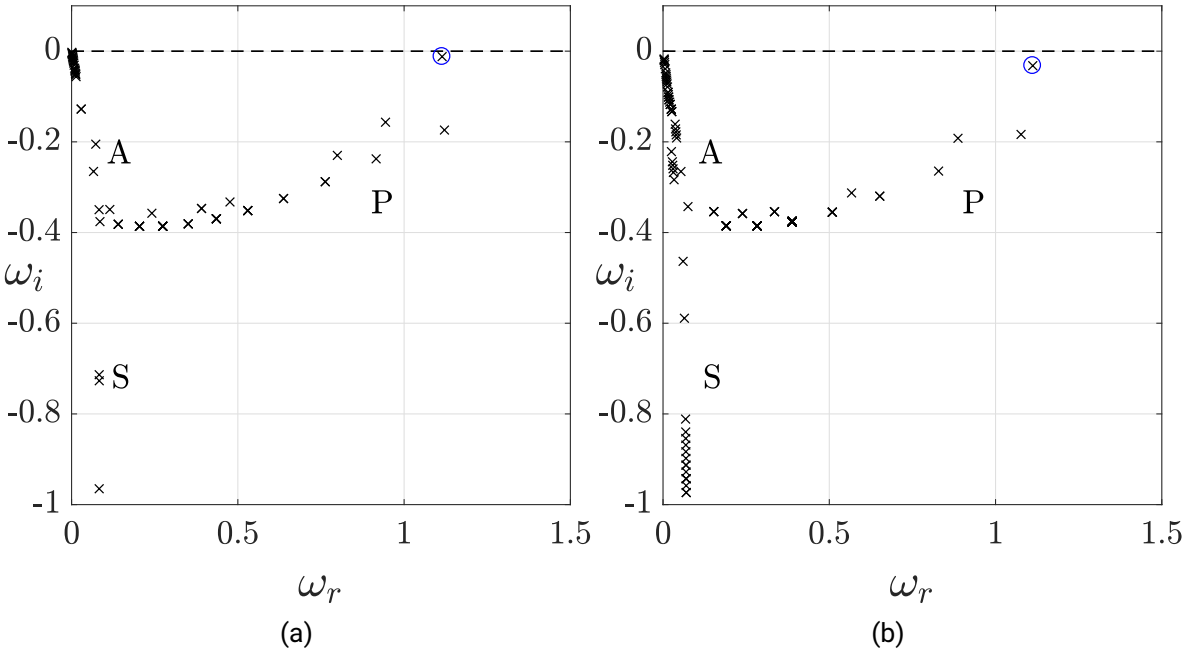

Figure 4.7: Two additional temporal spectra are depicted for (a) $Re_V = 15$ and (b) $Re_V = 20$. In contrast to figure 4.6a, the $S-$ branch is clearly visible and similarly distorted towards $\omega_r \approx 0.1$. (adapted from Sun et al. (2022))

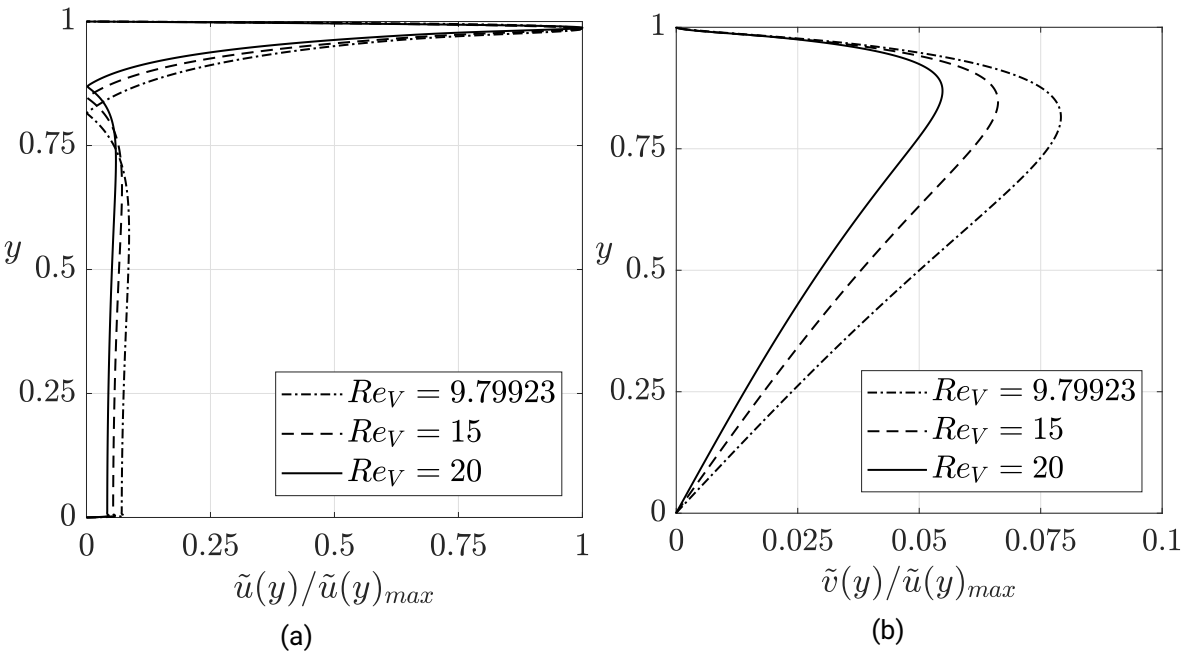

Figure 4.8: Streamwise (a) and wall-normal (b) eigenfunctions $\tilde{u}(y)$ and $\tilde{v}(y)$, respectively, rescaled by the maximum of the streamwise eigenfunction $\tilde{u}(y)_{max}$ for $Re_V = Re_{V,cr}$, $Re_V = 15$ and $Re_V = 20$. (adapted from Sun et al. (2022))

A similar branching is visible for the spatial spectrum in the critical point illustrated in figure 4.6b. The TS mode correctly is located at $\alpha_{cr} \approx 1.32052$ as given in (4.28d).
Additional temporal spectra for $Re_V = 15$ and $Re_V = 20$ at α_{cr} and Re_{cr} may be referred to in figures 4.7a and 4.7b. The branch-structure is similar to the spectra in the critical point, whereas the $S-$ branch for these cases are clearly visible and clearly relocated towards $\omega_r \approx 0.1$.
Lastly, the eigenfunctions in streamwise and wall-normal functions rescaled by $\tilde{u}(y)_{max}$ are displayed in figures 4.8a and 4.8b, respectively. The streamwise eigenfunction $\tilde{u}(y)$ is strongly squeezed towards the upper-wall, which is reminiscent of the laminar base profile shown in figure 4.1. Curiously, for all Re_V one can observe a clear local minimum at $y \approx 0.8$. The wall-normal eigenfunction $\tilde{v}(y)$ is an order of magnitude lower than its streamwise equivalent and much more present in the bulk. The shape of $\tilde{v}(y)$ is similar to analogous eigenfunctions in figure 3.8a for the ASBL. It is possible, although not demonstrated at this point, that both eigenfunctions may be transformed into one another with the transformation framework presented in section 4.2.

4.5 Summary and conclusions

The effect of transpiration on PCF was studied in a classical LSA based on methods already employed successfully in the chapter 3 for the ASBL. One key result is the onset of instability due to transpiration starting from transpiration Reynolds numbers $Re_V > Re_{V,min} \approx 6.71$. It seems that considerable cross-flow in the wall-normal direction destabilizes PCF. The critical quadruplet was computed precisely up to the fifth decimal place. The critical Reynolds number resulted as $Re_{cr} = 668350.49152$.
It was further shown that PCFT can be transformed to the ASBL for $Re_V \to \infty$ via specific coordinate and parameter transformations. This transformation is rediscovered by comparing the inverted slope of the asymptote discernible in the Re-Re_V-plane for large enough Re_V, which incidentally equalled the critical Reynolds number of the ASBL, further hinting at a universality wall-bounded shear flows with transpiration seem to share. The similarity of both flows is further manifested by comparing the temporal stability maps depicted for PCFT for the critical transpiration Reynolds number.
The temporal and spatial spectra were additionally plotted in the critical point, revealing a branch structure, which especially for the temporal spectra resembles a branching nomenclature coined by Mack (1976). The respective spectra for PCFT are similar to the ones known for PCF. However, the vertical S-branch is distorted at the presence of transpiration and shifted towards lower $\omega_r \approx 0.1$. Lastly, the eigenfunctions in streamwise and wall-normal direction were examined. The streamwise eigenfunctions $\tilde{u}(y)$ seem to be influenced by the BL effect revealed for PCFT for large Re_V at the upper-wall. The wall-normal eigenfunctions $\tilde{v}(y)$ in turn are strong in the bulk and resemble similar eigenfunctions for the ASBL, further hinting at a universality of wall-bounded shear flows with transpiration. From this point on, it would be interesting to see how instabilities in PCFT evolve structurally in the laminar-turbulent transition process. It remains to be answered if the famous turbulent stationary rolls numerically proven by Kraheberger et al. (2018) can be tracked down to modes of instability in PCFT. Still, transpiration proved to be one possible reason for transitioning PCF. Another phenomenon possibly inducing transition is presented in the last two chapters.

5 Extension of Squire's transformation to spatial stability and novel unstable oblique modes

This chapter is based on a soon-to-be submitted manuscript authored by Oberlack, Turkac and Yalcin (2022) named in alphabetical order with the provisional title *On a new set of unstable three-dimensional (3D) oblique modes examplified by plane Couette flow*. The order of authors is still in discussion and the disagreement is not yet resolved at the time this dissertation is handed in. The theory presented in this chapter is based on a systematization and subsequent extension of the Squire's transformation introduced in section 2.4.4 in terms of Lie symmetry theory. This idea was introduced by Oberlack, who among other theories notably employed Lie group analysis to unify solution sets for the mean velocity of stationary parallel turbulent shear flows (Oberlack, 2001), co-authored works introducing a systematization of ansatz functions in linear stability theory (LST) (Nold and Oberlack, 2013; Nold et al., 2015), discussed in section 3.2.4, and very recently expanded the understanding of how scaling laws for arbitrary moments in turbulent wall-bounded shear flows may be derived in first principles thinking through Lie symmetry theory (Oberlack et al., 2022). The application of Lie symmetry theory on the parameter set of the Orr–Sommerfeld equation (OSE) therefore is a logical continuation of the successful application of Lie symmetry theory in hydrodynamic stability theory and turbulence. The arising equations are discussed later in section 5.2, where the algebraic set of invariance conditions (5.19) arising from aforementioned exploitation of symmetry theory was partly solved by Turkac (2019) and later corrected and completed by the present author, who applied the theory on plane Couette flow (PCF) in the present chapter and verified the legitimacy of ensuing results in chapter 6 through a direct numerical simulation (DNS) conducted with the open source spectral element code *nek5000* (Fischer et al., 2008).

As was summarized in the introductory words of chapter 4, PCF is known to be linearly stable for any Reynolds number. Today it is known that PCF in fact undergoes transition when finite-amplitude disturbances are present in the flow as was elaborated by Orszag and Kells (1980). These finite-amplitude disturbances in turn are assumed to be footprints of the large-scale turbulent superstructures forming in laminar-turbulent PCF. Closely related to PCF is the flow forming between two counter-rotating cylinders, i.e. Taylor-Couette flow (TCF). Due to its relatively simple experimental setup, TCF was early examined in detail with regard to its transition to turbulence. Coles (1965) discovered the occurrence of spiral-shaped intermittent turbulent structures in TCF, which fittingly are sometimes referred to as *barber pole turbulence*. Naturally, the question presented itself whether similar inclined persisting structures could also be observed in PCF. Indeed, in the aforementioned works of Daviaud et al. (1992) inclined laminar-turbulent stripe patterns were presented, albeit only one or two turbulent spots could be visualized. It was later specified that these rather singular spots are due to the large wavelengths – roughly 40 times the half-gap width in PCF – and consequently

by increasing dimensions in stream- and spanwise directions with respect to the half-gap width, Prigent et al. (2002) could successfully resolve the laminar-turbulent patterns fully. Thereafter, numerical studies by Barkley and Tuckerman (2005) were capable of reproducing these results by accounting for the large spanwise wavelengths of the patterns and employing domains of $L'_x \times L'_y \times L'_z = 10 \times 2 \times 120$, where the x-z-plane is tilted by varying angles θ. The emerging laminar-turbulent oblique patterns ranged from $\theta_{min} = 15°$ to $\theta_{max} = 66°$ at $Re = 350$. Duguet and Schlatter (2013) investigated the obliqueness of these patterns analytically by means of a clear scale separation and came to the conclusion that they are induced by the incompressibility of the large-scale flows. It is yet to be answered, however, where the oblique structures originate from and which phenomenon defines the distinct inclination angles. Against this background, the present goal is to provide a new link to the 3D spatial stability problem.

In view of Squire's theorem (Squire, 1933), the investigation of 3D modes was neglected as two-dimensional (2D) modes are most critical in the temporal framework, which was naively assumed for the spatial stability problem as well. Squire showed for the temporal case that the investigation of the 3D temporal eigenvalue problem can in fact be omitted entirely by making use of the Squire's transformation, which can be stated in a modern form as an equivalence transformation (see e.g Bluman and Kumei 2013). This is a special form of the symmetry transformations, in which the parameters appearing in the equation, such as the wave numbers α and β, are also part of the transformation. Essentially identical to symmetry transformations, equivalence transformations seek a transformation under the condition that the underlying equation does not change under the transformation, i.e. remains invariant. Squire discovered that the OSE for 2D and 3D perturbations are identical in form if one takes into account the occurring parameters, i.e. α, β, Re and ω in the transformation. Although it was easy to conclude from this that 2D modes are always the most unstable modes, LST did not give satisfactory results for a number of the above flows, i.e. the critical Reynolds number was not calculated correctly.

Squire's theorem was originally derived for the temporal stability problem, i.e. α and β are real numbers whereas ω is the complex eigenvalue, and in fact it does not hold for the spatial problem where α is complex. Indeed, Mack (1977) stated that the utility of Squire's theorem is lost if complex α and β are assumed, reinforcing the idea that the theorem must be applied only in the temporal framework. However, Benjamin (1961) remarked in a side note the theorem of Squire should also hold for complex values of β. He even went further and stated that critical Reynolds numbers below the 2D critical value subsequently become a possibility. To the present author's surprise, the suggestion of complex β in the context of Squire's theorem has not been subject of further analysis since then.

In the present chapter, the modification of the spatial stability problem by a complex spanwise wave number β is investigated with respect to Squire's theorem. First hints towards the potential existence of oblique modes investigated hereafter are given in Turkac (2019). We will show that assuming $\beta \in \mathbb{C}$ is necessary to extend Squire's transformation to spatially developing disturbances. Thus, the perturbations may now witness spanwise growth or decay, leading to novel 3D modes with oblique amplification. At the same time these modes naturally give rise to a symmetry breaking of the spanwise reflection symmetry. A result is the negation of Squire's theorem for the spatial case, as the 3D Reynolds numbers arising from the transformation of 2D to 3D modes may in fact be lower than the initial 2D Reynolds numbers.

As was demonstrated in previous research, symmetry breaking in PCF due to laminar-turbulent structures is a common occurrence and hardly a singular observation. In addition to the mentioned works of Daviaud et al. (1992), Barkley and Tuckerman (2005), Tuckerman and

Barkley (2011), which analyze oblique laminar-turbulent patterns in PCF, similar oblique patterns have been discovered in PCF with a heated upper and cooled lower plate (Fukudome et al., 2018). In the context of turbulent flow control of PCF, imposing seed velocity perturbations that are non-symmetric in the spanwise direction led to a symmetry breaking of the turbulence spanwise reflection symmetry in Chagelishvili et al. (2014). The occurrence of symmetry breaking is discussed in more detail in section 5.2, where non-zero spanwise amplification rates are derived by the proposed extension of Squire's transformation.
The idea of extending Squire's transformation has been previously discussed in the literature, albeit in different contexts. As an example, Jerome and Chomaz (2014) have discussed the validity of the classical Squire's transformation when transient growth mechanisms are considered. They extended the framework to the entire eigenfunction structure of Orr–Sommerfeld (OS) and Squire modes. In contrast to the extensions presented in this chapter, however, they consider the temporal stability problem and assume α and β to be real valued. To the best knowledge of the author the theory presented hereafter has not yet been discussed in the literature and therefore should represent an important addition to the theory of linear stability.

5.1 Revisiting Squire's transformation as an equivalence transformation

Squire's famous transformation (Squire, 1933) constitutes a central achievement in LST in that it essentially renders the analysis of the 3D temporal eigenvalue problem (EVP) superfluous by means of transforming the 2D parameter set of OSE (2.43) to 3D so that the underlying ordinary differential equation (ODE) itself is kept invariant. This represents what in group theory is called a symmetry transformation. The idea of symmetries in the context of differential equations is swiftly understood when considering the one-dimensional (1D) heat equation

$$\frac{\partial u}{\partial t} - \frac{\partial^2 u}{\partial x^2} = 0, \tag{5.1}$$

which is a second order partial differential equation (PDE) for the temperature $u(x,t)$. Now, a symmetry essentially describes a point transformation $\mathbf{T} = (\hat{x}, \hat{t}, \hat{u})$ with

$$\hat{x} = \hat{x}(x,t,u;\epsilon), \qquad \hat{t} = \hat{t}(x,t,u;\epsilon), \qquad \hat{u} = \hat{u}(x,t,u;\epsilon), \tag{5.2}$$

where ϵ denotes the group parameter, which, applied to the quantities in (5.1), leaves the original differential equation form-invariant, i.e.

$$\frac{\partial \hat{u}}{\partial \hat{t}} - \frac{\partial^2 \hat{u}}{\partial \hat{x}^2} = 0. \tag{5.3}$$

One example for a symmetry of (5.1) or (5.3) is the two-parameter scaling group

$$\hat{x} = e^{\epsilon_1} x, \qquad \hat{t} = e^{2\epsilon_1} t, \qquad \hat{u} = e^{\epsilon_2} u, \tag{5.4}$$

where $\epsilon_1, \epsilon_2 \in \mathbb{R}$ represent the respective continuous group parameters. Subsequently employing (5.4) into (5.1) evidently yields (5.3), as the scaling factors cancel identically on both sides.

Evidently, (5.1) is left invariant by the two-parameter scaling transformation (5.4).
Now, the Squire's transformation (Squire, 1933) is a special type of symmetry transformation, where the original 2D OSE is left form-invariant upon a symmetry transformation of the parameters $(\alpha_{2D}, \omega_{2D}, Re_{2D})$, which in the literature is typically referred to as an equivalence transformation (see e.g. Bluman and Kumei 2013). The classical approach rewritten as an equivalence transformation is to declare the spanwise wave number β, which generates 3D disturbances, as the group parameter and find a point transformation in analogy to (5.2) for the parameter set of the form

$$\alpha_{3D} = \Phi_\alpha(\alpha_{2D}, \omega_{2D}, Re; \beta), \tag{5.5a}$$
$$\omega_{3D} = \Phi_\omega(\alpha_{2D}, \omega_{2D}, Re; \beta), \tag{5.5b}$$
$$Re_{3D} = \Phi_{Re}(\alpha_{2D}, \omega_{2D}, Re; \beta), \tag{5.5c}$$

so that the 2D OSE

$$L_{OS,2D}(\tilde{v}(y); \alpha_{2D}, \omega_{2D}, Re_{2D}) = 0, \tag{5.6}$$

is kept invariant by means of the equivalence transformation (5.5c). Here, $L_{OS,2D}$ denotes the OS differential operator in 2D. Employing (5.5c) into the 3D OSE (2.43) then yields

$$L_{OS,3D}(\tilde{v}(y); \alpha_{3D}(\beta), \omega_{3D}(\beta), Re_{3D}(\beta)) = 0. \tag{5.7}$$

Squire found an equivalence transformation upon comparison of the parameter terms in equation (2.43) in both the 2D and 3D OSE, which reveals that

$$\alpha_{2D}^2 = \alpha_{3D}^2 + \beta^2, \tag{5.8a}$$
$$Re_{2D}\alpha_{2D} = Re_{3D}\alpha_{3D}, \tag{5.8b}$$
$$Re_{2D}\omega_{2D} = Re_{3D}\omega_{3D}, \tag{5.8c}$$

must hold. Squire's original transformation is conducted in the framework of temporal stability, i.e. $\omega \in \mathbb{C}$ and $\alpha, \beta \in \mathbb{R}$. Upon employing (5.8) one may obtain any 3D parameter set from the 2D parameter set via

$$\alpha_{3D} = \sqrt{\alpha_{2D}^2 - \beta^2}, \tag{5.9a}$$
$$\omega_{3D,r} = \omega_{2D,r}\frac{\sqrt{\alpha_{2D}^2 - \beta^2}}{\alpha_{2D}}, \tag{5.9b}$$
$$\omega_{3D,i} = \omega_{2D,i}\frac{\sqrt{\alpha_{2D}^2 - \beta^2}}{\alpha_{2D}}, \tag{5.9c}$$
$$Re_{3D} = Re_{2D}\frac{\alpha_{2D}}{\sqrt{\alpha_{2D}^2 - \beta^2}}, \tag{5.9d}$$

which is the well-known classical Squire's transformation. Once again, if compared to (5.1) – (5.3) it becomes evident that (5.9) is a point transformation of the OSE in parameter space $\{\alpha, \beta, \omega, Re\}$ with β as the group parameter. From Squire's transformation follows Squire's theorem (5.9d) which states that after transformations (5.9) of a 2D mode the corresponding 3D mode always has a higher 3D Reynolds number. In particular, given a shear flow has a critical parameter set $\{\alpha_{2D,cr}, \omega_{2D,cr}, Re_{cr}\}$, the corresponding critical 3D mode is given at a higher Reynolds number. Hence, in the temporal framework of LST the most critical mode is always the 2D mode.

5.2 Extended Squire's transformation for spatially developing instabilities and oblique modes

In analogy with the approach presented for the temporal case, the idea is to derive transformations similar to (5.9) for the OSE describing spatial instabilities. The classical spatial LST features a complex streamwise wave number, i.e. $\omega, \beta \in \mathbb{R}$ and $\alpha = \alpha_r + i\alpha_i \in \mathbb{C}$, due to which (5.8) yields

$$\alpha_{2D,r}^2 - \alpha_{2D,i}^2 = \alpha_{3D,r}^2 - \alpha_{3D,i}^2 + \beta^2, \tag{5.10a}$$

$$\alpha_{2D,r}\alpha_{2D,i} = \alpha_{3D,r}\alpha_{3D,i}, \tag{5.10b}$$

$$Re_{2D}\alpha_{2D} = Re_{3D}\alpha_{3D}, \tag{5.10c}$$

$$Re_{2D}\omega_{2D} = Re_{3D}\omega_{3D}. \tag{5.10d}$$

Solving (5.10c) for α_{3D} gives

$$\alpha_{3D} = \alpha_{2D}\frac{Re_{2D}}{Re_{3D}}. \tag{5.11}$$

Substituting (5.11) into (5.10b) gives

$$\alpha_{2D,r}\alpha_{2D,i} = \alpha_{3D,r}\alpha_{3D,i}\left(\frac{Re_{2D}}{Re_{3D}}\right)^2, \tag{5.12}$$

which is obviously a contradiction unless the trivial case $Re_{2D} = Re_{3D}$ applies. This contradiction can be elegantly resolved by assuming the more general case $\alpha, \beta \in \mathbb{C}$. As will be shown, a complex spanwise wave number β alters (5.10b), which allows to resolve (5.12). With β being complex, it cannot serve as a group parameter anymore, which requires a new group parameter in order to keep the 2D OSE (2.43) invariant. A physically intuitive and logical candidate for the new group parameter is the ratio of 2D and 3D Reynolds numbers

$$\phi := \frac{Re_{2D}}{Re_{3D}}, \tag{5.13}$$

so that instead of (5.7) we now use

$$L_{OS,3D}(\tilde{v}(y); \alpha_{3D}(\phi), \omega_{3D}(\phi), Re_{3D}(\phi), \beta(\phi)) = 0, \tag{5.14}$$

where $\beta(\phi)$ now is not a parameter but rather a solution parametrized by ϕ arising from the invariance conditions (5.8).
Analogous to the temporal OSE, the symmetry of the spatial OSE is investigated by employing a complex spanwise wave number ($\omega \in \mathbb{R}$ and $\alpha, \beta \in \mathbb{C}$). One can directly start with (5.8a) - (5.8c), where now instead of the frequency the streamwise wave number α is split into real and imaginary parts

$$\alpha_{2D} = \alpha_{2D,r} + i\alpha_{2D,i}, \tag{5.15}$$

$$\alpha_{3D} = \alpha_{3D,r} + i\alpha_{3D,i}. \tag{5.16}$$

From the argument above additionally the spanwise wave number β can be split into its real and imaginary parts

$$\beta = \beta_r + i\beta_i. \tag{5.17}$$

The resulting eigenfunction thus is given by

$$\begin{aligned} v(x,y,z,t) &= \tilde{v}(y)\, e^{i(\alpha_{3D}x+\beta z-\omega t)} \\ &= \tilde{v}(y)\, e^{i(\alpha_{3D,r}x+\beta_r z-\omega t)} e^{-\alpha_{3D,i}x-\beta_i z}, \end{aligned} \tag{5.18}$$

which corresponds to a wave with oblique growth in the x-z-plane and a propagation vector with both stream- and spanwise components. The invariant conditions (5.8a) - (5.8c) in turn are altered due to the presence of complex spanwise wave numbers $\alpha, \beta \in \mathbb{C}$, giving

$$\alpha_{2D,r}^2 - \alpha_{2D,i}^2 = \alpha_{3D,r}^2 - \alpha_{3D,i}^2 + \beta_r^2 - \beta_i^2, \tag{5.19a}$$

$$\alpha_{2D,r}\alpha_{2D,i} = \alpha_{3D,r}\alpha_{3D,i} + 2\beta_r\beta_i, \tag{5.19b}$$

$$Re_{2D}\alpha_{2D} = Re_{3D}\alpha_{3D}, \tag{5.19c}$$

$$Re_{2D}\omega_{2D} = Re_{3D}\omega_{3D}. \tag{5.19d}$$

Similar to the classical Squire approach, we intend to solve for the 3D quantities when the 2D quantities are given.
The ultimate goal is to identify oblique modes with 3D Reynolds numbers which are lower than the 2D Reynolds numbers, i.e. with (5.13) $\phi < 1$. Equations (5.13) and (5.19c) - (5.19d) lead to

$$Re_{3D} = \phi Re_{2D}, \qquad \alpha_{3D,r} = \frac{\alpha_{2D,r}}{\phi}, \qquad \alpha_{3D,i} = \frac{\alpha_{2D,i}}{\phi}, \qquad \omega_{3D} = \frac{\omega_{2D}}{\phi}. \tag{5.20}$$

In the upcoming discussion, in (5.18) $\alpha_r > 0$ is assumed, i.e. perturbation waves exclusively propagate in downstream direction.
Inserting the transformations (5.20) in (5.19b) one finds

$$\beta_i = \left(1 - \frac{1}{\phi^2}\right) \frac{\alpha_{2D,r}\alpha_{2D,i}}{\beta_r}. \tag{5.21}$$

Equation (5.21) represents a key result. For $\phi \neq 1$ and $\alpha_{2D,i} \neq 0$, i.e. off the neutral stability curve, one obtains $\beta_i \neq 0$. This implies growth or decay is observed in one direction of the spanwise coordinate, complemented by opposing decay or growth in converse spanwise direction. This gives rise to novel perturbation waves with 3D oblique growth mechanisms in the x-z-plane. Furthermore, a non-zero spanwise amplification rate β_i immediately leads to a symmetry breaking in spanwise direction. Reflection symmetry is generally maintained in classical LST due to real valued spanwise wave numbers β.
Now, substituting β_i into (5.19a) gives

$$\beta_r^4 - (\alpha_{2D,r}^2 - \alpha_{2D,i}^2)\left(1 - \frac{1}{\phi^2}\right)\beta_r^2 - (\alpha_{2D,r}\alpha_{2D,i})^2\left(1 - \frac{1}{\phi^2}\right)^2 = 0, \tag{5.22}$$

which is solved by

$$\beta_r = \pm\sqrt{\frac{1}{2}\left(1 - \frac{1}{\phi^2}\right)\left(\alpha_{2D,r}^2 - \alpha_{2D,i}^2 \pm \left(\alpha_{2D,r}^2 + \alpha_{2D,i}^2\right)\right)}, \tag{5.23}$$

where the inner and outer plus-minus signs lead to four distinct solutions. Employing (5.23) into (5.21) and reconstructing $\beta = \beta_r + i\beta_i$ concretely gives

$$\beta_{1,2} = \pm\sqrt{1 - \frac{1}{\phi^2}}\,(\alpha_{2D,r} + i\,\alpha_{2D,i}), \tag{5.24a}$$

$$\beta_{3,4} = \pm\sqrt{\frac{1}{\phi^2} - 1}\,(\alpha_{2D,i} - i\,\alpha_{2D,r}), \tag{5.24b}$$

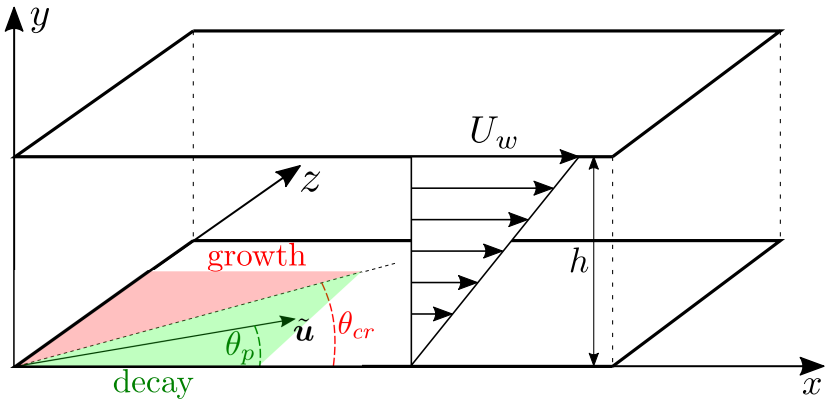

Figure 5.1: Flow domain with upper wall velocity U_w, the laminar base profile and a perturbation $\tilde{\boldsymbol{u}}$. The wave and growth mechanics are described with the corresponding angles θ_p and θ_{cr} respectively as defined in (5.26) and (5.28) for oblique 3D modes as defined in equation (5.18) and induced by $\phi < 1$.

where the first two solutions arise when taking the inner plus sign and the latter two solutions emerge for an inner minus sign.
In fact, for $\phi > 1$ both (5.24a) and (5.24b) are equivalent, i.e. $\beta_{1,2} = \beta_{3,4}$, whereas if $\phi < 1$ the outer signs are flipped so that $\beta_{1,2} = -\beta_{3,4}$. Swapping the outer signs in (5.24a) and (5.24b), however, merely mirrors the perturbations along the x-y-plane, which, from a physical point of view, does not make a difference. Hence, it is sufficient to only consider the outer plus sign, which leaves one unique solution

$$\begin{aligned} \beta &= \sqrt{1 - \frac{1}{\phi^2}}\,(\alpha_{2D,r} + i\,\alpha_{2D,i}) \qquad \text{for } \phi > 1, \\ \beta &= \sqrt{\frac{1}{\phi^2} - 1}\,(\alpha_{2D,r} - i\,\alpha_{2D,i}) \qquad \text{for } \phi < 1. \end{aligned} \tag{5.25}$$

The intrinsically interesting case arises when $\phi < 1$, since this implies unstable subcritical modes or even unstable 3D modes for originally stable 2D modes.
For the case of stable 2D flows, i.e., $\alpha_{2D,i} > 0$, β_r and β_i have opposite signs, resulting in the 3D wave propagating in the spanwise direction in which the perturbation field experiences growth. However, since according to (5.20) the wave continues to decay in the pure flow direction even in the 3D case, the question arises whether the wave is fanned in the propagation direction in the x-z-plane or decays, as in the 2D case. In the case of unstable 2D flows, i.e., $\alpha_{2D,i} < 0$, exactly the opposite case presents itself. Examining (5.25) for $\phi < 1$, i.e., for potentially subcritical 3D modes, we notice that for this case β_r and β_i have the same sign. Thus, after transformation, the 3D wave propagates in that spanwise direction in which the field decays. Analogously, in the 3D case according to (5.20), an amplification of the wave in the pure flow direction occurs, which is why there is again the question of whether the wave in the 3D case is amplified in the propagation direction or decays. In particular, for this case, fanning in the 3D case would mean that subcritical 3D modes could be constructed, which would be in clear contradiction to Squire's theorem.

These questions are straightforwardly answered by comparing the propagation angle θ_p and critical angle θ_{cr} visible in figure 5.1. These angles may be derived upon considering the exponent of the wall-normal eigenfunction (5.18). The imaginary part of the exponent gives

rise to the propagation angle θ_p of waves in the x-z-plane, which in conjunction with (5.20) is determined by

$$\theta_p = \arctan\left(\frac{\beta_r}{\alpha_{3D,r}}\right) = \arctan\left(\frac{\beta_r}{\frac{1}{\phi}\alpha_{2D,r}}\right). \tag{5.26}$$

Additionally, a critical angle θ_{cr} may be defined from the real part in the exponent of (5.18) at which spanwise growth as well as streamwise decay neutralize one another, i.e. $\alpha_{3D,i}\, x + \beta_i\, z = 0$. Thus, the condition for the neutral stability line is given by

$$\alpha_{3D,i} + \beta_i \tan(\theta_{cr}) = 0, \tag{5.27}$$

which for θ_{cr} together with (5.20) and (5.21) yields

$$\theta_{cr} = \arctan\left(-\frac{\alpha_{3D,i}}{\beta_i}\right) = \arctan\left(\frac{\beta_r}{\left(\frac{1}{\phi} - \phi\right)\alpha_{2D,r}}\right). \tag{5.28}$$

The 3D modes for linearly stable 2D flows, such as 2D PCF, would now be unstable in the propagation direction if $\theta_p > \theta_{cr}$, as then the spanwise growth component is larger than the spanwise decay component. When linearly unstable 2D flows are transformed, $\phi > 1$ always generate unstable 3D modes, as according to (5.20) and (5.25) both $\alpha_{3D,i} < 0$ as well as $\beta_i < 0$, leading to growth in stream- and spanwise directions. In contrast, $\phi < 1$ demands yet again a comparison of θ_p and θ_{cr}, when specifically $\theta_p < \theta_{cr}$ represents the instability condition, since $\alpha_{3D,i} < 0$ and $\beta_i > 0$ by virtue of the transformations (5.20) and (5.25).
Comparison of the respective arguments of the arc tangent in (5.26) and (5.28) reveals that for $\phi < 1$ it follows that $\theta_p < \theta_{cr}$, independent of the selected 2D parameter set. Correspondingly, we conclude that linearly stable 2D modes remain stable in 3D regardless of ϕ, whereas linearly unstable 2D modes in fact always transform into linearly unstable 3D modes for both $\phi > 1$ and $\phi < 1$. This result is quite remarkable, as then the critical point $Re_{2D,cr}$ may be transformed to a subcritical 3D Reynolds number with $\phi < 1$. Consequently, in the spatial framework Squire's theorem does not hold, which embodies another key result of the present chapter. It is thereby possible to construct unstable subcritical 3D oblique modes for linearly unstable 2D flows.

6 Direct numerical simulations of oblique modes in plane Couette flow

In the following chapter, the attempt is made to verify the existence of three-dimensional (3D) oblique modes in plane Couette flow (PCF). For this, firstly the spatial stability problem for two-dimensional (2D) PCF is solved for 2D modes, which in turn are transformed to 3D modes in accordance with the transformation rules (5.20) and (5.25). Afterwards, these modes are introduced into an unperturbed 3D PCF over the stream- and spanwise boundaries in a direct numerical simulation (DNS). Thereupon the ensuing flow fields are investigated regarding whether the perturbation field predicted analytically is replicated in the entire field by the flow solver for large enough turnover times.

6.1 Spatial stability problem of plane Couette flow and generation of 3D modes with oblique growth

In this subsection the existence of 3D modes with spatial oblique amplification, i.e. $\alpha_i \neq 0$ and $\beta_i \neq 0$, is discussed for PCF and verified via DNS of the Navier–Stokes equations (NSE) (2.30). For PCF, an analytical solution of the 2D Orr–Sommerfeld equation (OSE) (2.43) of the form $\tilde{v}(y) = \sum_{n=1}^{4} C_n \tilde{v}_n(y)$ may be derived in terms of exponential and Airy functions (Reid, 1979) and is given in full detail in Appendix B. Demanding non-trivial solutions for the coefficient vector $\boldsymbol{C}$ in $(B.2)$ yields the dispersion relation

$$\mathcal{D}(\alpha, \beta, \omega, Re) := \det(\boldsymbol{A}) = 0, \tag{6.1}$$

where $\boldsymbol{A}$ is the coefficient matrix arising from the boundary condition (BC) (2.56) and is given in detail in (B.2). This establishes an algebraic eigenvalue problem (EVP) for whichever parameter is chosen to be complex. The 2D spatial EVP of interest arises for the case $\beta = 0$, $\omega \in \mathbb{R}$ and $\alpha \in \mathbb{C}$. In order to obtain the 2D eigenvalues, which are then to be transformed to 3D modes with oblique growth mechanics according to (5.20) and (5.25), we could in principle numerically solve equation (6.1). However, it turned out to be more time-efficient to get estimates for the eigenvalues using a collocation scheme and reiterate on (6.1) to a given very small residuum instead of computing eigenvalues from (6.1) directly. For this, a Chebyshev collocation MATLAB code by Schmid et al. (2002) was employed. The number of modes was set to $m = 200$, which provides 2D spatial eigenvalues leaving a comparatively small residuum when substituted into the algebraic EVP (6.1). As any solution obtained by the Chebyshev collocation method must be iterable to arbitrarily small residua, the computed eigenvalues were then used in (6.1) as starting points in a non-linear complex root finding algorithm (Muller, 1956) and reiterated to residua of $O(10^{-10})$, which was smaller than any

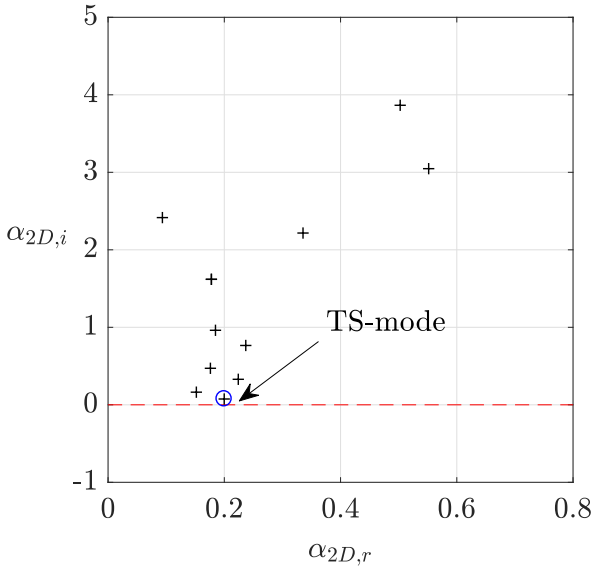

Figure 6.1: A part of the 2D spatial eigenvalue spectrum of PCF with $\omega_{2D} = 0.1$ and $Re_{2D} = 1000$ is displayed for modes with $\alpha_{2D,i} < 5$. All modes employed into (6.1) yield a residuum smaller than $r = 10^{-10}$. The TS mode is encircled in blue.

	2D parameters	3D parameters
Reynolds number Re	1000	350
streamwise wave number α	$0.19983 + 0.074993\,i$	$0.57094 + 0.21427\,i$
spanwise wave number β	0	$0.20071 - 0.53483\,i$
wave frequency ω	0.1	0.28571

Table 6.1: Transformation of 2D to 3D parameters with Reynolds number ratio $\phi = 0.35$ as transformation parameter according to (5.20) and (5.25).

residua of the initial set of eigenvalues. Non-iterable modes, on the other hand, were discarded as spurious modes. The reiterated set of eigenvalues for $\omega_{2D} = 0.1$ and $Re_{2D} = 1000$ may be taken from figure 6.1, where only eigenvalues with $\alpha_{2D,i} < 5$ are shown in order to distinguish the Tollmien–Schlichting (TS) $\alpha_{2D,TS} = 0.19983 + 0.074993\,i$ visually.
The goal now is to obtain a 3D mode with oblique growth mechanics as derived in (5.20) and (5.25). For this, the TS mode is chosen as the least stable of the set in figure 6.1. The 2D parameters $\omega_{2D} = 0.1$ and $Re_{2D} = 1000$ are selected carefully to obtain 3D modes with moderate growth rates in spanwise direction. As can be deduced from (5.25), β_i in general changes signs depending on whether ϕ is larger or smaller than unity. The interesting case certainly occurs for $\phi < 1$, as then the sign of β_i is negative, which corresponds to modes

	3D wave characteristics
streamwise wavelength λ_x	11.00
spanwise wavelength λ_z	31.12
propagation angle θ_p	19.47°
critical angle θ_{cr}	21.94°

Table 6.2: 3D wave characteristics for transformed 3D mode given in table 6.1

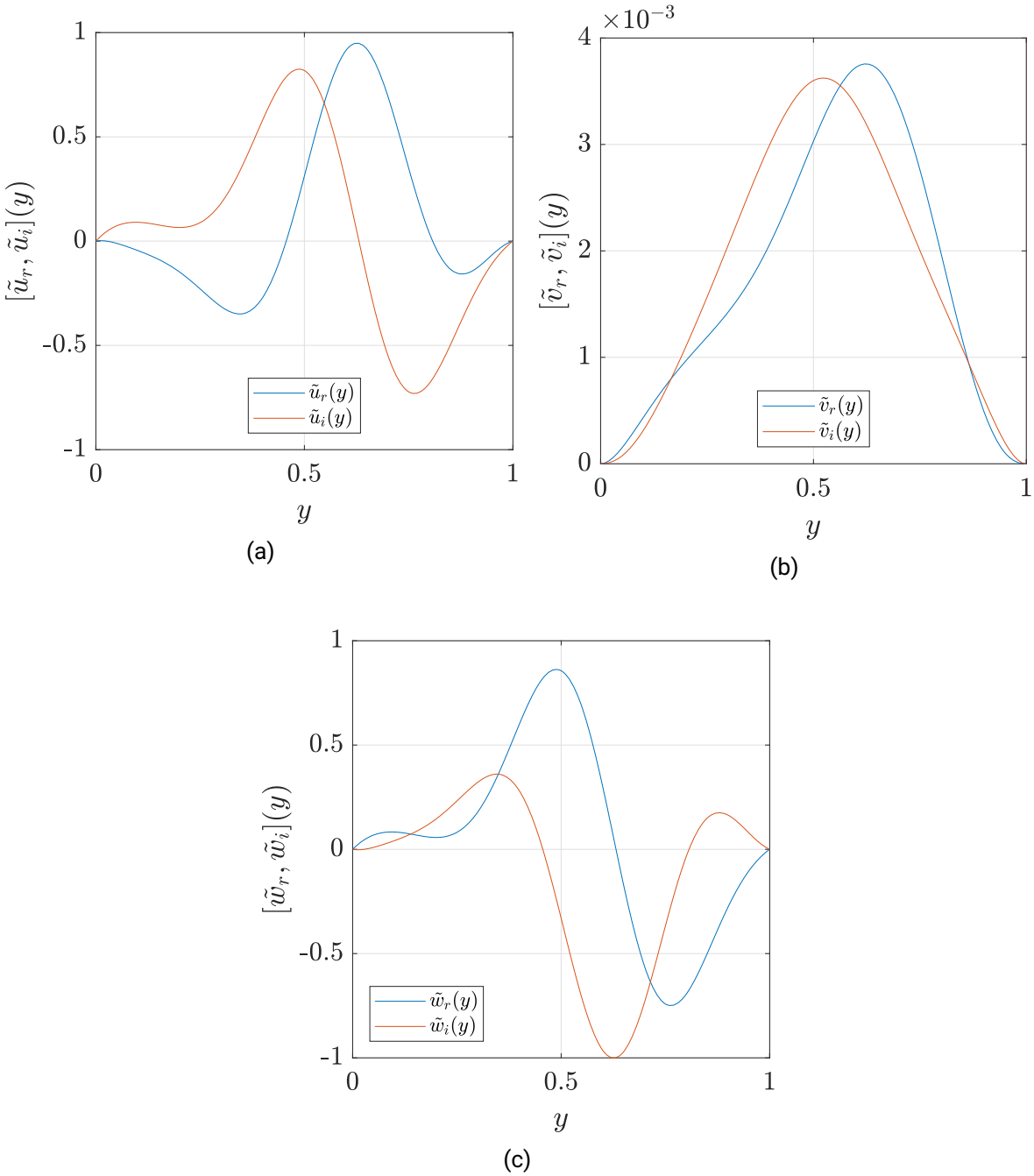

Figure 6.2: Amplitudes of eigenfunctions $\tilde{u}(y)$ (a), $\tilde{v}(y)$ (b) and $\tilde{w}(y)$ (c) arising for a transformation of the 2D parameter set in table 6.1, separated into real and imaginary parts.

growing in spanwise direction, whereas decay in streamwise direction is maintained as α scales inversely with ϕ and does not change its sign. This becomes apparent in numbers when transforming the presented 2D mode according to (5.20) and (5.25) to yield the 3D parameter set given in table 6.1. The Reynolds number ratio $\phi = 0.35$ is chosen to produce moderate spanwise growth rates β_i and a sufficiently small spanwise wavelength $\lambda_z = 2\,\pi/\beta_r$. Furthermore, the resulting 3D Reynolds number $Re_{3D} = 350$ is roughly at which PCF is capable of transitioning, featuring remarkable oblique laminar-turbulent patterns as was laid out in the introduction chapter. Specific 3D wave characteristics may be taken from table 6.2 and will be discussed in subsection 6.2.
The 3D eigenfunctions corresponding to the transformed 3D mode in table 6.1 are given in figure 6.2. As can be seen, the eigenfunctions satisfy the BC in (2.56) perfectly, which in turn legitimates the novel transformation performed with a Reynolds number ratio $\phi < 1$. With this, the novel oblique modes are formally derived and will be validated below.

6.2 Numerical method and boundary conditions

In the now following subsections the attempt is made to validate that the oblique modes in PCF are maintained in the entire flow field when solving the dimensionless NSE (2.30) in a DNS upon introducing the 3D perturbations into the flow domain over the respective boundaries in stream- and spanwise directions. For this, the highly parallel nek5000 code (Fischer et al., 2008) based on spectral element method (SEM) is employed. SEM based codes unite low numerical dissipation and dispersion, which spectral methods are known for, with geometric advantages of finite element method (FEM). As such, SEM codes are commonly used for performing DNS of stability simulations.
The numerical domain consists of E hexahedral elements with $[L_x, L_y, L_z]$ labeling the box dimensions. The solutions are computed in terms of tensor products of Lagrange polynomials with order N. In the present chapter, the order was set to $N = 7$ providing a good compromise between numerical precision and computing expenses. The polynomials are based on $N + 1$ Gauss–Lobatto–Legendre (GLL) quadrature points in every element and every Cartesian direction, equalling to a total number of $E \cdot (N + 1)^3$ nodal points for the entire domain. The implemented $P_N - P_N$ solver, which represents approaches for the discretization and decoupling of the velocity-pressure system in the NSE described by Otero et al. (2019), is used as recommended by the developers. Time integration of the momentum equation is conducted with a semi-implicit second order backward differentiation formula and extrapolation (BDF2/EXT2) scheme, which is chosen for its numerical stability.

The physical domain ranges from $L_x = 10h$, $L_y = h$ and $L_z = 15h$, where the dimensions of the domain are tailored around the wavelength of the mode described in tables 6.1 and 6.2 as well as the spanwise growth rate of the respective perturbation modes. In order to account for the required accuracy of stability calculations, the residual tolerance for both velocity and pressure computation were set to machine accuracy, i.e. $\delta = 10^{-15}$. The simulations were performed non-dimensionally, where non-dimensionalization is conducted with the upper wall-velocity U_w and the channel height h. The target Courant–-Friedrichs–-Lewy (CFL) number is set to 0.5 to ensure a good time resolution.

The initial condition is given as the non-dimensional unperturbed PCF

$$(U, V, W)^T_{t=0} = (y, 0, 0)^T. \tag{6.2}$$

The BC deserve extended discussion due to focus on spatially developing perturbations in both the stream- and the spanwise direction. Where usually periodic BC are set on the boundaries facing in spanwise direction, time-dependent Dirichlet BC need to be set to account for growth in spanwise direction as described in (5.25).
At $y = 0$ no-slip rigid wall BC were employed, while at $y = 1$ the upper wall-velocity was set as a Dirichlet BC. In order to introduce perturbations over the boundaries, a time-dependent Dirichlet BC is used at $x = 0$ as well as $z = L_z$ for the velocities, where the BC read

$$\begin{aligned}
(U(y),0,0)^T + \epsilon(u,v,w)^T|_{x=0} &= (y,0,0) + \epsilon\left[(\tilde{u}_r,\tilde{v}_r,\tilde{w}_r)^T(y)\ \cos(\beta_i z - \omega t)\right. \\
&\quad - \left.(\tilde{u}_i,\tilde{v}_i,\tilde{w}_i)^T(y)\ \sin(\beta_i z - \omega t)\, e^{-\beta_r z}\right], \\
(U(y),0,0)^T + \epsilon(u,v,w)^T|_{z=L_z} &= (y,0,0) + \epsilon\left[(\tilde{u}_r,\tilde{v}_r,\tilde{w}_r)^T(y)\ \cos(\alpha_i x + \beta_i L_z - \omega t)\right. \\
&\quad - \left.(\tilde{u}_i,\tilde{v}_i,\tilde{w}_i)^T(y)\ \sin(\alpha_i x + \beta_i L_z - \omega t)\, e^{-\alpha_r x - \beta_r L_z}\right],
\end{aligned} \tag{6.3}$$

where $(u, v, w)^T$ denote the perturbation velocities while $(\tilde{u}, \tilde{v}, \tilde{w})^T$ stand for the eigenfunctions calculated and depicted in figure 6.2. Furthermore, ϵ denotes the maximum amplitude of the perturbation velocity field, where $\epsilon = 1$ yields the maximum amplitude to be equal to the non-dimensional upper wall-velocity $u(y = L_y) = 1$.
For the remaining two boundaries at $x = L_x$ and $z = 0$, open BC of the type

$$[-p\boldsymbol{I} + \nu(\Delta \boldsymbol{u})] \cdot \boldsymbol{n} = 0, \tag{6.4}$$

are utilized.
The motivation to employ time-dependent Dirichlet BC at $z = L_x$, and not at $z = 0$, as done in streamwise direction, stems from the growth mechanics of modes as derived in section 5.2, specifically the spanwise growth rate β_i derived in (5.21). As elaborated, the sign of the spanwise growth rate β_i depends on the choice of the Reynolds number ratio ϕ as well as the sign of $\alpha_{2D,i}$. For PCF, the 2D spatial eigenvalue problem yields stable modes exclusively and therefore provide positive signs to (5.21). Hence, when applying $\phi < 1$, modes will grow in pure spanwise direction after transformation to 3D whereas decay in streamwise direction is maintained nevertheless. In order to resolve the wave nature in spanwise direction, the box dimension L_z should be sufficiently large, which in turn yields a growth in spanwise direction of

$$\Gamma = \frac{e^{-\beta_i L_z}}{e^{-\beta_i 0}}, \tag{6.5}$$

where Γ denotes the amplification factor across the entire spanwise direction. If the perturbations at $z = L_z$ are to remain in the linear regime, i.e. $(v(x, y, z)) \ll 1$, the respective perturbation field consequently will be multiple magnitudes of order smaller at $z = 0$. Setting Dirichlet BC at $z = L_z$ therefore ensures sufficiently large values at the boundary while also giving insight to an interesting physical question:
(i) do we observe the emergence of modes in the entire flow field, which experience exponential growth $\exp(-\beta_r z)$ in spanwise direction such that the BC at $z = L_z$ are matched?
(ii) do we observe the emergence of modes in the entire flow field, which in a broader sense adopt the 3D parameters ensuing from the extended Squire's transformation in section 5.2?

6.3 DNS Results

In this section, the DNS results verifying oblique modes for PCF is presented in accordance with the method and computational box described in the previous section. Relevant wave characteristics may be taken from table 6.2. The spanwise wavelength is $\lambda_z = 31.12$, corresponding to roughly twice the length of the computational box in spanwise direction. As can be deduced, the perturbation wave propagates at an angle of $\theta_p = 19.47°$ in the x-z-plane relative to pure streamwise direction.
The direction of neutral stability is given by $\theta_{cr} = 21.94°$. As the wave propagates at a subcritical angle, dampening in streamwise direction outweighs growth in spanwise direction due to which the wave decays in the direction of propagation, as is visualized in figure 5.1. Yet, it is interesting to study the decay and growth mechanics of these new oblique modes. The negative β_i signifies that the global perturbation mode grows in its spanwise direction and this for any angle $\theta > \theta_{cr}$. Therefore, it depends on the angle of view whether the observer sees growth or decay. It appears entirely plausible according to this that formerly 2D stable modes become unstable in 3D when moving in directions $\theta > \theta_{cr}$.
Figure 6.3 displays the three perturbation velocity components $u(x)$, $v(x)$ and $w(x)$ at fixed wall-normal coordinate $y = 0.5 = L_y/2$ and spanwise coordinate $z = 5 = L_z/3$ both from DNS and analytical results. The z-coordinate in particular is chosen to be far away from the boundary at $z = L_z$, as there the analytically derived eigenfunctions are set as the BC. The motivation, thus, is to show that even at large distance from this particular boundary, the flow adapts to the solution elsewhere in the flow as well. The analytical results are plotted alongside the results obtained from the DNS. It can be seen that the DNS results match the theoretical eigenfunctions almost perfectly. Slight deviations can be observed at the outflow boundary at $x = 20 = L_x$, which is due to the natural BC (6.4). Nevertheless, the numerical results plotted in streamwise directions suggest validates the predicted novel oblique 3D perturbations.
The results in spanwise direction are plotted in figures 6.4 - 6.6, in (a) linear and in (b) semi-logarithmic scaling. While the results in Cartesian coordinates show good agreement for all three perturbation velocity components at large z, the actual growth rate is best extracted from figures 6.4b, 6.5b and 6.6b. Close to the boundary $z = L_z$, where the analytical eigenfunctions are set as a BC in accordance with (6.3), the DNS results agree very well both in slope as well as in phase with the theorized new oblique modes. For $u(z)$, the analytical perturbation field suggests change of sign at $z \approx 10.45$, which is also replicated by the DNS. Only in the vicinity of the natural BC (6.4) at $z = 0$ do the numerical results deviate from the analytical prediction, which is likely due to non-ideal outflow at this boundary. As described in (6.3), the upper BC at $z = L_z$ is a time-dependent Dirichlet BC where the analytical solutions for the temporal development of the perturbation velocity field is assumed. In figure 6.7, the flow quickly adjusts itself so that the theoretically predicted perturbation velocity field is adapted and, importantly, the BC $z = L_z$ is matched equally once the simulation becomes stationary.
Despite being linearly stable at all Reynolds numbers, the oblique growth mechanism notably induces global growth of the perturbation field in spanwise direction, despite perturbation waves in PCF decaying in the direction of propagation. Thus, with the presently derived modes, linear stability theory (LST) must be reassessed by taking into account those modes, which are not only 3D in their direction of propagation but also in their growth vector.

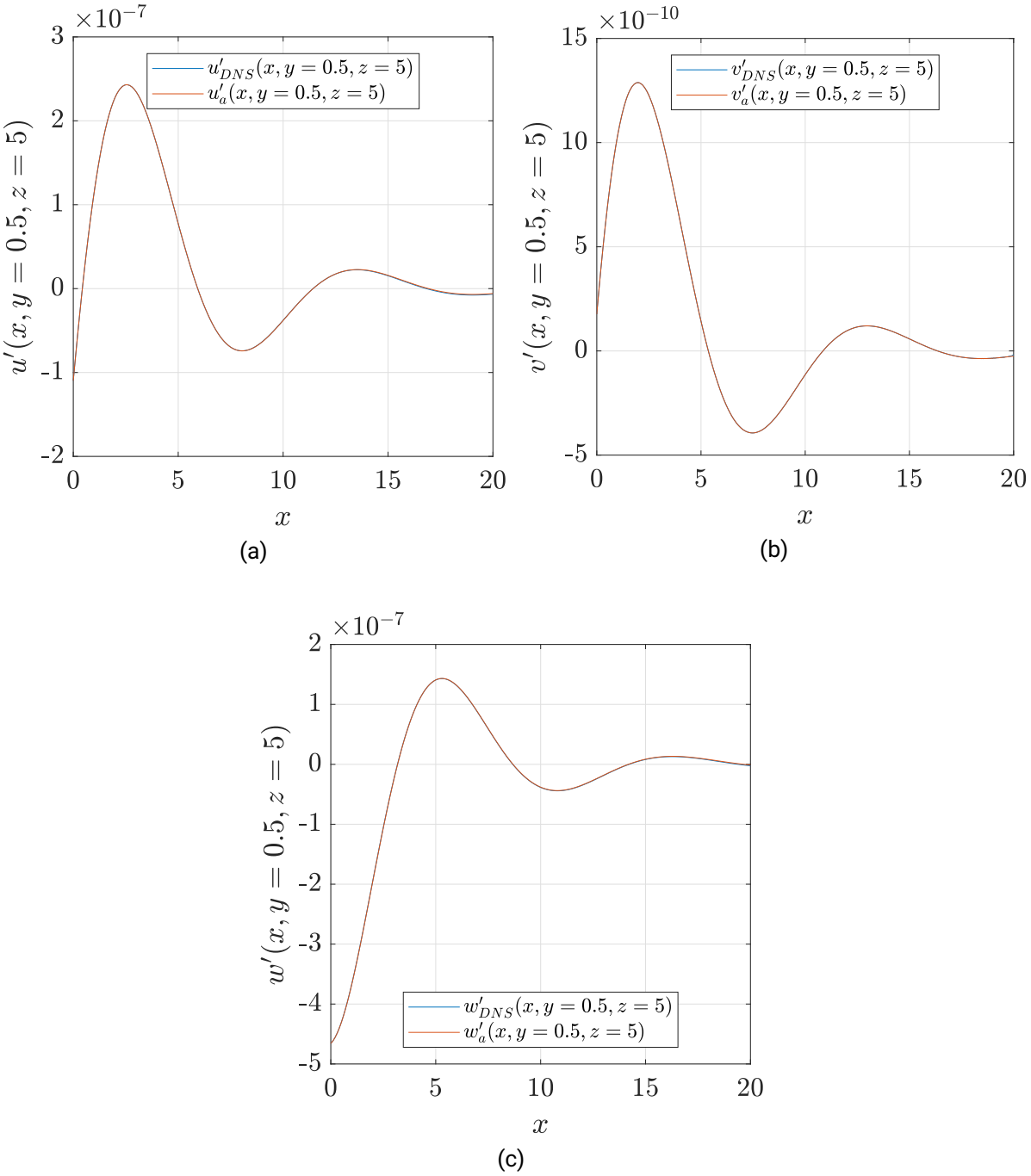

Figure 6.3: Perturbation velocity components $u(x, y = 0.5, z = 5)$ (a), $v(x, y = 0.5, z = 5)$ (b) and $w(x, y = 0.5, z = 5)$ (c) displayed in streamwise direction at $y = 0.5$ and $z = 5$ after $t = 200 \approx 9T$, where $T = 2\pi/\omega$, i.e. one period. The index 'a' gives the analytical results, the index 'DNS' gives the results simulated with the nek5000 SEM code.

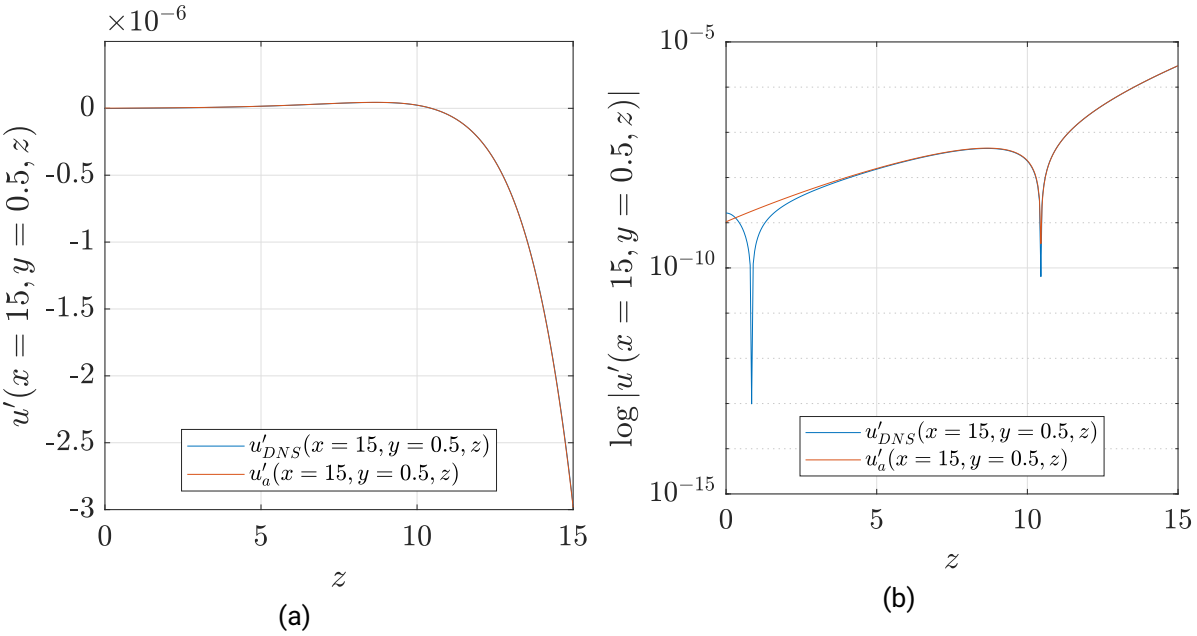

Figure 6.4: Streamwise velocity component $u'(x = 15, y = 0.5, z)$ in Cartesian (a) and semi-logarithmic coordinates (b) displayed in spanwise direction at $y = 0.5$ and $x = 15$ after $t = 200 \approx 9T$, where $T = 2\pi/\omega$, i.e. one period. The index 'a' gives the analytical results, the index 'DNS' gives the results simulated with the nek5000 SEM code.

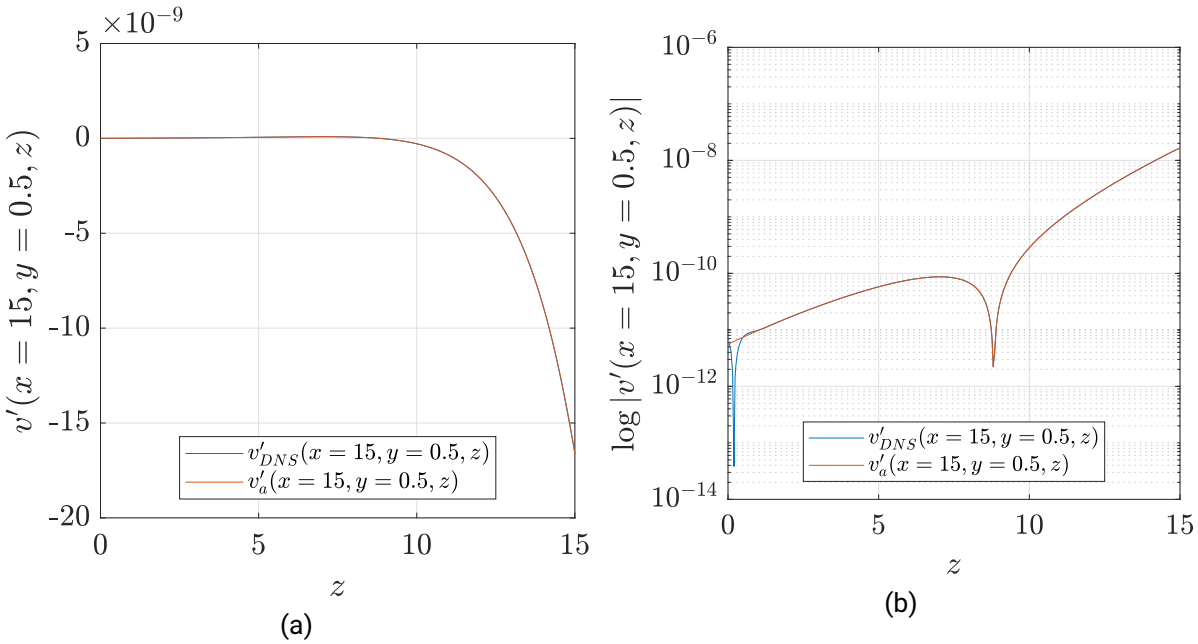

Figure 6.5: Wall-normal velocity component $v(x = 15, y = 0.5, z)$ in (a) linear and (b) semi-logarithmic scaling displayed in spanwise direction at $y = 0.5$ and $x = 15$ after $t = 200 \approx 9T$, where $T = 2\pi/\omega$, i.e. one period. The index 'a' gives the analytical results, the index 'DNS' gives the result simulated with the nek5000 SEM code.

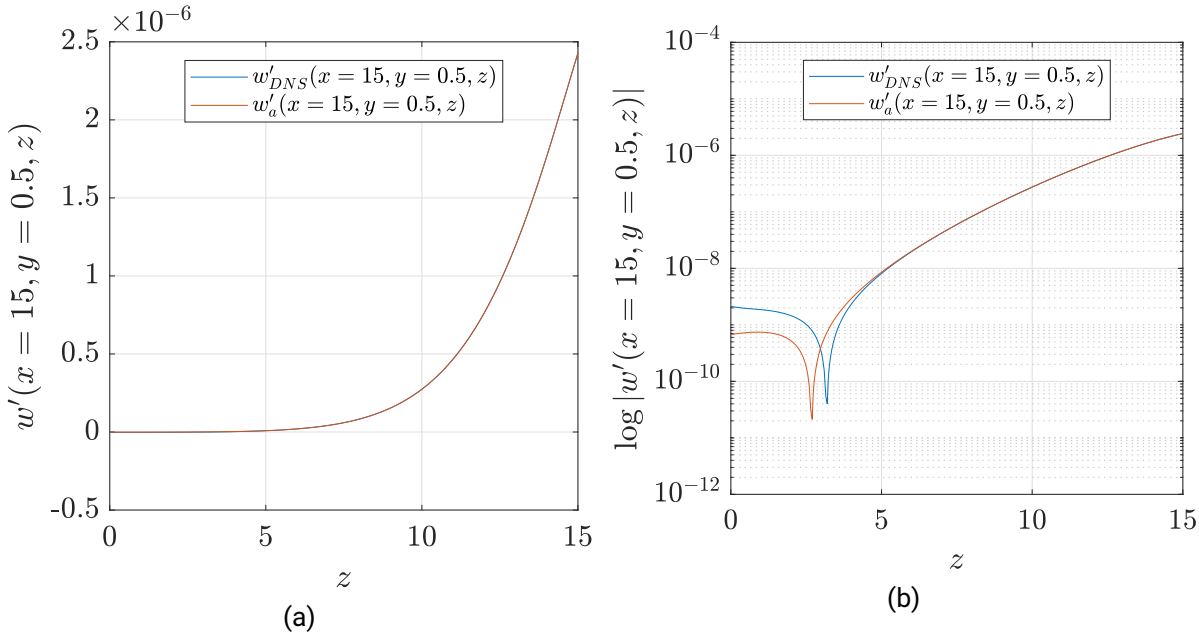

Figure 6.6: Spanwise velocity component $w'(x = 15, y = 0.5, z)$ in (a) linear and (b) semi-logarithmic scaling displayed in spanwise direction at $y = 0.5$ and $x = 15$ after $t = 200 \approx 9T$, where $T = 2\pi/\omega$, i.e. one period. The index 'a' gives the analytical results, the index 'DNS' gives the result simulated with the nek5000 SEM code.

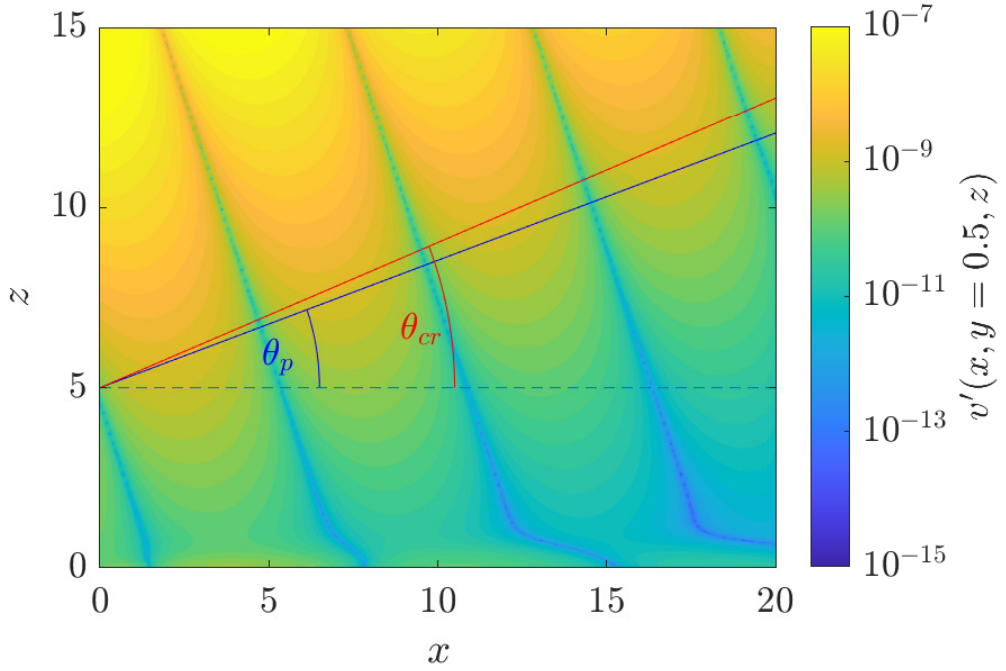

Figure 6.7: 2D contour plot of the wall-normal perturbation velocity component $v(x, y = 0.5, z)$ at half channel height $y = 0.5$ after $t = 200 \approx 9T$, where $T = 2\pi/\omega$, i.e. one period, with the propagation angle θ_p and critical angle θ_{cr} as defined in (5.26) and (5.28).

6.4 Summary

In chapter 5, Squire's transformation for parallel flows is extended by a transformation for 3D spatial oblique modes with spanwise amplification. For this, the invariance transformation of the 2D OSE to 3D OSE is not performed with β as the group parameter, as is done classically in Squire's transformation, but with the 3D to 2D Reynolds number ratio ϕ. Importantly, β is now complex, which was proven to be a necessity in order to allow for a non-trivial symmetry transformation of the OSE parameters. As such, growth of modes in spanwise direction is now a possibility by yielding $\phi < 1$, even when decay is exhibited in streamwise direction. These new oblique 3D modes were then investigated for PCF in the present chapter 6. First, 2D modes at $Re_{2D} = 1000$ were transformed with the newly derived transformation schemes to a lower 3D Reynolds number of $Re_{3D} = 350$, which indeed yielded spanwise growth of the ensuing 3D modes. The neutral stability line is at an angle of $\theta_{cr} = 21.94°$. Though their simulations were conducted with finite amplitude perturbations, a similar angle of $\theta = 24°$ at the same 3D Reynolds number is observed in Tuckerman and Barkley (2011). Moreover, they observe a distance between successive turbulent bands of $\lambda = 40$, which is not too far off the spanwise wavelength of $\lambda_z = 31.12$ calculated for the 3D oblique wave presented in table 6.2.
We thus obtain a new set of oblique modes with growth and decay mechanisms not only in stream- but also in spanwise direction. In the context of replicating these modes in a numerical experiment, a complex β prohibits periodic BC in spanwise direction. To deal with this, the BC usually applied in spatial stability DNS in streamwise directions, i.e. setting the derived eigenfunctions for the perturbations velocity $\boldsymbol{u'}(x, y, z, t)$ as time-dependent Dirichlet BC at $x = 0$, were also set in streamwise direction at $z = L_z$. At the opposite boundaries, natural BC were implemented to allow for a smooth outflow at $x = L_x$ and inflow at $z = 0$ respectively. The corresponding DNS of PCF superposed by the derived novel 3D oblique mode revealed that the flow field emerging is exactly the one required to match the time-dependent Dirichlet BC at $x = 0$ and $z = L_z$. The natural BC led to slight errors in the vicinity of the respective boundaries, which implies that possibly a different class of BC is required to reduce the errors at the respective in- and outflow.
In the present chapter, it was shown that indeed modifying Squire's transformation by a new group parameter ϕ leads to a new class of oblique 3D modes with growth in spanwise direction even for flow that classically see decay in streamwise direction at any Reynolds number. This result raises the question on the applicability of Squire's theorem on spatial stability problems. In classical LST, the critical Reynolds number does not depend on whether the temporal or the spatial problem is investigated. The current new theory, however, suggests that in the spatial stability problem 2D modes may be transformed with $\phi < 1$, i.e. to $Re_{3D} < Re_{2D}$, thus allowing for the possibility of a lower critical 3D Reynolds number.

7 Conclusion

In the introductory words of this dissertation, the goal was set out to uncover links between large-scale turbulent structures and the laminar-turbulent transition process by revisiting linear stability analysis (LSA) for the asymptotic suction boundary layer (ASBL) and plane Couette flow (PCF). Until today the origin of such turbulent superstructures is not clarified satisfactorily, while it appears quite plausible that prominent structures in turbulent flows could originate from distinctive modes in the linear stability problem, which share features of superstructures such as elongation in streamwise direction and an extent in the order of the characteristic length scales of the flow problem.

The dissertation is commenced by a classical LSA of the ASBL, for which the modified Orr–Sommerfeld equation (mOSE) is solvable in terms of generalized hypergeometric functions. A first important result is the correction of the critical Reynolds number to $Re_{cr} \approx 54378.62032$, which is a sizable improvement when compared to the previously accepted critical Reynolds number $Re_{cr,old} = 54382$. The asymptotic analysis of the ensuing algebraic eigenvalue problem (EVP) for temporal stability, which in common literature has been primarily omitted for discrete methods, further disclosed a remarkable dependence of streamwise elongation on the Reynolds number in the zero limit of the streamwise wave number α and the infinite limit of the Reynolds number Re, in that perturbations of small wave numbers may only exist in the distinguished limit $Re_\alpha = Re\alpha$, where $\alpha \to 0$ and $Re \to \infty$ with $Re = O(\alpha^{-1})$. It turned out that $Re_\alpha \approx 0.81491$ represents a lower bound below which the algebraic EVP yields no solutions, thus representing an upper bound for the streamwise elongation of perturbations. Remarkably, this finding coincides with observations in turbulent wall-bounded shear flows, such as channel flow, and could even be generalized to any wall-bounded shear flow via asymptotic analysis of the Orr–Sommerfeld equation (OSE) performed in above mentioned distinguished limit. It further became apparent that for waves corresponding to modes in the distinguished limit, the viscous part of the perturbation velocity component v_{vis} persists furthest into the far-field. Correspondingly, these waves by virtue of small streamwise wave numbers α have very large streamwise wavelengths λ_x, which further attributes to possible links between the distinguished limit and large-scale structures in the ASBL.
The spatial stability analysis revealed a unique solution branching for continuous modes, yielding a positive and negative branch. Interestingly, the positive solution branch yields unstable modes for $\alpha < 0.5$, which seems to be the first case of unstable continuous modes existing in wall-bounded shear flows to date. These relatively low streamwise wave numbers again correspond to comparatively large λ_x and strongly resemble free-stream turbulence (FST), which is supported by the fast Fourier transformation (FFT) of a typical unstable continuous eigenfunction in wall-normal direction.
While transpiration in form of suction stabilizes the ASBL, there are notions in literature of transpiration leading to destabilization, in particular for flows bounded between two walls.

Hence, a classical flow bounded by two walls, PCF, is investigated regarding the influence of transpiration on linear stability, which is exceptionally interesting as PCF is known to be linearly stable for all Reynolds numbers. Indeed, a minimal transpiration Reynolds number of roughly $Re_{V,min} \approx 6.71$ seems to be the threshold above which instabilities begin to occur. The critical Reynolds number $Re_{cr} = 668350.49152$, however, corresponds to a transpiration Reynolds number of $Re_{V,cr} = 9.79923$.
A surprising discovery again is contributed to asymptotic analysis, concretely in the infinite limit for Re_V. It is found that by redefining the Reynolds number and introducing specific coordinate and parameter transformations, plane Couette flow with transpiration (PCFT) may be transformed to the ASBL. This is convenient, as the corresponding algebraic EVP for the ASBL is simpler than the corresponding equations for PCFT, which enables stability analysis for $Re_V \to \infty$ by rigorous transformation to the ASBL and subsequent utilization of the readily derived stability equations. The projection of the neutral stability surface to the Re_V-Re-plane shows that the inverted slope of the projected surface for large Re_V takes a value very close to the previously mentioned critical Reynolds number for the ASBL, which by its definition corresponds to the newly introduced Reynolds number of PCFT for the transformation.
Lastly, a novel extension of Squire's transformation for the spatial stability problem thematically stemming from applying Lie symmetry theory to the parameter space of the OSE reveals the necessity of introducing complex spanwise wave number $\beta in \mathbb{C}$ in addition to the complex streamwise wave number $\alpha in \mathbb{C}$, which in turn corresponds to oblique growth mechanisms in the x-z-plane in view of the spatial growth rates α_i and β_i. It is derived that linearly stable two-dimensional (2D) flows are transformed to three-dimensional (3D) flows with decay in streamwise direction and growth in spanwise direction of the perturbation velocity field. For linearly unstable 2D flows, in turn, it is shown that subcritical 3D oblique modes can be constructed with $Re_{3D,cr} < Re_{2D,cr}$, contradicting Squire's theorem. The novel framework is applied to PCF subsequently and PCF superposed by oblique 3D modes obtained by the extended Squire's transformation is finally simulated numerically with a spectral element solver. The numerical results disclosed very good agreement with the predicted theoretical velocity fields. Moreover, the stripe patterns arising for such superposition grow in spanwise direction and are indeed reminiscent of laminar-turbulent stripe patterns in transitional PCF. With this, yet another link between linear modes and large-scale structures is possibly established.

The results presented in this dissertation certainly do not conclude the potential linear stability theory (LST) offers for seeking the origins of turbulent superstructures. It remains interesting to see if the modes derived for the distinguished limit for the ASBL indeed form the skeleton of structures evolving into large-scale turbulent structures elongated in streamwise direction. Whether unstable spatial continuous modes in fact provide a plausible model for FST also remains to be seen and should certainly be studied with suitable numerical experiments.
It is shown that transpiration destabilizes PCF, which is bounded by two parallel walls. One can imagine that perturbations in classical PCF, for which the velocity vector points in the wall-normal direction, represent wall-normal cross-flows and possibly shed new light on the transitional process of PCF. Certainly, PCF with transpiration should be studied both numerically and experimentally in order to further understand how transition and transpiration are connected.
The extension of Squire's transformation represents a remarkable addition to LST, accounting for modes which grow or decay not only in stream- but also in spanwise direction. Intuitively, it seems plausible that such modes should exist, but LST to date has not provided a framework to

analyze the implications of oblique modes for laminar-turbulent transition and oblique stripe patterns, which for instance demonstrably exist for transitioning LST. While as a start the validity of oblique modes were verified in numerical simulations for PCF, it remains interesting how the oblique modes evolve into weakly non-linear and non-linear regimes and whether they indeed could be responsible for superstructures occurring for PCF.
In summary, it should not remain unmentioned that the framework of modal LST is not yet exhausted at all and should never be entirely neglected in view of nonmodal and nonlinear theories. The present author motivates further research in the direction this dissertation attempted to sketch and establish. While numerical and experimental fluid mechanics increasingly overshadow analytical methods, the present dissertation shall also demonstrate that fluid mechanics is still governed by equations and theoretical principles. Ultimately, the extension and comprehension of the existing set of stability equations are guaranteed to further expand the understanding of laminar-turbulent transition and turbulent superstructures.

Bibliography

Acheson, D. (1990). Elementary Fluid Dynamics. Clarendon Press.

Ahlers, G., Grossmann, S., and Lohse, D. (2009). "Heat transfer and large scale dynamics in turbulent Rayleigh-Bénard convection." In: Reviews of modern physics 81.2, p. 503.

Baldwin, P. (1970). "The stability of the asymptotic suction boundary layer profile." In: Mathematika 17.2, pp. 206–242.

Barkley, D. and Tuckerman, L. S. (2005). "Computational study of turbulent laminar patterns in Couette flow." In: Physical review letters 94.1, p. 014502.

Barkley, D. and Tuckerman, L. S. (1999). "Stability analysis of perturbed plane Couette flow." In: Physics of Fluids 11.5, pp. 1187–1195.

Batchelor, C. K. and Batchelor, G. (2000). An introduction to fluid dynamics. Cambridge university press.

Benjamin, T. B. (1961). "The development of three-dimensional disturbances in an unstable film of liquid flowing down an inclined plane." In: Journal of Fluid Mechanics 10.3, pp. 401–419. DOI: 10.1017/S0022112061001001.

Bertolotti, F. P., Herbert, T., and Spalart, P. (1992). "Linear and nonlinear stability of the Blasius boundary layer." In: Journal of fluid mechanics 242, pp. 441–474.

Bethe, H. (1931). "Eigenwerte und Eigenfunktionen der linearen Atomkette." In: Z. Phys 71.205, p. 13.

Blasius, H. (1907). Grenzschichten in Flüssigkeiten mit kleiner Reibung. Druck von BG Teubner.

Bluman, G. W. and Kumei, S. (2013). Symmetries and differential equations. Vol. 81. Springer Science & Business Media.

Bodenschatz, E., Pesch, W., and Ahlers, G. (2000). "Recent developments in Rayleigh-Bénard convection." In: Annual review of fluid mechanics 32.1, pp. 709–778.

Boltzmann, L. (1872). Weitere Studien über das Wärmegleichgewicht unter Gasmolekülen. k. und k. Hof- und Staatsdr.

Canuto, C., Hussaini, M. Y., Quarteroni, A., Thomas Jr, A., et al. (2012). Spectral methods in fluid dynamics. Springer Science & Business Media.

Caviglia, G. and Morro, A. (1989). "Conservation laws for incompressible fluids." In: International Journal of Ma 12.2, pp. 377–384.

Chagelishvili, G., Khujadze, G., Foysi, H., and Oberlack, M. (2014). "Spanwise reflection symmetry breaking and turbulence control: plane Couette flow." In: Journal of fluid mechanics 745, pp. 300–320.

Chemloul, N.-E. S. (2020). Dimensional Analysis and Similarity in Fluid Mechanics. John Wiley & Sons.

Chiarulli, P. and Freeman, J. C. (1948). Stability of the Boundary Layer. Tech. Rep no. F-TR-1197-IA. Headquarters Air Materiel Command, Dayton.

Coles, D. (1965). "Transition in circular Couette flow." In: Journal of Fluid Mechanics 21.3, pp. 385–425.

Daviaud, F., Hegseth, J., and Bergé, P. (1992). "Subcritical transition to turbulence in plane Couette flow." In: Physical review letters 69.17, p. 2511.

Dempsey, L. J. and Walton, A. G. (2017). "Vortex/Tollmien–Schlichting wave interaction states in the asymptotic suction boundary layer." In: The Quarterly Journal of Mechanics and Applied Mathematics 70.3, pp. 187–213.

Duguet, Y. and Schlatter, P. (2013). "Oblique laminar-turbulent interfaces in plane shear flows." In: Physical review letters 110.3, p. 034502.

Ferro, M., Fallenius, B. E., and Fransson, J. H. (2021). "Experimental study on turbulent asymptotic suction boundary layers." In: Journal of Fluid Mechanics 915.

Fischer, P. F., Lottes, J. W., and Kerkemeier, S. G. (2008). nek5000 web page. (accessed: 15.04.2022) http://nek5000.mcs.anl.gov.

Floryan, J. (2003). "Wall-transpiration-induced instabilities in plane Couette flow." In: Journal of Fluid Mechanics 488, pp. 151–188.

Fransson, J. H. and Alfredsson, P. (2003). "On the disturbance growth in an asymptotic suction boundary layer." In: Journal of Fluid Mechanics 482, pp. 51–90.

Fukudome, K., Tsukahara, T., and Ogami, Y. (2018). "Heat and momentum transfer of turbulent stripe in transitional-regime plane Couette flow." In: International Journal of Advances in Engineering Sciences 10.4, pp. 291–298.

Gallet, B., Doering, C. R., and Spiegel, E. A. (2010). "Destabilizing Taylor–Couette flow with suction." In: Physics of Fluids 22.3, p. 034105.

Gebler, T., Plümacher, D., Kahle, J., and Oberlack, M. (2021). "Algebraic stability modes in rotational shear flow." In: Fluid Dynamics Research 53.6, p. 065509. DOI: 10.1088/1873-7005/ac44f9.

Getling, A. V. (1998). Rayleigh-Bénard convection: structures and dynamics. Vol. 11. World Scientific.

Griffith, A. and Meredith, F. (1936). "The possible improvement in aircraft performance due to the use of boundary layer suction." In: Royal Aircraft Establishment Report No. E 3501, p. 12.

Grosch, C. E. and Salwen, H. (1978). "The continuous spectrum of the Orr-Sommerfeld equation. Part 1. The spectrum and the eigenfunctions." In: Journal of Fluid Mechanics 87.1, pp. 33–54.

Hocking, L. (1975). "Non-linear instability of the asymptotic suction velocity profile." In: The Quarterly Journal of Mechanics and Applied Mathematics 28.3, pp. 341–353.

Hughes, T. and Reid, W. (1965). "On the stability of the asymptotic suction boundary-layer profile." In: Journal of Fluid Mechanics 23.4, pp. 715–735.

Hutchins, N. and Marusic, I. (2007). “Evidence of very long meandering features in the logarithmic region of turbulent boundary layers.” In: Journal of Fluid Mechanics 579, pp. 1–28.

Jerome, J. J. S. and Chomaz, J.-M. (2014). “Extended Squire’s transformation and its consequences for transient growth in a confined shear flow.” In: Journal of fluid mechanics 744, pp. 430–456.

Karniadakis, G., Beskok, A., and Aluru, N. (2006). Microflows and nanoflows: fundamentals and simulation. Vol. 29. Springer Science & Business Media.

Kelbin, O., Cheviakov, A. F., and Oberlack, M. (2013). “New conservation laws of helically symmetric, plane and rotationally symmetric viscous and inviscid flows.” In: Journal of Fluid Mechanics 721, pp. 340–366.

Kendall, J. (1985). “Experimental study of disturbances produced in a pre-transitional laminar boundary layer by weak freestream turbulence.” In: 18th Fluid Dynamics and Plasmadynamics and Lasers C p. 1695.

Kerswell, R. (2018). “Nonlinear nonmodal stability theory.” In: Annual Review of Fluid Mechanics 50, pp. 319–345.

Khapko, T., Schlatter, P., Duguet, Y., and Henningson, D. S. (2016). “Turbulence collapse in a suction boundary layer.” In: Journal of Fluid Mechanics 795, pp. 356–379.

Kovasznay, L. S., Kibens, V., and Blackwelder, R. F. (1970). “Large-scale motion in the intermittent region of a turbulent boundary layer.” In: Journal of Fluid Mechanics 41.2, pp. 283–325.

Kraheberger, S., Hoyas, S., and Oberlack, M. (2018). “DNS of a turbulent Couette flow at constant wall transpiration up to $Re_\tau = 1000$.” In: Journal of Fluid Mechanics 835, pp. 421–443.

Liao, S. (2003). Beyond perturbation: introduction to the homotopy analysis method. Chapman and Hall/CRC.

Lundbladh, A. and Johansson, A. V. (1991). “Direct simulation of turbulent spots in plane Couette flow.” In: Journal of Fluid Mechanics 229, pp. 499–516.

Mack, L. M. (1976). “A numerical study of the temporal eigenvalue spectrum of the Blasius boundary layer.” In: Journal of Fluid Mechanics 73.3, pp. 497–520.

Mack, L. M. (1977). “Transition and laminar instability.” In: Jet Propulsion Laboratory Publication 78.

Mack, L. M. (1984). Boundary-layer linear stability theory. Tech. rep. California Inst of Tech Pasadena Jet Propulsion Lab.

Messiter, A. (1970). “Boundary-layer flow near the trailing edge of a flat plate.” In: SIAM Journal on Applied Ma 18.1, pp. 241–257.

Mirzayev, J. (2016). “Asymptotic suction boundary layer - Normal and new non-normal modes of stability using symmetry methods.” *Bachelor thesis (unpublished)*. TU Darmstadt, Chair of Fluid Dynamics.

Muller, D. E. (1956). “A method for solving algebraic equations using an automatic computer.” In: Mathematical tables and other aids to computation 10.56, pp. 208–215.

Nagata, M. (1990). “Three-dimensional finite-amplitude solutions in plane Couette flow: bifurcation from infinity.” In: Journal of Fluid Mechanics 217, pp. 519–527.

Nakagawa, H. and Nezu, I. (1981). “Structure of space-time correlations of bursting phenomena in an open-channel flow.” In: Journal of Fluid Mechanics 104, pp. 1–43.

Neiland, V. Y. (1970). “Propagation of perturbations upstream with interaction between a hypersonic flow and a boundary layer.” In: Fluid Dynamics 5.4, pp. 559–566.

Nold, A. and Oberlack, M. (2013). “Symmetry analysis in linear hydrodynamic stability theory: Classical and new modes in linear shear.” In: Physics of Fluids 25.10, p. 104101.

Nold, A., Oberlack, M., and Cheviakov, A. F. (2015). “On new stability modes of plane canonical shear flows using symmetry classification.” In: Journal of Mathematical Physics 56.11, p. 113101.

Oberlack, M., Hoyas, S., Kraheberger, S. V., Alcántara-Ávila, F., and Laux, J. (2022). “Turbulence Statistics of Arbitrary Moments of Wall-Bounded Shear Flows: A Symmetry Approach.” In: Physical Review Letters 128.2, p. 024502.

Oberlack, M. (2001). “A unified approach for symmetries in plane parallel turbulent shear flows.” In: Journal of Fluid Mechanics 427, pp. 299–328.

Olver, F. W., Lozier, D. W., Boisvert, R. F., and Clark, C. W. (2010). NIST handbook of mathematical functions hardl Cambridge university press.

Orr, W. M. (1907). “The stability or instability of the steady motions of a perfect liquid and of a viscous liquid. Part II: A viscous liquid.” In: Proceedings of the Royal Irish Academy. Section A: Mathematical ar JSTOR, pp. 69–138.

Orszag, S. A. and Kells, L. C. (1980). “Transition to turbulence in plane Poiseuille and plane Couette flow.” In: Journal of Fluid Mechanics 96.1, pp. 159–205.

Orszag, S. A. (1971). “Accurate solution of the Orr–Sommerfeld stability equation.” In: Journal of Fluid Mechanics 50.4, pp. 689–703.

Otero, E., Gong, J., Min, M., Fischer, P., Schlatter, P., and Laure, E. (2019). “OpenACC acceleration for the PN–PN-2 algorithm in Nek5000.” In: Journal of Parallel and Distributed Computing 132, pp. 69–78.

Pandey, A., Scheel, J. D., and Schumacher, J. (2018). “Turbulent superstructures in Rayleigh-Bénard convection.” In: Nature communications 9.1, pp. 1–11.

Pope, S. B. and Pope, S. B. (2000). Turbulent flows. Cambridge university press.

Prandtl, L. (1904). “Über Flüssigkeitsbewegung bei sehr kleiner Reibung.” In: Verhandl. III, Internat. Math.-Kong., pp. 484–491.

Prigent, A., Grégoire, G., Chaté, H., Dauchot, O., and Saarloos, W. van (2002). “Large-scale finite-wavelength modulation within turbulent shear flows.” In: Physical review letters 89.1, p. 014501.

Reddy, S. C., Schmid, P. J., and Henningson, D. S. (1993). “Pseudospectra of the Orr–Sommerfeld operator.” In: SIAM Journal on Applied Mathematics 53.1, pp. 15–47.

Reid, W. (1979). “An Exact Solution of the Orr-Sommerfeld Equation for Plane Couette Flow.” In: Studies in Applied Mathematics 61.1, pp. 83–91.

Reynolds, O. (1883). “XXIX. An experimental investigation of the circumstances which determine whether the motion of water shall be direct or sinuous, and of the law of resistance in parallel channels.” In: Philosophical Transactions of the Royal society of London 174, pp. 935–982.

Richards, E. J. and Burge, C. (1943). “An aerofoil designed to give laminar flow over the whole surface with boundary-layer suction.” In.

Romanov, V. A. (1973). “Stability of plane-parallel Couette flow.” In: Functional analysis and its applications 7.2, pp. 137–146.

Schmid, P. J., Henningson, D. S., and Jankowski, D. (2002). “Stability and transition in shear flows. applied mathematical sciences, vol. 142.” In: Appl. Mech. Rev. 55.3, B57–B59.

Schlatter, P. and Örlü, R. (2011). “Turbulent asymptotic suction boundary layers studied by simulation.” In: Journal of Physics: Conference Series. Vol. 318. 2. IOP Publishing, p. 022020.

Schlüter, A., Lortz, D., and Busse, F. (1965). “On the stability of steady finite amplitude convection.” In: Journal of Fluid Mechanics 23.1, pp. 129–144.

Schmid, P. J. (2007). “Nonmodal stability theory.” In: Annu. Rev. Fluid Mech. 39, pp. 129–162.

Schlichting, H. (1933). “Zur Entstehung der Turbulenz bei der Plattenströmung.” In: Nachrichten von der Gesel 1933, pp. 181–208.

Simon, V., Weigand, B., and Gomaa, H. (2017). Dimensional analysis for engineers. Vol. 650. Springer.

Sommerfeld, A. (1908). “Ein Beitrag Zur Hydrodynamischen Erklärung Der Turbulenten Flüssigkeitsbewegungen.” In: Atti Del IV Congresso Internazionale Dei Matematici. Rome, pp. 116–124.

Spurk, J. H. and Aksel, N. (2010). “Strömungslehre: Einführung in die Theorie der Strömungen. 8. Auflage.” In.

Squire, H. B. (1933). “On the stability for three-dimensional disturbances of viscous fluid flow between parallel walls.” In: Proceedings of the Royal Society of London. Series A, Containing Papers of a Mat 142.847, pp. 621–628.

Stewartson, K. and Williams, P. (1969). “Self-induced separation.” In: Proceedings of the Royal Society of Lond 312.1509, pp. 181–206.

Stewartson, K. and Stuart, J. T. (1971). “A non-linear instability theory for a wave system in plane Poiseuille flow.” In: J. Fluid Mech. 48.3, pp. 529–545.

Sun, W., Yalcin, A., and Oberlack, M. (2022). “On the stability of plane Couette flow with constant wall-transpiration.” *(unpublished manuscript)*.

Sun, W. (2020). “Dreidimensionale Stabilitätsanalyse einer ebenen Couette-Strömung mit Wandtranspiration.” *Master thesis (unpublished)*. TU Darmstadt, Chair of Fluid Dynamics.

Thomas, L. (1953). “The stability of plane Poiseuille flow.” In: Physical Review 91.4, p. 780.

Thwaites, B. (1946). “On certain types of boundary-layer flow with continuous surface suction.” In: Aeronautical Research Council Reports Memoranda 2243.

Tilton, N. and Cortelezzi, L. (2006). “The destabilizing effects of wall permeability in channel flows: A linear stability analysis.” In: Physics of Fluids 18.5, p. 051702.

Tillmark, N. and Alfredsson, P. H. (1992). “Experiments on transition in plane Couette flow.” In: Journal of Fluid Mechanics 235, pp. 89–102.

Tollmien, W. (1930). “Über die Entstehung der Turbulenz.” In: Vorträge aus dem Gebiete der Aerodynamik und v Springer, pp. 18–21.

Trefethen, L. N., Trefethen, A. E., Reddy, S. C., and Driscoll, T. A. (1993). “Hydrodynamic stability without eigenvalues.” In: Science 261.5121, pp. 578–584.

Tuckerman, L. S. and Barkley, D. (2011). “Patterns and dynamics in transitional plane Couette flow.” In: Physics of Fluids 23.4, p. 041301.

Turkac, Y. (2019). “Dreidimensionale Stabilitätsanalyse einer asymptotisch abgesaugten Grenzschichtströmung.” *Master thesis (unpublished)*. TU Darmstadt, Chair of Fluid Dynamics.

UN (2015). “Adoption of the Paris agreement.” In: 21st Conference of the Parties, United Nations Framework Cor UNFCCC Paris.

Van Dyke, M. (1975). “Perturbation methods in fluid mechanics/Annotated edition.” In: NASA STI/Recon Technical Report A 75, p. 46926.

Yalcin, A., Turkac, Y., and Oberlack, M. (2021). “On the temporal linear stability of the asymptotic suction boundary layer.” In: Physics of Fluids 33.5, p. 054111.

Yoshioka, S., Fransson, J. H., and Alfredsson, P. H. (2004). “Free stream turbulence induced disturbances in boundary layers with wall suction.” In: Physics of fluids 16.10, pp. 3530–3539.

A Appendix

A.1 Asymptotic expansion for small streamwise wave numbers

The influence of large wavelength perturbations in the streamwise direction is attempted to be understood by an asymptotic analysis for small streamwise wave numbers α. For this we introduce a formal Poincaré-expansion for the eigenvalue ω of the form

$$\omega = \sum_{k=0}^{\infty} \omega_k \, \alpha^k, \tag{A.1}$$

to be employed into the EVP (3.54).
With this, the viscous parameter $\sigma(\omega)_{\alpha,Re}$ may be expanded to

$$\sigma(\omega(\alpha)) = \sqrt{1 - 4iRe\omega_0} + \frac{2iRe(1-\omega_1)}{\sqrt{1-4iRe\omega_0}}\alpha + O(\alpha^2). \tag{A.2}$$

Expanding the parameters of the ${}_2F_3$ generalized hypergeometric function constituting the EVP (3.54) yields

$$\begin{aligned}
\boldsymbol{a_2} &= \begin{pmatrix} \sqrt{\alpha^2+1}+\alpha \\ -\sqrt{\alpha^2+1}+\alpha \end{pmatrix} = \begin{pmatrix} 1+\alpha+O(\alpha^2) \\ -1+\alpha+O(\alpha^2) \end{pmatrix}, \\
\boldsymbol{b_2} &= \begin{pmatrix} 1+2\alpha \\ -\frac{\sigma}{2}+\frac{1}{2}+\alpha \\ \frac{\sigma}{2}+\frac{1}{2}+\alpha \end{pmatrix} = \begin{pmatrix} 1+2\alpha \\ -\frac{1}{2}\sqrt{1-4iRe\omega_0}+\frac{1}{2}+\left(\frac{iRe(\omega_1-1)}{\sqrt{1-4iRe\omega_0}}+1\right)\alpha+O(\alpha^2) \\ \frac{1}{2}\sqrt{1-4iRe\omega_0}+\frac{1}{2}+\left(-\frac{iRe(\omega_1-1)}{\sqrt{1-4iRe\omega_0}}+1\right)\alpha+O(\alpha^2) \end{pmatrix}, \\
\boldsymbol{a_4} &= \begin{pmatrix} \sqrt{\alpha^2+1}+\frac{1}{2}+\frac{\sigma}{2} \\ -\sqrt{\alpha^2+1}+\frac{1}{2}+\frac{\sigma}{2} \end{pmatrix} = \begin{pmatrix} \frac{1}{2}\left(3+\sqrt{1-4iRe\omega_0}\right)+\frac{iRe(1-\omega_1)}{\sqrt{1-4iRe\omega_0}}\alpha+O(\alpha^2) \\ \frac{1}{2}\left(-1+\sqrt{1-4iRe\omega_0}\right)+\frac{iRe(1-\omega_1)}{\sqrt{1-4iRe\omega_0}}\alpha+O(\alpha^2) \end{pmatrix}, \\
\boldsymbol{b_4} &= \begin{pmatrix} 1+\sigma \\ \frac{3}{2}+\frac{\sigma}{2}+\alpha \\ \frac{3}{2}+\frac{\sigma}{2}-\alpha \end{pmatrix} = \begin{pmatrix} 1+\sqrt{1-4iRe\omega_0}+\frac{2iRe(1-\omega_1)}{\sqrt{1-4iRe\omega_0}}\alpha+O(\alpha^2) \\ \frac{1}{2}(3+\sqrt{1-4iRe\omega_0})+\left(1+\frac{iRee(1-\omega_1)}{\sqrt{1-4iRe\omega_0}}\right)\alpha+O(\alpha^2) \\ \frac{1}{2}(3+\sqrt{1-4iRe\omega_0})+\left(-1+\frac{iRe(-1-\omega_1)}{\sqrt{1-4iRe\omega_0}}\right)\alpha+O(\alpha^2) \end{pmatrix}.
\end{aligned} \tag{A.3}$$

Now, only the leading order terms are considered. The first ${}_2F_3$-function then expands into

$$\begin{aligned}
{}_2F_3\left(\begin{matrix}\boldsymbol{a_2}\\ \boldsymbol{b_2}\end{matrix}; -iRe\,\alpha\right) &= \sum_{n=0}^{\infty} \frac{(1)_n\,(-1+\alpha)_n}{(1)_n\,\left(\frac{1}{2}(1-\sigma_0)\right)_n\,\left(\frac{1}{2}(1+\sigma_0)\right)_n}\,\frac{(-iRe\,\alpha)^n}{n!} + O(\alpha^2) \\
&= 1 + \frac{1}{\omega_0}\,\alpha + O(\alpha^2),
\end{aligned} \tag{A.4}$$

with $\sigma_0 = \sqrt{1 - 4iRe\,\omega_0}$.
Clearly, ${}_2F_3\left(\boldsymbol{a_2}, \boldsymbol{b_2}; -iRe\,\alpha\right)$ asymptotically strives towards unity in the leading order. Substituting the parameters a_{4i} and b_{4i} into ${}_2F_3\left(\boldsymbol{a_4}, \boldsymbol{b_4}; -iRe\,\alpha\right)$ yields

$$\begin{aligned} {}_2F_3\left(\begin{matrix}\boldsymbol{a_4}\\ \boldsymbol{b_4}\end{matrix}; -iRe\,\alpha\right) &= \sum_{n=0}^{\infty} \frac{\left(\frac{1}{2}\,(3+\sigma_0)\right)_n \left(\frac{1}{2}\,(-1+\sigma_0)\right)_n}{(1+\sigma_0)_n \left(\frac{1}{2}(3+\sigma_0)\right)_n \left(\frac{1}{2}(3+\sigma_0)\right)_n} \frac{(-iRe\,\alpha)^n}{n!} + O(\alpha) \\ &= 1 + O(\alpha). \end{aligned} \tag{A.5}$$

Analogously, the differentiated hypergeometric functions expand into

$$\begin{aligned} {}_2F_3\left(\begin{matrix}\boldsymbol{a_2+1}\\ \boldsymbol{b_2+1}\end{matrix}; -iRe\,\alpha\right) &= \sum_{n=0}^{\infty} \frac{(2)_n\,(\alpha)_n}{(2)_n \left(\frac{1}{2}(3-\sigma_0)\right)_n \left(\frac{1}{2}(3+\sigma_0)\right)_n} \frac{(-iRe\,\alpha)^n}{n!} + O(\alpha^2) \\ &= 1 + O(\alpha^2), \end{aligned} \tag{A.6}$$

$$\begin{aligned} {}_2F_3\left(\begin{matrix}\boldsymbol{a_4+1}\\ \boldsymbol{b_4+1}\end{matrix}; -iRe\,\alpha\right) &= \sum_{n=0}^{\infty} \frac{\left(\frac{1}{2}\,(5+\sigma_0)\right)_n \left(\frac{1}{2}\,(1+\sigma_0)\right)_n}{(2+\sigma_0)_n \left(\frac{1}{2}(5+\sigma_0)\right)_n \left(\frac{1}{2}(5+\sigma_0)\right)_n} \frac{(-iRe\,\alpha)^n}{n!} + O(\alpha^2) \\ &= 1 + O(\alpha^2). \end{aligned} \tag{A.7}$$

Substituting the leading order of all expansions into the eigenvalue problem in (3.54) results in

$$\mathcal{D}(\omega(\alpha)) = -\frac{1}{2}\left(1 + \sqrt{1 - 4iRe\omega_0}\right) + O(\alpha) = 0, \tag{A.8}$$

which apparently yields no solution for ω_0. As a consequence, the leading order $D(\omega(\alpha))^{O(1)}$ is not equal to zero. An ansatz as suggested in (A.1) therefore is not viable for $\alpha \to 0$. In fact it can be shown analogously that any power series $\omega = \sum_p^P \omega_p\,\alpha^p$ with $p \geq 0 \in \mathbb{R}$ fails.

A.2 Asymptotic expansion for distinguished limit Re_α

In order to expand (3.54) asymptotically in the distinguished limit (3.57), it is necessary to expand each parameter of the ${}_2F_3$ generalized hypergeometric functions given in (3.25):

$$\begin{aligned} \boldsymbol{a_2} &= \begin{pmatrix} \sqrt{\alpha^2+1} + \alpha \\ -\sqrt{\alpha^2+1} + \alpha \end{pmatrix} = \begin{pmatrix} 1 + O(\alpha) \\ -1 + \alpha + O(\alpha^2) \end{pmatrix}, \\ \boldsymbol{b_2} &= \begin{pmatrix} 1 + 2\alpha \\ -\frac{\sigma}{2} + \frac{1}{2} + \alpha \\ \frac{\sigma}{2} + \frac{1}{2} + \alpha \end{pmatrix} = \begin{pmatrix} 1 + 2\alpha \\ -\frac{1}{2}\sigma_0 + \frac{1}{2} + O(\alpha) \\ \frac{1}{2}\sigma_0 + \frac{1}{2} + O(\alpha) \end{pmatrix}, \\ \boldsymbol{a_4} &= \begin{pmatrix} \sqrt{\alpha^2+1} + \frac{1}{2} + \frac{\sigma}{2} \\ -\sqrt{\alpha^2+1} + \frac{1}{2} + \frac{\sigma}{2} \end{pmatrix} = \begin{pmatrix} \frac{1}{2}\,(3+\sigma_0) + O(\alpha) \\ \frac{1}{2}(-1+\sigma_0) + O(\alpha) \end{pmatrix}, \\ \boldsymbol{b_4} &= \begin{pmatrix} 1 + \sigma \\ \frac{3}{2} + \frac{\sigma}{2} + \alpha \\ \frac{3}{2} + \frac{\sigma}{2} - \alpha \end{pmatrix} = \begin{pmatrix} 1 + \sigma_0 + O(\alpha) \\ \frac{1}{2}\,(3+\sigma_0) + O(\alpha) \\ \frac{1}{2}\,(3+\sigma_0) + O(\alpha) \end{pmatrix}, \end{aligned} \tag{A.9}$$

with $\sigma_0 = \sqrt{1 + 4i\,Re_\alpha\,(1-\omega_1)}$. Furthermore, the argument of the ${}_2F_3$-functions is expanded as

$$z(y=0) = -iRe\,\alpha = -iRe_\alpha, \tag{A.10}$$

which in the distinguished limit is now constant.
We observe that for all ${}_2F_3$-functions, the expansions of their parameters as well as their respective arguments are constant to leading order. Further, the ${}_2F_3$-functions constituted by $\boldsymbol{a_4}$ and $\boldsymbol{b_4}$ will be reduced to ${}_1F_2$-functions as the leading orders of a_{41} and b_{42} are equal, due to which they cancel each other out. Lastly, as $a_{22} = -1 + \alpha$, the Pochhammer term $(a_{22})_n = (-1+\alpha)\,(\alpha)\,(1+\alpha)...$, i.e. the second factor is of order $O(\alpha)$. Hence, for $n \geq 2$ all series terms of ${}_2F_3(\boldsymbol{a_2}, \boldsymbol{b_2}, z(y=0))$ are of order (α). The same applies for ${}_2F_3(\boldsymbol{a_2}{+}\boldsymbol{1}, \boldsymbol{b_2}{+}\boldsymbol{1}, z(y=0))$, where for $n \geq 1$ the series terms are of order $O(\alpha)$. With this, we can now formally expand the ${}_2F_3$-function whereupon we obtain

$$\begin{aligned} {}_2F_3\left(\begin{matrix}\boldsymbol{a_2}\\ \boldsymbol{b_2}\end{matrix}; -iRe\,\alpha\right) &= \sum_{n=0}^{\infty} \frac{(1)_n\,(-1+\alpha)_n}{(1)_n\,\left(\frac{1}{2}(1-\sigma_0)\right)_n\,\left(\frac{1}{2}(1+\sigma_0)\right)_n} \frac{(-iRe_\alpha)^n}{n!} + O(\alpha) \\ &= \frac{\omega_1}{\omega_1 - 1} + O(\alpha), \end{aligned} \tag{A.11}$$

where the series terms for $n \geq 2$ are of order $O(\alpha)$. The same applies for the generalized hypergeometric function ${}_2F_3\,(\boldsymbol{a_2}{+}\boldsymbol{1}, \boldsymbol{b_2}{+}\boldsymbol{1}; -iRe\,\alpha)$, with the only difference being that due to the increment of 1 on all parameters, all series terms for $n \geq 1$ are of order $O(\alpha)$, which gives

$$\begin{aligned} {}_2F_3\left(\begin{matrix}\boldsymbol{a_2}+\boldsymbol{1}\\ \boldsymbol{b_2}+\boldsymbol{1}\end{matrix}; -iRe\,\alpha\right) &= \sum_{n=0}^{\infty} \frac{(2)_n\,(\alpha)_n}{(2)_n\,\left(\frac{1}{2}(3-\sigma_0)\right)_n\,\left(\frac{1}{2}(3+\sigma_0)\right)_n} \frac{(-iRe_\alpha)^n}{n!} + O(\alpha) \\ &= 1 + O(\alpha). \end{aligned} \tag{A.12}$$

$$\begin{aligned} {}_2F_3\left(\begin{matrix}\boldsymbol{a_4}\\ \boldsymbol{b_4}\end{matrix}; -iRe\,\alpha\right) &= \sum_{n=0}^{\infty} \frac{\left(\frac{1}{2}(-1+\sigma_0)\right)_n\,\left(\frac{1}{2}(3+\sigma_0)\right)_n}{(1+\sigma_0)_n\,\left(\frac{1}{2}(3+\sigma_0)\right)_n\,\left(\frac{1}{2}(3+\sigma_0)\right)_n} \frac{(-iRe_\alpha)^n}{n!} + O(\alpha) \\ &= \sum_{n=0}^{\infty} \frac{\left(\frac{1}{2}(-1+\sigma_0)\right)_n}{(1+\sigma_0)_n\,\left(\frac{1}{2}(3+\sigma_0)\right)_n} \frac{(-iRe_\alpha)^n}{n!} + O(\alpha) \\ &= {}_1F_2\left(\begin{matrix}a_{41,0}\\ b_{41,0}, b_{42,0}\end{matrix}; -iRe_\alpha\right) + O(\alpha), \end{aligned} \tag{A.13}$$

where $a_{42,0}$, $b_{41,0}$ and $b_{43,0}$ denote the leading orders of the corresponding parameters expanded in (A.9). As is displayed in (A.13) the leading orders of a_{41} and b_{42} cancel each other out, yielding a ${}_1F_2$ generalized hypergeometric function to leading order. An analogous expansion is conducted for the last generalized hypergeometric function ${}_2F_3\,(\boldsymbol{a_4}{+}\boldsymbol{1}, \boldsymbol{b_4}{+}\boldsymbol{1}; -iRe\,\alpha)$ resulting in

$$\begin{aligned} {}_2F_3\left(\begin{matrix}\boldsymbol{a_4}+\boldsymbol{1}\\ \boldsymbol{b_4}+\boldsymbol{1}\end{matrix}; -iRe\,\alpha\right) &= \sum_{n=0}^{\infty} \frac{\left(\frac{1}{2}(5+\sigma_0)\right)_n\,\left(\frac{1}{2}(1+\sigma_0)\right)_n}{(2+\sigma_0)_n\,\left(\frac{1}{2}(5+\sigma_0)\right)_n\,\left(\frac{1}{2}(5+\sigma_0)\right)_n} \frac{(-iRe_\alpha)^n}{n!} + O(\alpha) \\ &= \sum_{n=0}^{\infty} \frac{\left(\frac{1}{2}(1+\sigma_0)\right)_n}{(2+\sigma_0)_n\,\left(\frac{1}{2}(5+\sigma_0)\right)_n} \frac{(-iRe_\alpha)^n}{n!} + O(\alpha) \\ &= {}_1F_2\left(\begin{matrix}a_{41,0}+1\\ b_{41,0}+1, b_{42,0}+1\end{matrix}; -iRe_\alpha\right) + O(\alpha). \end{aligned} \tag{A.14}$$

Employing all expansions derived above into the EVP (3.54) gives the degenerated EVP (3.61), for which results are computed and discussed in section 3.2.2. It is noteworthy that the results of (3.61) agree perfectly with numerical computations of (3.54) conducted in the distinguished limit.

A.3 Asymptotic expansion for large streamwise wave numbers ($\alpha \to \infty$)

The asymptotic analysis for the case $\alpha \to \infty$ is rather straightforward. The EVP (3.54) is transformed by redefining

$$\alpha_T := \frac{1}{\alpha}, \tag{A.15}$$

which now for the examined limit yields $\alpha_T \to 0$, allowing us to employ classical tools of asymptotic theory. The EVP then is written as

$$\begin{aligned}
&\mathcal{D}(\alpha, \beta, Re, \omega) \\
&= {}_2F_3\left(\begin{matrix}\boldsymbol{a_2}\\ \boldsymbol{b_2}\end{matrix}; -iRe\,\frac{1}{\alpha_T}\right)\left[\frac{\overline{a}_4}{\overline{b}_4}\, i\frac{1}{\alpha_T} Re\, {}_2F_3\left(\begin{matrix}\boldsymbol{a_4{+}1}\\ \boldsymbol{b_4{+}1}\end{matrix}; -iRe\,\frac{1}{\alpha_T}\right) - \left(\frac{\sigma+1}{2}\right) {}_2F_3\left(\begin{matrix}\boldsymbol{a_4}\\ \boldsymbol{b_4}\end{matrix}; -iRe\,\frac{1}{\alpha_T}\right)\right] \\
&- {}_2F_3\left(\begin{matrix}\boldsymbol{a_4}\\ \boldsymbol{b_4}\end{matrix}; -iRe\,\frac{1}{\alpha_T}\right)\left[\frac{\overline{a}_2}{\overline{b}_2}\, i\frac{1}{\alpha_T} Re\, {}_2F_3\left(\begin{matrix}\boldsymbol{a_2{+}1}\\ \boldsymbol{b_2{+}1}\end{matrix}; -iRe\,\frac{1}{\alpha_T}\right) - \frac{1}{\alpha_T} {}_2F_3\left(\begin{matrix}\boldsymbol{a_2}\\ \boldsymbol{b_2}\end{matrix}; -iRe\,\frac{1}{\alpha_T}\right)\right] = 0,
\end{aligned} \tag{A.16}$$

with the parameters

$$\boldsymbol{a_2} = \begin{pmatrix} \tilde{\alpha}_T + \frac{1}{\alpha_T} \\ -\tilde{\alpha}_T + \frac{1}{\alpha_T} \end{pmatrix}, \qquad \boldsymbol{a_4} = \begin{pmatrix} \frac{1}{2} + \frac{\sigma}{2} + \tilde{\alpha}_T \\ \frac{1}{2} + \frac{\sigma}{2} - \tilde{\alpha}_T \end{pmatrix}, \tag{A.17}$$

$$\boldsymbol{b_2} = \begin{pmatrix} 1 + 2\frac{1}{\alpha_T} \\ \frac{1}{2} - \frac{\sigma}{2} + \frac{1}{\alpha_T} \\ \frac{1}{2} + \frac{\sigma}{2} + \frac{1}{\alpha_T} \end{pmatrix}, \qquad \boldsymbol{b_4} = \begin{pmatrix} 1 + \sigma \\ \frac{3}{2} + \frac{\sigma}{2} + \frac{1}{\alpha_T} \\ \frac{3}{2} + \frac{\sigma}{2} - \frac{1}{\alpha_T} \end{pmatrix}, \tag{A.18}$$

with $\tilde{\alpha}_T = \sqrt{(1/\alpha_T)^2 + 1}$ and $\sigma = \sqrt{4/\alpha_T + 1 + 4iRe\,(1/\alpha_T - \omega)}$. Asymptotic theories are now used to derive a leading order solution for $\omega(\alpha_T)$. For this, we assume a Laurent-series of the form

$$\omega(\alpha_T) = \sum_{n=-\infty}^{\infty} \omega_n \alpha_T^n. \tag{A.19}$$

Without going into detail, the following can be observed:
(i) In the above series, for $n \geq -1$ the parameter quotients $\boldsymbol{a_i}/\boldsymbol{b_i}$ are of order $O(\alpha_T)$ regardless of the series count of the corresponding hypergeometric series. Together with the argument of the series, each term of these series is of $O(1)$. For $n < 1$, however, these series diverge heavily as then each term of the series is at least of order $O(\alpha_T^{-1})$. Hence the leading order of (A.19) must be

$$\omega(\alpha_T) = \omega_{(-1)} \frac{1}{\alpha_T} + O(1), \tag{A.20}$$

which yields

$$\sigma(\alpha_T) = \frac{2}{\alpha_T} + iRe\,\left(1 - \omega_{(-1)}\right) + O(\alpha_T) \tag{A.21}$$

(ii) The order of the dispersion relation (A.16) with (A.20) purely depends on the factors of each series product. Concretely, we need to compare the leading orders of:

$$T_1 = \frac{\overline{a_4}}{\overline{b_4}}\, iRe\, \frac{1}{\alpha_T} \tag{A.22}$$

$$T_2 = \frac{1}{\alpha_T} - \left(\frac{\sigma+1}{2}\right) = \frac{1}{2}\left(iRe\,\left(1 - \omega_{(-1)}\right) - 1\right) + O(\alpha_T) \tag{A.23}$$

$$T_3 = \frac{\overline{a_2}}{\overline{b_2}}\, iRe\, \frac{1}{\alpha_T}. \tag{A.24}$$

As already pointed out, the leading orders of the parameter quotients respectively is $O(\alpha_T)$. Hence, T_2 embodies the leading order term and has to disappear in order to yield (A.16) zero in the leading order. This results in

$$\omega_{(-1)} = 1 - \frac{i}{Re}, \tag{A.25}$$

which substituted into (A.19) gives

$$\omega(\alpha) = \left(1 - \frac{i}{Re}\right)\,\alpha + O(1). \tag{A.26}$$

The real part of the eigenvalue thus is equal to the wave number, while the imaginary part is always negative, regardless of the Reynolds number. The flow therefore is stable at the infinity limit $\alpha \to \infty$ for arbitrary Reynolds numbers.

A.4 Asymptotic expansion for the Stokes-limit ($Re \to 0$)

The Stokes-limit can be treated qualitatively, claiming that flows at very small Reynolds numbers are naturally globally stable. For the ASBL, it is still possible to demonstrate this with the already employed asymptotic methods rather rigorously. First, we assume a Laurent-series of the form

$$\omega(Re) = \sum_{n=-\infty}^{\infty} \omega_n\, Re^n, \tag{A.27}$$

In analogy to the large α case, we examine the hypergeometric series with regard to their asymptotic behavior. To be specific, it is generally necessary for the series terms to not diverge, as then the series surely diverges. Since all four series in (3.54) should not be equivalent in the Stokes-limit, it is obligatory to prevent any of these series from diverging. The parameter quotients $\frac{\overline{a_i}}{\overline{b_i}}$ must therefore at least be of order $O(Re^{-1})$ in order to cancel out with the argument of each respective series. With this, the Laurent-series (A.27) reduces to

$$\omega(Re) = \sum_{n=-2}^{\infty} \omega_n\, Re^n. \tag{A.28}$$

In fact, with this reduction every term in (3.54) is of order $O(1)$, except

$$\sigma(Re) = 2\,\omega_{(-2)}\,\frac{1}{\sqrt{Re}} + O(1), \tag{A.29}$$

which in conclusion constitutes the leading order of the EVP (3.54), which must be zero. This demands

$$\omega_{(-2)} = 0, \tag{A.30}$$

which further reduces the Laurent-series to

$$\omega(Re) = \omega_{(-1)}\frac{1}{Re} + O(1). \tag{A.31}$$

So far the considerations helped to determine the leading order of the ansatz (A.27). It is still necessary, however, to determine the coefficient of the leading order $\omega_{(-1)}$. This is also achieved by doing a leading order consideration. All series are now of order $O(1)$. It can even be shown that all hypergeometric series ${}_2F_3(\cdot) = 1 + O(\sqrt{Re})$. Again, the leading order of the EVP comes down to evaluating the three pre-factor terms T_1, T_2 and T_3 given in (A.24). With (A.29), the terms T_1 and T_3 are of order $O(\sqrt{Re})$. Consequently, the leading order of (3.54) is given by

$$\mathcal{D}(Re)^{O(1)} = \alpha - \left(\frac{\sigma+1}{2}\right) = \alpha - \frac{1}{2}\left(1 + \sqrt{4\,\alpha^2 + 1 - 4i\omega_{(-1)}}\right) = 0, \tag{A.32}$$

which gives

$$\omega_{(-1)} = -i\alpha. \tag{A.33}$$

Substituted into (A.31) we obtain

$$\omega(Re) = -i\alpha\,\frac{1}{Re} + O(1). \tag{A.34}$$

As was claimed at the beginning of this analysis, the flow is globally stable in the Stokes-limit for any $\alpha \geq 0$.

B Solution to Orr-Sommerfeld equation for plane Couette flow

The solution of (2.43) for plane Couette flow, i.e. $U(y) = y$, is given by

$$\begin{aligned}\tilde{v}(y) \; &= C_1 e^{ky} + C_2 e^{ky} \int_0^y e^{-2ky} \mathrm{d}y \\ &+ \frac{C_3}{2k}\left(e^{ky}\int_0^y e^{-ky} Ai\left(\frac{(-i\alpha Re)^{\frac{1}{3}}(ik^2 - \alpha Rey + \omega Re)}{\alpha Re}\right)\mathrm{d}y\right. \\ &\left. - e^{-ky}\int_0^y e^{ky} Ai\left(\frac{(-i\alpha Re)^{\frac{1}{3}}(ik^2 - \alpha Rey + \omega Re)}{\alpha Re}\right)\mathrm{d}y\right) \\ &+ \frac{C_4}{2k}\left(e^{ky}\int_0^y e^{-ky} Bi\left(\frac{(-i\alpha Re)^{\frac{1}{3}}(ik^2 - \alpha Rey + \omega Re)}{\alpha Re}\right)\mathrm{d}y\right. \\ &\left. - e^{-ky}\int_0^y e^{ky} Bi\left(\frac{(-i\alpha Re)^{\frac{1}{3}}(ik^2 - \alpha Rey + \omega Re)}{\alpha Re}\right)\mathrm{d}y\right).\end{aligned} \tag{B.1}$$

Due to the fluid domain being bounded by two parallel plates, the BC (4.5) lead to

$$\underbrace{\begin{pmatrix} 1 & -\frac{1}{2k} & 0 & 0 \\ e^k & -\frac{e^{-k}}{2k} & \frac{-e^{-k}I_1(1)+e^k I_2(1)}{2k} & \frac{-e^{-k}I_3(1)+e^k I_4(1)}{2k} \\ k & \frac{1}{2} & 0 & 0 \\ ke^k & \frac{e^{-k}}{2} & \frac{e^{-k}I_1(1)+e^k I_2(1)}{2} & \frac{e^{-k}I_3(1)+e^k I_4(1)}{2} \end{pmatrix}}_{\boldsymbol{A}} \begin{pmatrix} C_1 \\ C_2 \\ C_3 \\ C_4 \end{pmatrix} = \begin{pmatrix} 0 \\ 0 \\ 0 \\ 0 \end{pmatrix}, \tag{B.2}$$

with

$$\begin{aligned} I_1(y) &= \int_0^y e^{ky} Ai\left(\frac{(-i\alpha Re)^{\frac{1}{3}}(ik^2 - \alpha Rey + \omega Re)}{\alpha Re}\right)\mathrm{d}y, \\ I_2(y) &= \int_0^y e^{-ky} Ai\left(\frac{(-i\alpha Re)^{\frac{1}{3}}(ik^2 - \alpha Rey + \omega Re)}{\alpha Re}\right)\mathrm{d}y, \\ I_3(y) &= \int_0^y e^{ky} Bi\left(\frac{(-i\alpha Re)^{\frac{1}{3}}(ik^2 - \alpha Rey + \omega Re)}{\alpha Re}\right)\mathrm{d}y, \\ I_4(y) &= \int_0^y e^{-ky} Bi\left(\frac{(-i\alpha Re)^{\frac{1}{3}}(ik^2 - \alpha Rey + \omega Re)}{\alpha Re}\right)\mathrm{d}y. \end{aligned} \tag{B.3}$$